High Resolution Wind and Bathymetry Maps from Synthetic Aperture Radar to increase Ship Safety and Ship Traffic Monitoring from Space

Dissertation
zur Erlangung des Doktorgrades
der Naturwissenschaften im Fachbereich
Geowissenschaften
der Universität Hamburg

vorgelegt von:

Stephan Brusch
aus
Schwerin

Hamburg
2011

Als Dissertation angenommen
vom Fachbereich Geowissenschaften der Universität Hamburg

Auf Grund der Gutachten
von
Prof. Dr. Hartmut Graßl
und
Dr. Susanne Lehner

Hamburg, den 02.02.2011
Prof. Dr. Jürgen Oßenbrügge
(Leiter des Departments für Geowissenschaften)

This document gives a summary of 3 publications written by Stephan Brusch as lead author. All publications are accepted or already printed in peer reviewed international journals (IEEE, IJRS)

List of Publications:

[1] S. Brusch, S. Lehner, and J. S.-Stellenfleth (2008) "*Synergetic Use of Radar and Optical Satellite Images to Support Severe Storm Prediction for Offshore Wind Farming*" in IEEE Journal of Selected Topics in Applied Earth Observations and Remote Sensing, 1 (1), pages 57-66. DOI: 10.1109/JSTARS.2008.2001838. ISSN 1939-1404

[2] S. Brusch, P. Held, S. Lehner, W. Rosenthal, A. Pleskachevsky (2010) "*Underwater Bottom-Topography in coastal areas from TerraSAR-X data*" in IJRS International Journal of Remote Sensing, accepted for publication

[3] S. Brusch, S. Lehner, T. Fritz, M. Soccorsi, A. Soloviev, B. van Schie (2010) "*Ship surveillance with TerraSAR-X*" in IEEE-Transactions on Geoscience and Remote Sensing (TGRS), 10.1109/TGRS.2010.2071879, ISSN: 0196-2892

Summary:

In this work satellite images taken by space borne sensors are used to explain atmospheric as well as oceanographic features, e.g. wind fields or ocean wave heights, all are compared to operational numerical model output. One focus in the *first paper* was to understand the synergy of high resolution passive microwave satellite sensors and optical sensors on different space scales. The jointly retrieved meteorological and oceanographical parameters, e.g. wind speed and significant wave height, show the high quality of space based data in understanding of complex systems, e. g. wave fields. A space based Radar and imaging spectrometers are used to analyse wind and waves during extreme weather conditions, in particular, to describe the spatial evolution of the atmospheric boundary layer processes involved in cold air outbreaks. The behaviour of wind fields in coastal and offshore regions is investigated and compared to numerical model results. For wind field retrieval a geophysical model function is used. High resolution radar satellites provide a fine scale structure of wind fields and information on small-scale atmospheric features as well as more extreme values of environmental parameters during high impact

weather, which are not captured well by the numerical models. One case study showed that cloud patterns seen in the optical data and radar cross-section modulation give a consistent dynamical picture of the atmospheric processes. The relevance of space based data for assimilation into numerical models and for offshore wind farming is discussed.

Waves are the most obvious feature in Synthetic Aperture Radar (SAR) images over the ocean. The modulation of sea surface roughness by wind makes them visible in radar images and thus variations of wave fields can be detected. Due to the high horizontal resolution of SAR data (down to 1m) wave refraction and shoaling of swell can be monitored. Radar sensors are able to monitor waves with a wavelength longer then the cut-off wavelength. The cut-off wavelength depends on the SAR sensor (resolution) and is a function of wind speed and significant wave height. In this work algorithm to retrieve sea state parameters measured by high resolution SAR data have been adapted from known C-Band SAR systems (ERS-2/ENVISAT) to the new X-Band satellite TS-X (TerraSAR-X).

TS-X gives access to spatial resolution as fine as 1 m in Spotlight mode and high resolution variability of coastal wave fields. Images from the TS-X satellite are particularly suitable for the observation of wave behaviour in transient and shallow water (<100m water depth). By computing the 2 dimensional spectra waves can be tracked. In the *second paper* it is shown, how wave Refraction and shoaling can be monitored and the calculation of bottom topography can be provided. The retrieved bathymetry is compared to ETOPO1 (a 1 arc-minute global relief model of Earth's surface that integrates land topography and ocean bathymetry, source: NOAA), US Coastal Relief Model (a 3 arc-second US model integrating offshore bathymetry with land topography, source: NOAA) and sea charts from the British Admiralty.

Knowledge of the water depth is one important parameter for monitoring of ship traffic and secure navigation. Planning of ship routes is an important economic factor. The knowledge about bathymetry in coastal regions or river estuaries is of high interest. Therefore, ship detection and maritime surveillance with high resolution sensors has increased, in particular in the field of maritime security and maritime safety in the last years.

In the *third paper* first results on the combined use of TS-X ship detection, AIS (Automatic Identification System), and Satellite AIS is presented. The AIS system is an effective terrestrial method for tracking vessels in real time typically up to 40 km off the coast. The quality of TS-X images with respect to ship detection is evaluated and a first assessment of its performance for ship detection is given. Velocity of a moving ship is estimated using complex TS-X data. First results on simultaneous superposition of satellite AIS and high resolution radar images are presented.

Summary Report of my Publications:

1. Discussion of each publication:

Paper 1: Synergetic Use of Radar and Optical Satellite Images to Support Severe Storm Prediction for Offshore Wind Farming (see Appendix)

Abstract

Satellite images taken by space-borne radar sensors and cloud parameters from optical data are combined to help maintain and plan offshore wind farms. With both the synthetic aperture radar (SAR) and the medium resolution imaging spectrometer (MERIS) onboard the environmental satellite (ENVISAT) of ESA a severe cold air outbreak is analyzed on 1 November 2006 over the North Sea. The satellite data are compared with numerical model results of the German Weather Service "Lokal Modell" (LM) and the high-resolution limited area model (HIRLAM). LM and HIRLAM show differences in mesoscale turbulent behaviour and coastal shadowing. Maximum wind speeds of up to 25 m/s are measured by SAR and are confirmed by the models. However, significant differences are observed in the models concerning location of the maxima. High-resolution ENVISAT ASAR measurements provide very detailed information on small-scale atmospheric features, which seem not to be captured well by the numerical models in coastal areas. Meteosat Second Generation (MSG) data are used to determine the movement of cloud patterns. Cloud patterns seen in the optical data and radar cross-section modulation at the ocean surface give a consistent dynamical picture of the atmospheric boundary layer processes. The relevance for offshore wind farming is discussed.

Discussion of the Paper

An explanation for particulary high individual ocean waves causing an accident at the offshore platform FiNO 1 in the North Sea is given by investigating the fine scale structure of the low pressure system ("Britta") on 1 November 2006 using satellite and numerical model data (HIRLAM, LM - DWD). "Britta" developed initially as a frontal wave in the central North Atlantic early on 28 October 2006 and, after moving firstly northeast, turned further east and developed hurricane-force northwesterly winds on its western side as it passed through the North Sea. Britta was captured partly by an ENVISAT ASAR with a resolution approximately of 150m x 150m in Wide Swath Mode (WSM) on 1 November 2006 at 10:42 UTC. The wind field was derived by using the CMOD algorithm and then compared to model results (see Figure 1).

The calculated wind fields of Storm Britta from the HIRLAM or the German Weather Service LM are validated using the ENVISAT ASAR and QuikSCAT wind field. In Figure 2 the comparison of the German Weather Service LM and ENVISAT ASAR is shown. LM shows differences in mesoscale turbulent behaviour and coastal shadowing. Maximum wind speed of up to 25 m/s is measured by SAR and cannot be observed in the model output. Significant differences are observed in the location of the wind maxima. Due to the high horizontal resolution ENVISAT ASAR data allow very detailed information on small scale atmospheric and oceanographic features, which are not captured by the numerical model in particular for coastal areas.

Mesoscale features, e.g., downburst due to cloud streets with a diameter of up 15 km are not detected by LM. The Marine Atmospheric Boundary Layer (MABL) and the ocean often exchange large amounts of heat, moisture, and momentum. Updrafts and downdrafts in cells and roll-like updrafts and downdrafts in cloud streets in the MABL cause strong flux differences. Cells and rolls each cause distinctive signatures in the wave fields. The signatures result from changes in ocean surface roughness caused by wind gusts. For the explanation of gusts high backscatter in front of cloud bands can be explained by optical cloud products, e.g., cloud optical thickness and total water path that are products of combined visible and infrared channels from MERIS and the Moderate Resolution Imaging Spectroradiometer (MODIS). Ahead of clouds the surface wind speed is observed to increase by 15 m/s. A sub-image in Figure 3 (left part) shows a cut through a cloud pattern perpendicular to the wind direction with embedded convective cloud streets separated by up to 13 km. The main wind direction is from north to south. These clouds are precipitating. From north to south an increase in wind speed of 5 m/s is observed. Footprints of these cloud streets with outflows (downward winds) ahead of convective lines are detectable in the radar images of the sea surface (see Fig. 3 left) by the roughening of the sea surface. Thus strong convective outflow ahead of convective cloud patterns is not present in the numerical atmospheric models and can be used to improve or validate them. ENVISAT ASAR wind vector fields show more structure caused by coasts, topography, and cloud pattern. Results open new opportunities to compare offshore wind farm sites and validate the results with in situ measurements and models of nearly the whole North Sea.

The joint use of high-resolution SAR, Scatterometer and optical data allows observation of high-resolution wind fields also between offshore wind farms, because small scale wind patterns can be detected and can help to understand the behaviour of an offshore wind farm. While large-scale wind patterns are mainly responsible for wave height, which is an important factor for

the construction of offshore wind turbines and, therefore, for their life time, short-term wind power forecast is one of the most important points in managing wind parks. Satellite retrieved high-resolution wind vector fields can help to increase the confidence level of weather forecast models.

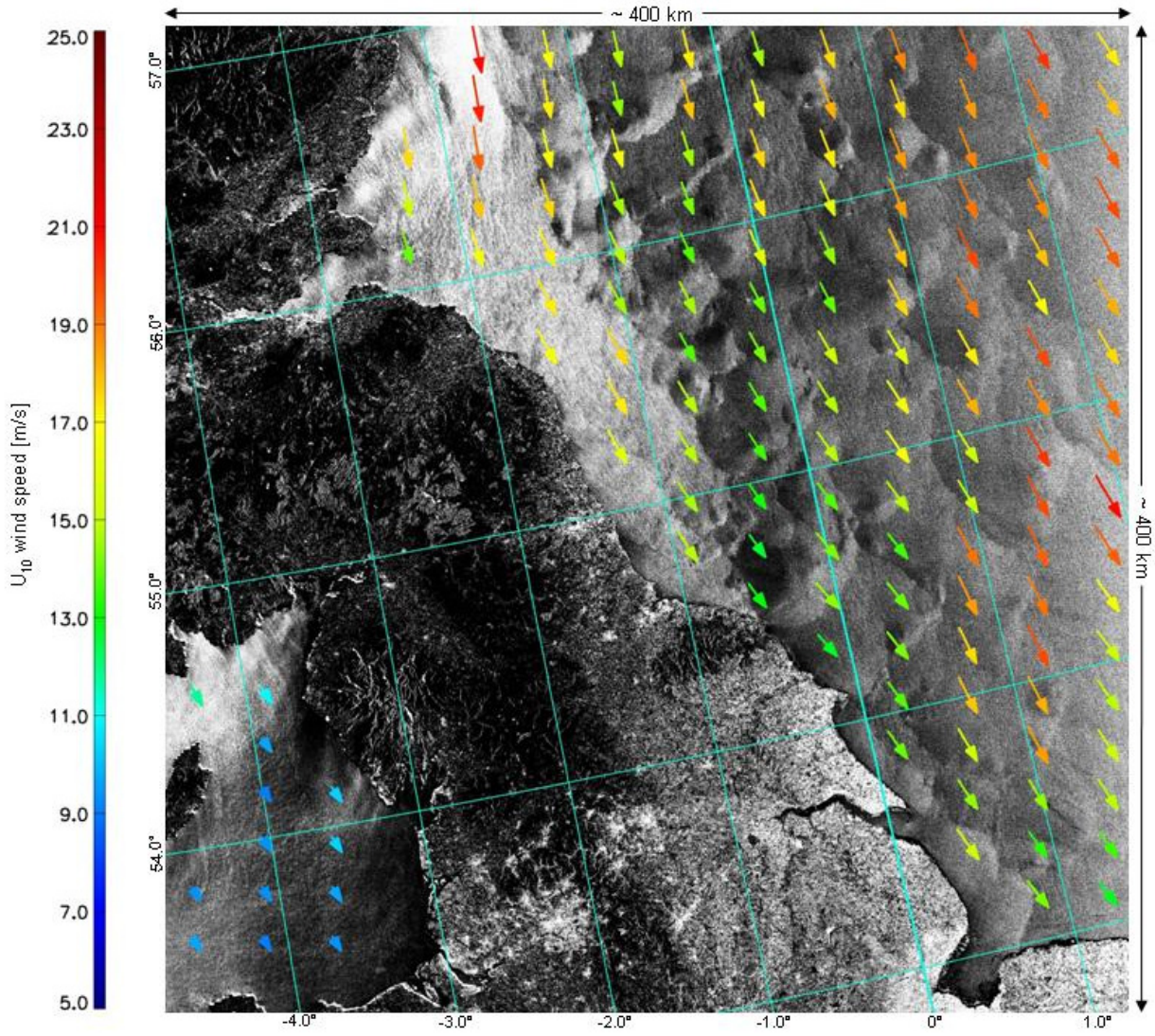

Fig. 1: ENVISAT ASAR Wide Swath Mode-WSM (400km x 400km coverage, 150m x 150m resolution) with superimposed wind vector field at 10m height on 1 November 2006 at 10:42 UTC.

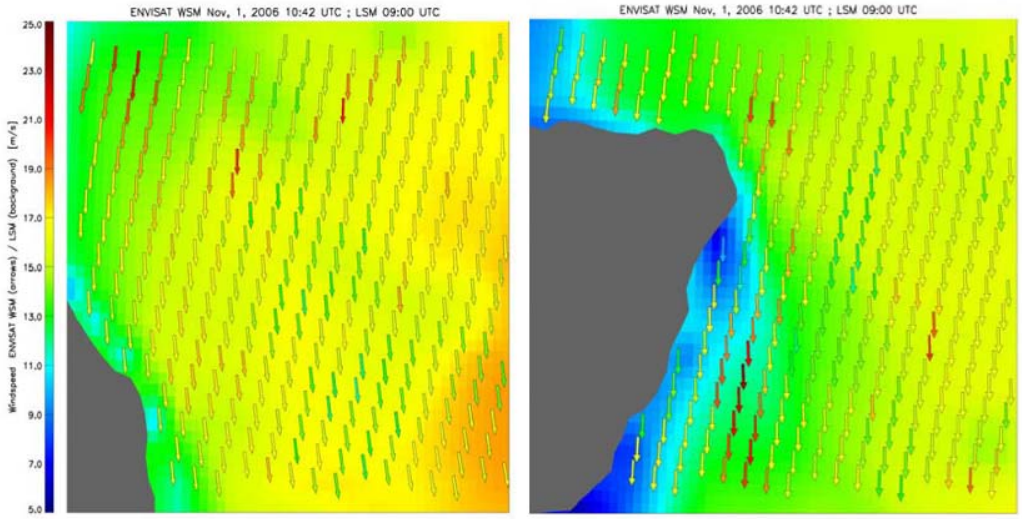

Fig. 2: ***Left****: Wind field of the LM model at 09:00 UTC (background) and ENVISAT ASAR wind vectors superimposed as arrows at 10:42 UTC (coordinates: bottom left corner: 54° 6'10.26"N, 1° 5'21.24"W, upper right corner: 55° 2'46.33"N, 0°34'5.16"E)* ***Right****: Wind field of the LM model input at 09:00 UTC (background) and the ENVISAT ASAR wind vectors at 10:42 UTC superimposed by arrows (coordinates: bottom left corner: 56°29'23.23"N, 3° 1'41.98"W; upper right corner: 58°10'49.45"N, 0°10'23.16"W); wind vectors are coloured as the model wind speed*

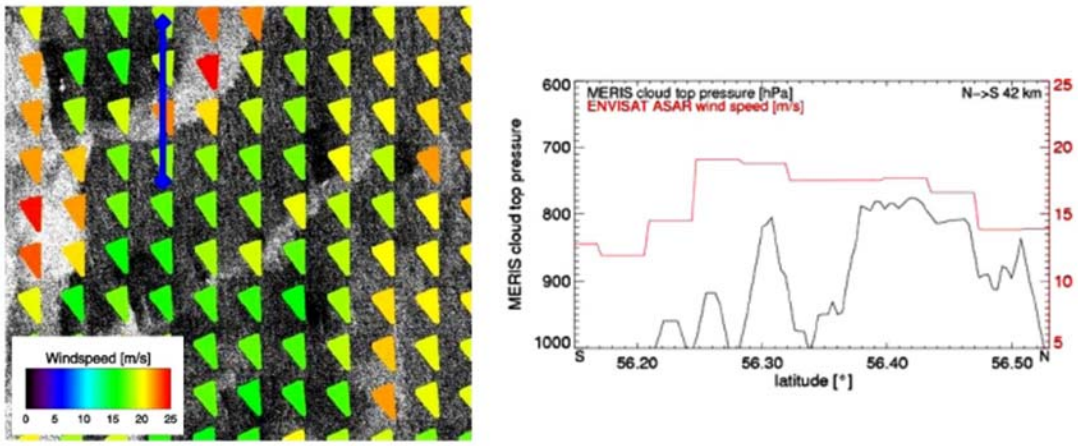

Fig. 3: ***Left****: Sub-scene ENVISAT ASAR WSM (120 km x120 km, coordinates: bottom left corner: 56°15'47.62"N, 1° 9'51.35"W, upper right corner: 57°14'19.46"N, 1° 1'50.94"E) derived wind field on 1 November 2006 at 10:42 UTC.* ***Right****: South-North cut along the blue line (42km) showing MERIS cloud top pressure and ENVISAT ASAR wind speed.*

Paper 2: Underwater Bottom-topography in coastal areas from TerraSAR-X data (see Appendix)

Abstract

In this paper, wave refraction and shoaling in coastal areas are investigated and used to derive the bathymetry. Due to its high spatial resolution, which can achieve up to 1m in Spotlight mode, and its low cut-off wavelength, images from the TS-X satellite are particularly suitable for the observation of wave behaviour in shallow water. By computing the two dimensional spectra shoaling waves are tracked from the open sea up to the shoreline. The observed wave refraction and shoaling is compared with wave refraction laws and first order wave theory (Airy Theory). The retrieved bathymetry is compared against depth data from other sources like ETOPO1 (a 1 arc-minute global relief model of Earth's surface that integrates land topography and ocean bathymetry, source: NOAA), US Coastal Relief Model (a 3 arc-second US model integrating offshore bathymetry with land topography, source: NOAA) and sea charts from the British Admiralty. Another goal of this paper is the investigation of breaking waves showing up as near shore image patterns. A theory is presented how to derive the height of breaking waves by use of this pattern. SAR images with azimuth as well as range travelling waves are investigated. As test sites the entrance of Port Phillip near Melbourne (Australia) and the Duck Research Pier in North Carolina (USA) are chosen.

Discussion of the Paper

Calibrated SAR Spotlight images from the German TS-X Satellite are used to investigate the variability of the coastal wave field. TS-X is capable to detect wave refraction and wave shoaling due to its high spatial resolution. A method to track shoaling waves on their way from the open ocean to the beach is demonstrated. Figure 4 shows retrieved wave tracks based on 2-dim FFT analysis of a TS-X Spotlight Mode image obtained on 17 March 2008 over the entrance of Port Phillip in Australia. In this case, waves travelling in azimuth direction were investigated. It has been found, that azimuth travelling waves down to 70m wavelength and around 2m significant wave height can still be captured by the TS-X satellite. By tracking wave rays, the change of wavelength can be measured. The linear dispersion relation for ocean surface gravity waves is used to derive water depth from the wavelength measured. Figure 5 shows the retrieved bathymetry. The retrieved bottom topography fits well to depth information from an official nautical chart. The scatter plot is given on the sub-image of Figure 5. This comparison is presented to show the general agreement

of SAR obtained depths against the nautical map. The depth difference is smaller than 5m for 72,2% of entries, and <7m for 89,2%). A new approach is presented to derive the height of breaking waves from image patterns, produced by breaking waves. As a wave is shoaling, wave height increases, which leads to an increase of the orbital velocity of water particles within the wave. If the velocities of water particles become too high, they cannot be tracked by SAR any longer and smearing in the SAR images occurs. The smearing is caused by scatterers with different velocities.

In Figure 6 detected breaking patterns in TS-X Spotlight image acquired on 17 March 2008 over the entrance of Port Phillip are shown. In sub-image A an area westwards and in sub-image B, an area eastwards of the Port-Phillip entrance are shown. The mean length of smearing is 60m in A and 180m in B. From the measured length of breaking patterns in sub-image A and B of figure 6 the height of breaking waves is calculated to be 4.50m and 3.95m, respectively. The retrieved wave height is compared to wave height calculated with wave shoaling theories and shows a good agreement. The measured maximum wave height from a buoy is about 2.6m at the time of SAR image acquisition. The comparison of wave height derived from SAR with 3,95m against the buoy measurement shows a difference of about 1m which can be explained by the shoaling effect near the coast.

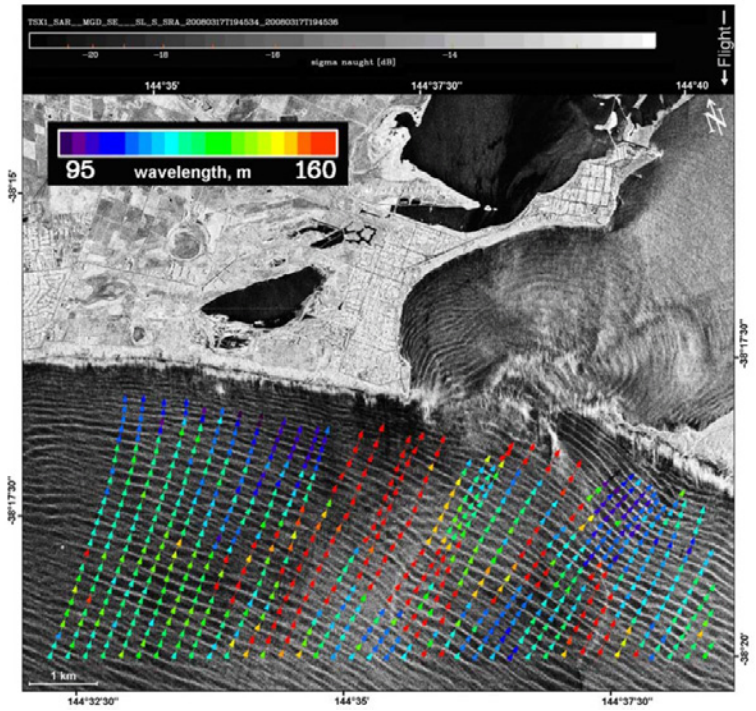

Fig. 4: TS-X Spotlight image acquired over entrance of Port Phillip in Melbourne, on 17 March 2008 at 19:45 UTC. Tracked wave rays indicating wave length are represented by colour coded arrows

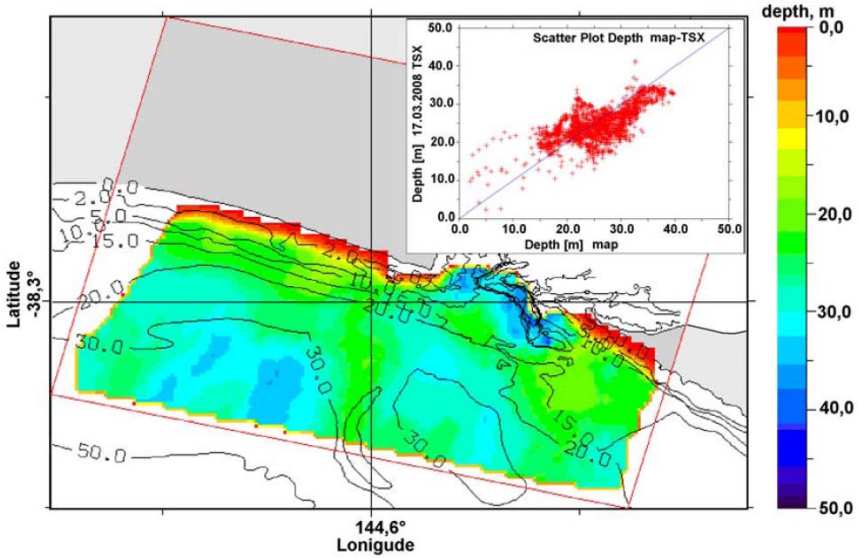

Fig. 5: SAR retrieved underwater bottom topography compared against depth isolines from nautical chart of the Port Phillip area, Melbourne-Australia.

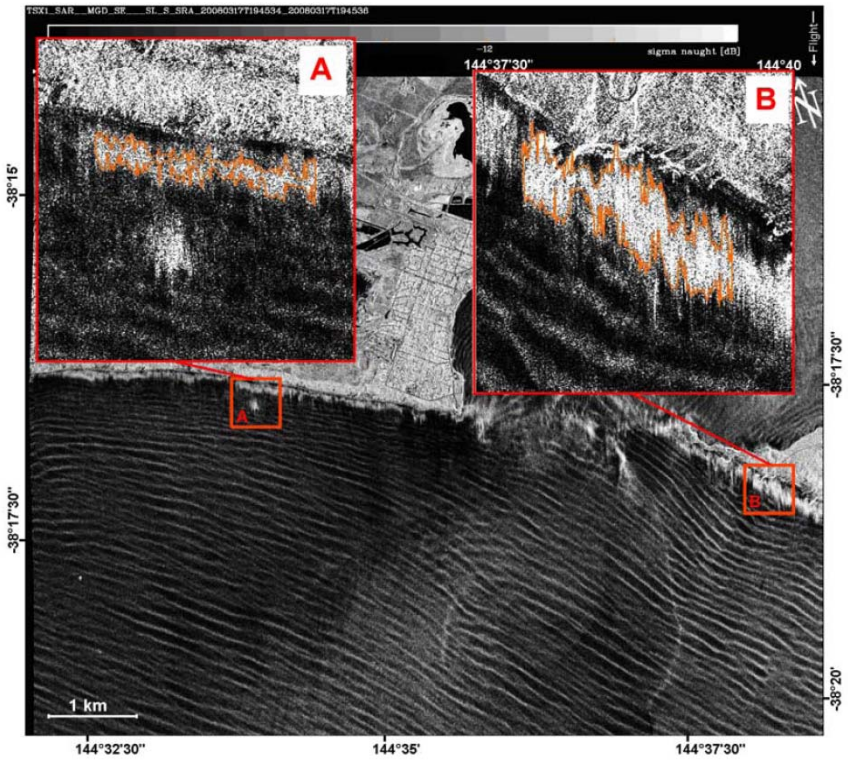

Fig. 6: Output of breaking wave streaks detection algorithm for TS-X Spotlight image acquired on 17 March 2008 over the entrance of Port Phillip, Melbourne. Orange contour line: SAR imaged breaking waves (smeared in flight direction of the satellite)

Paper 3: Ship surveillance with TerraSAR-X (see Appendix)

Abstract

Ship detection is an important application of global monitoring of environment and security. In order to overcome the limitations by other systems, surveillance with satellite SAR (Synthetic Aperture Radar) is used because of its possibility to provide ship detection at high resolution over wide swaths and during all weather conditions. The new X-band radar on board the TS-X satellite gives access to spatial resolution as fine as 1 m. In this paper first result on the combined use of TS-X ship detection, AIS (Automatic Identification System), and Satellite AIS is presented. The AIS system is an effective terrestrial method for tracking vessels in real time typically up to 40 km off the coast. Satellite AIS is a space based system that allows almost global coverage for monitoring of ships. However, not all ships do operate their AIS and smaller ships are not equipped with AIS.

In this paper the quality of TS-X images with respect to ship detection is evaluated and a first assessment of its performance for ship detection is given. Velocity of a moving ship is estimated using complex TS-X data. As test cases, images were acquired over the North Sea, Baltic Sea, Atlantic Ocean, and Pacific Ocean in Stripmap mode with a resolution of 3m at coverage of 30kmx100 km. Simultaneous information on ship positions was available from TS-X and terrestrial as well as satellite AIS. First results on simultaneous superposition of Satellite AIS and high resolution radar images are presented.

Discussion of the Paper

The ship detection problem can be considered as a simple detection of bright point targets against a noisy background. However, the reality is more complicated due to possible confusions associated with different environmental parameters, e.g. wind induced wave crests that could be falsely detected as ships. An optimum detector for this situation should maximize the probability of detection while minimizing the probability of false alarm. We therefore adopted a method that aims at maximizing the detection of ship targets. Validation of the method is performed by in-situ measurements (Automatic Identification System – AIS). But this coastal-based surveillance system are limited in their coverage, e.g., coastal AIS only covers up to 40 km off the coast and requires ships that have AIS onboard and operate it correctly. Satellite imagery gives the possibility to overcome the near to shore limits.

In the study TS-X acquisitions are analyzed in order to assess the potential of this new sensor for ship monitoring. An adapted ship detection algorithm for

TS-X images based on the classical CFAR method is used for the detection of ships. Ship detection systems generally consist of five steps:

-Preprocessing (Calibration, Geolocation)
-Land Masking
-Prescreening (CFAR)
-Discrimination (meteorological phenomena, SAR image artefacts)
-Feature Extraction (ship length, width, heading, and speed)

The developed algorithm was implemented for Near Real Time (NRT) use in the DLR Ground Station Neustrelitz. TS-X is the only radar sensor with a resolution of 1m, hence suited well for monitoring ship traffic both in coastal areas and also over the open ocean. Ship detection shows still limitations in coastal areas due to insufficient land masking or geophysical phenomena such as tidal change or severe weather. The algorithm has been integrated in to the DLR Toolbox (SAR AIS INtegrated Toolbox, SAINT) for automatic detection of both large and small vessels. Results show in case of the AIS-carrying larger vessels (length above 35m) that they were detected in more than 90 % of all cases. For smaller vessels (length < 30m) the assessment of quality is more difficult due to increasing false alarms in high sea state situations with breaking waves.

The limited coverage of terrestrial AIS coast makes Satellite AIS and SAR perfect candidates to fill this gap of ship traffic information over open oceans. In the next example, the synergetic use of high resolution earth observation data and satellite based AIS data is demonstrated. Figure 7 shows a TS-X Stripmap mode image in the southern Atlantic Ocean near Cape Town. Vessels detected by SAR are superimposed and marked with red rectangles. Collocated ships with terrestrial AIS messages are marked by green rectangles. Satellite AIS is superimposed with yellow rectangles. SAR as well as terrestrial and Satellite AIS are reporting the same position of targets as can be observed in Figure 7 a. Figure 7 b shows the general limitation of terrestrial AIS covering only an area up to 40 km of the Cape Town area. Three small vessels are detected by SAR. One of them is reporting to the AIS system via satellite.

Next ship detection case study of the hijacked tanker ´Sirius Star´ is given. The hijacking of the super tanker MV Sirius Star by Somali pirates initiated a test of the response time of the TS-X data acquisition as well as the rapid tasking performance of the ground segment DLR-BN (Ground Station Neustrelitz, Germany) for monitoring the situation. The Supertanker was hijacked close to Somalia (Africa) on 18 November 2008 and was released on 9 January 2009. With the detected ship positions derived from large area ScanSAR and Stripmap search acquisitions, high resolution modes of TS-X at smaller coverage (Spotlight and High-Resolution Spotlight) were planned.

Figure 8 gives an overview and examples of the data quality (with reduced resolution).

Velocity estimation based on complex TS-X data has been demonstrated. In order to determine ship speed the object velocity is regarded as a vector with two components, one in azimuth and one in range direction. The algorithm consists of three main steps. The first step is the generation of a sequence of single–look SAR images followed by the detection of moving objects. This consists of the detection of ship candidates and the respective velocity estimation. The third step is the compensation of the object motion and the imaging of the moving objects. Two kinds of detection and estimation of speed of the moving objects are possible, either in a multi look image or in a sequence of single–look images. Figure 9 b-c show zooms of a sequence of two single-look images based on a TS-X complex image acquired on 9 June 2008 over the East coast of Florida. The estimated velocity of the ship is 12.2 knots with an error of 1.6 knots as compared to the 11.3 knots available from the AIS information. However, the time lag between the SAR acquisition and the AIS may allow for the difference.

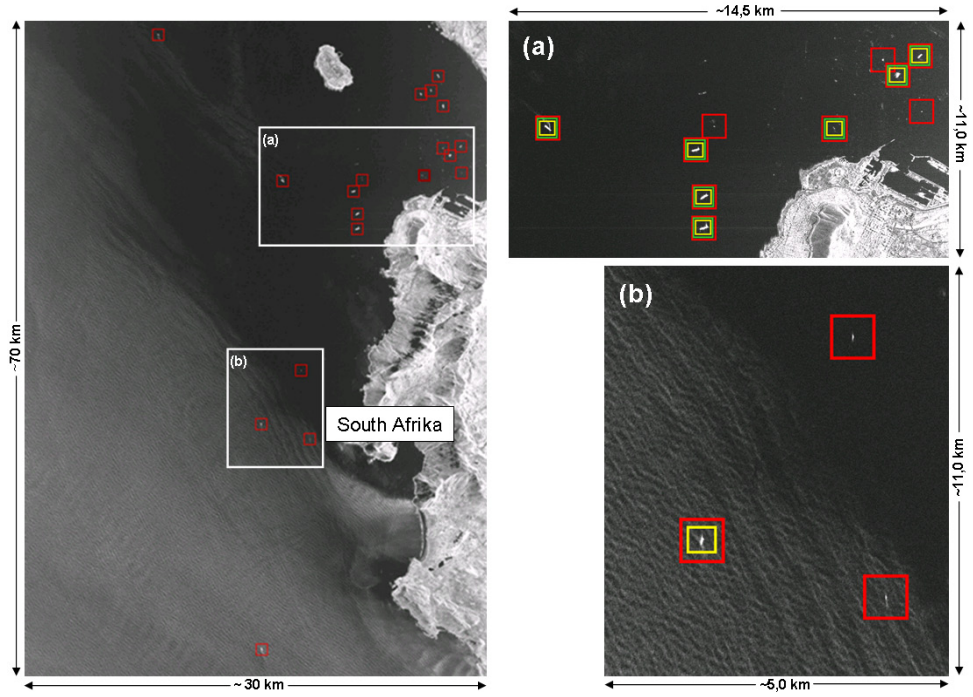

Fig. 7: TS-X Stripmap sub-image (HH-Pol, 3m resolution) acquired on 16 December 2008 over the southern Atlantic Ocean with ships detected by the DLR ship detection algorithm (red rectangles), superimposed AIS (source: IHS Fairplay) data with green rectangles, and Satellite AIS reports (yellow rectangles, source: Luxspace)

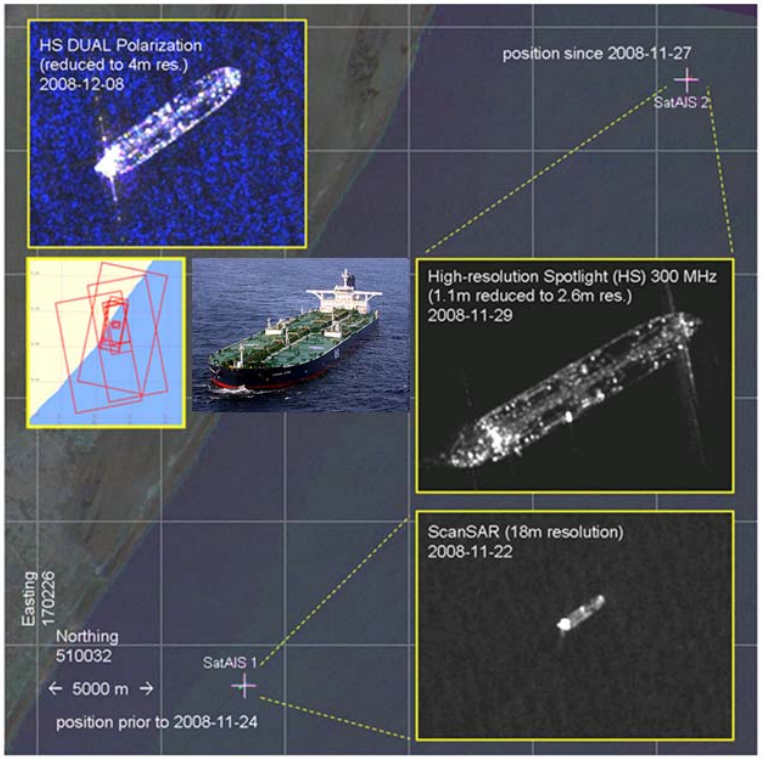

Fig. 8: Optical image and Colour composite of three TS-X ScanSAR acquisitions (red: 2008-11-27T15:04, green: 2008-11-22T03:02, blue: 2008-11-22T14:56) showing the position of the Sirius Star off Somali coast and its displacement. During the two acquisitions of 22 November, the ship was anchoring at the exact same position (yielding a cyan colour). The blow-ups are from three of the 16 single acquisitions with the footprints are indicated on the map plot. The AIS Coordinates retrieved later on are indicated by white crosses (source: LuxSpace).

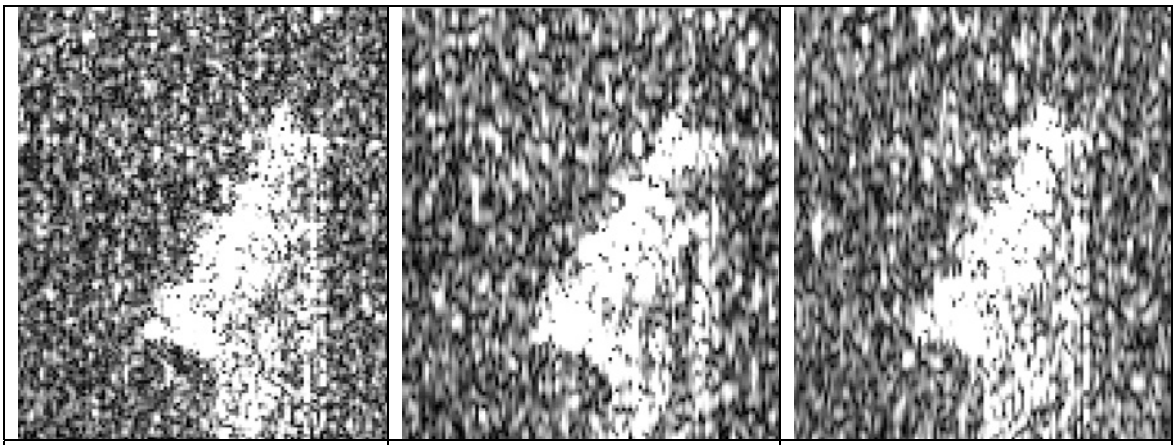

original image	(b) sub-look 1	(c) sub-look 2

Fig. 9: sequence of two single-look images based on a TS-X complex image on 9 June 2008 over the East coast of Florida.

2. Main Results:

The following points are the main results of this work:

- SAR systems can be used for validation of wind speed in high resolution numerical models during extreme weather
- The joint use of high resolution SAR and optical data allow detailed observation of turbulent exchange of large amounts of momentum between the ocean surface and atmosphere in the marine atmospheric boundary layer
- Distinctive atmospheric caused ocean surface signatures (e.g. from atmospheric cells) on SAR imagery and incorporated weather conditions can be analyzed by synergetic use of high resolution SAR and optical data
- High resolution X-Band systems (e.g., TS-X) provide the first time high resolution coastal bottom topography maps of up to 40m resolution measured by space based commercial SAR systems
- Small objects (<10m) can be observed by TS-X. Vessel monitoring reaches a higher level of accuracy and quality with TS-X
- TS-X ship detection algorithm was successfully integrated and tested in a Near Real Time chain at the DLR Ground Station Neustrelitz (Germany) and is currently in use for operational services

3. Outlook:

The used algorithm for wind speed retrieval provides more accurate high wind measurements (up to 30 m/s) than earlier algorithms. Future task are substantial algorithm improvements to achieve accurate wind measurements in strong or severe weather conditions.

Morphological changes in coastal areas, especially in river estuaries, are of high interest in many parts of the world. Satellite data from both optical and radar sensors will help to monitor and investigate these changes. Several polarization modes (dual, quad) for better separation of land and water areas are now available (TS-X, COSMO-Skymed, Radarsat 2) and will be used for further investigation.

The developed bathymetry retrieval model for SAR system has to be constantly improved and tested worldwide. The aim is the generation of a global

bathymetry map. Bathymetry products will be defined and delivered or will be made available for download.

Future tasks will have to improve ship detection techniques based on multi-polarization data from TS-X. The main advantage of using multi channel processing, with respect to a single channel, is that there is no need to segment or divide SAR spectrum to make the coherence analysis, this can instead be performed between the two channels. On the other hand, few multi channel satellites are currently available (e.g. TS-X, TD-X, Radarsat 2). Effort will be concentrated on Single Look Slant Range Complex (SSC) Dual Polarization data, but some experiments will also be done using the quad-polarised (Full) data.

Results have to be integrated to SAINT and the SAR oceanography toolbox (SEASAR) at DLR. The focus is on operational services for users, e.g., DWD, other national, and international authorities.

The work is complemented by two more publications as contributing author in peer reviewed journals:

[4] G.M. Diaz, S. Lehner, F. O.-Torres, X.M. Li, S. Brusch "*Wind and wave observations off the south Pacific coast of Mexico using TerraSAR-X imagery*" International Journal of Remote Sensing IJRS– in print

[5] A. V. Soloviev, M. Gilman, K. Young, S. Brusch, and S. Lehner (2009) "*Sonar measurements in ship wakes simultaneous with TerraSAR-X overpasses*". IEEE Transactions on Geoscience and Remote Sensing (TGARS), TerraSAR-X Special Issue; ISSN: 0196-2892; Page(s): 841 - 851

Danksagung/ Acknowledgments

Neben vielen Freunden und Mitmenschen, die alle auf ihre Art Anteil am Gelingen dieser Arbeit haben, möchte ich einigen besonders danken:

Mein Dank gilt Herrn Prof. Dr. Hartmut Grassl, für die Ermöglichung der Arbeit im Rahmen des Virtuellen Instituts “EXTROP” der Helmholtz-Gemeinschaft. Anregungen und Hilfen waren immer ein verlässlicher Kompass im Verlauf dieser Arbeit.

Mein Dank gilt auch Herrn Prof. Dr. Richard Bamler, Leiter des Instituts für Methodik der Fernerkundung am DLR, für die stetige Unterstützung und Ermöglichung der Arbeit.

Frau Dr. Susanne Lehner möchte ich an dieser Stelle besonders herzlich für die fortlaufende Unterstützung und den Einsatz bei der Betreuung dieser Arbeit danken. Ihr Wirken, ihre Geduld, viele Diskussionen und gute Hinweise, waren für den Fortgang und Beendigung dieser Arbeit außerordentlich hilfreich. Ihr Rückhalt während aller Höhen und Tiefen in den vergangenen Jahren hat einiges leichter gemacht.

Herr Dr. Andreas Neumann hat in den letzten Jahren jegliche Unterstützung als Abteilungsleiter der Gewässerfernerkundung am DLR geleistet, die zum Gelingen der Arbeit beitrug. Vielen Dank!

Ein weiterer Dank geht an meinen ehemaligen Kollegen Johannes Schulz-Stellenfleth. Seine Unterstützung in den ersten Monaten meiner Arbeit legte die Grundlage für daraufhin erreichte wissenschaftliche Ergebnisse. Seine große Begeisterung und sein Wissenshunger waren mir ein steter Antrieb und Vorbild. Gespräche und Diskussionen mit ihm waren ein Schlüssel zum Gelingen dieser Arbeit.

Meinen Kollegen aus der Gewässerfernerkundung des DLR danke ich für die freundliche und konstruktive Arbeitsatmosphäre.

Ich danke den ehemaligen Kollegen des Instituts für Weltraumwissenschaften, der Meteorologie an der FU-Berlin und Dr. Thomas Bruns vom DWD für Diskussionen und Datenbereitstellung aller Art.

Diese Arbeit widme ich meinen Eltern, Ingeborg und Günter Brusch, die mich bei jeglichen Entscheidungen in den letzten Jahren unterstützten und verteidigten.

Nomenclature

AIS	Automatic Identification System
ASAR	Advanced Synthetic Aperture Radar
CFAR	Constant False Alarm Rate
DEM	Digital Elevation Model
DLR	Deutsches Zentrum für Luft- und Raumfahrt
DLR-BN	DLR Ground Station Neustrelitz, Germany
DWD	Deutscher Wetterdienst
ENVISAT	Environmental Satellite
ESA	European Space Agency
HIRLAM	High Resolution Limited Area Model
HS	High Resolution
LM	Local Model
MABL	Marine Atmospheric Boundary Layer
MERIS	Medium Resolution Imaging Spectrometer
MODIS	Moderate Resolution Imaging Spectroradiometer
MSG	Meteosat Second Generation
NOAA	National Oceanic and Atmospheric Administration
NRT	Near Real Time
SAINT	SAR AIS Integrated Toolbox
SAR	Synthetic Aperture Radar

SSC	Single Look Slant Range Complex
TD-X	TanDEM-X
TS-X	TerraSAR-X
UTC	Coordinated Universal Time
WSM	Wide Swath Mode

Appendix

Full Versions of Publications

Synergetic Use of Radar and Optical Satellite Images to Support Severe Storm Prediction for Offshore Wind Farming

Stephan Brusch, Susanne Lehner, and Johannes Schulz-Stellenfleth

***Abstract*—In this paper, we show how satellite images taken by space-borne radar sensors can be used to determine mesoscale high-resolution wind fields in synergy with cloud parameters from optical data and, thus, help in the task of maintenance and planning offshore wind farms. The aim of this paper is to use synthetic aperture radar (SAR) and medium resolution imaging spectrometer (MERIS) onboard the environmental satellite (ENVISAT) in synergy to analyze severe weather systems, in particular, to describe the spatial evolution of the atmospheric boundary layer processes involved in cold air outbreaks. We investigated the fine-scale structure of a severe weather case on November 1, 2006 over the North Sea using satellite data. The satellite data are compared with numerical model results of the German Weather Service "Lokal Modell" (LM) and the high-resolution limited area model (HIRLAM). LM and HIRLAM show differences in mesoscale turbulent behavior and coastal shadowing. Maximum wind speeds of up to 25 m/s are measured by SAR and are confirmed by the models. Significant differences are observed in the location of the maxima. High-resolution ENVISAT ASAR measurements provide very detailed information on small-scale atmospheric features, which seem to not be captured well by the analyzed numerical models, in particular, in coastal areas. Meteosat second generation (MSG) is used to determine the movement of cloud patterns. Cloud patterns seen in the optical data and radar cross-section modulation give a consistent dynamical picture of the atmospheric processes. The relevance for offshore wind farming is discussed.**

***Index Terms*—Synergy, synthetic aperture radar (SAR), wind energy, wind field.**

I. Introduction

TO plan offshore wind energy exploitation, an assessment of the respective wind resources is necessary. Previous studies have shown that the mean wind speed is higher in offshore regions [1] compared to land sites. It has also beenshown that temporal variability of wind speed on diurnal timescales [2] has implications on wind energy extraction. Relatively little work has been done on the use of remote sensing data to study the impact of short scale wind field variations on offshore wind park operations (e.g., [3]). In this study, the focus is on the investigation of highly dynamical extreme weather events, which play an important role in wind turbine operations. The most important issues in this context are:

- increased fatigue loading and, thus, shorter lifetime due to turbulence;
- turbines are switched off when the wind speed exceeds a certain limit;
- increased risk that turbines are damaged;
- maintenance of turbines is getting more difficult;
- using a suitable turbine design, the energy contained in extreme events could be exploited.

To investigate dynamical processes of this kind, a dense spatial and temporal data sampling is desirable. Offshore wind information from *in situ* measurements is sparse. Remote sensing helps to develop more comprehensive and spatially resolved datasets over the oceans. While *in situ* observations from offshore platforms and coastal stations yield time series of wind speed and direction, satellite images yield synoptic observation of an area of up to 400 $\times$ 400 km. Upcoming satellites, e.g., Constellation of small Satellites for Mediterranean basin Observation (COSMO-Skymed) can increase the temporal resolution of space borne retrieved surface wind fields.

The SAR derived information can support offshore wind farming with respect to optimal siting and design and help to estimate their effects on the environment. SAR derived high-resolution wind fields enable the synoptic extraction of wind speed and wind direction for any offshore site located in the scene. Based on these measurements estimates of the energy yield at the respective offshore location and comparisons of wind conditions at different sites are possible.

This study concentrates on the analysis of an extreme weather event which occurred in the North Sea. A lot of offshore wind farm activities are currently ongoing in the North Sea leading to a big demand for respective geophysical information. Fig. 1 shows the QuikSCAT [4] and ENVISAT advanced synthetic aperture radar (A)SAR wide swath mode (WSM) derived wind field and wind direction in the North Sea on November 1, 2006. The locations of some already operating and planned offshore wind farms are superimposed.

Since the launch of the European Remote Sensing satellites ERS-l in 1991 and the subsequent platforms ERS-2, RADARSAT-1 SAR images have been acquired over the oceans on a continuous basis. Their independence on daylight and all-weather capability together with their high resolution

Manuscript received March 11, 2008; revised June 23, 2008. First published September 30, 2008; current version published October 15, 2008. This work was supported in part by the framework of the EXTROP project and Helmholtz Research Network "Integrated Earth Observing System" Helmholtz-EOS and in part by the Helmholtz Association of German Research Centers (HGF) in the framework of the virtual institute EXTROP and the research network IEOS.

The authors are with the Remote Sensing Technology Institute, German Aerospace Center (DLR), D-82234 Wessling, Germany (e-mail: stephan.brusch@dlr.de).

Color versions of one or more of the figures in this paper are available online at http://ieeexplore.ieee.org.

Digital Object Identifier 10.1109/JSTARS.2008.2001838

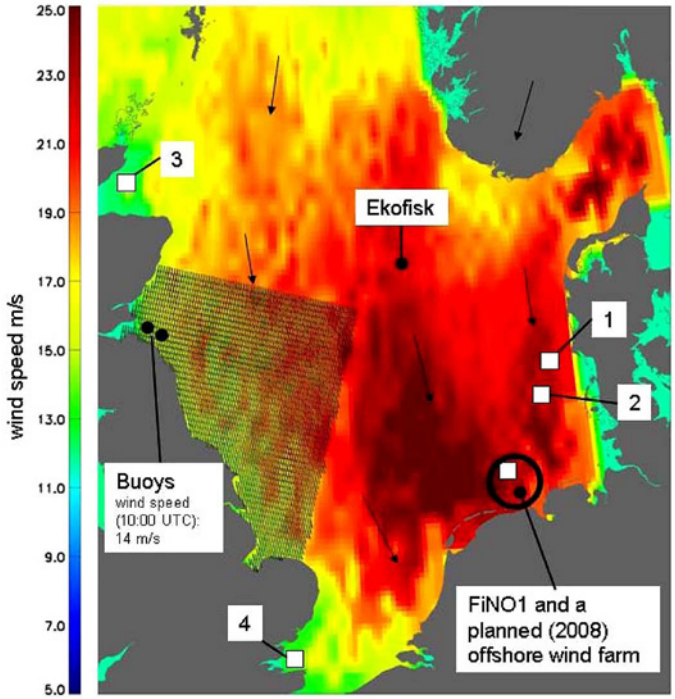

Fig. 1. Overview North Sea area. Background: QuikSCAT u10 wind field morning pass. ENVISAT ASAR wide swath mode (400 × 400 km size) derived wind field on November 1, 2006 at 10:42:28 UTC (rectangle with wind arrows). Buoys wind speed Measurement at 10:00 UTC (both 14 m/s). Platforms FiNO 1 and Ekofisk. Offshore wind farms (1: Horns Rev; 2: Butendiek; 3: Beatrice Field; 4: Thanet Scheme). Wind direction marked by black arrows.

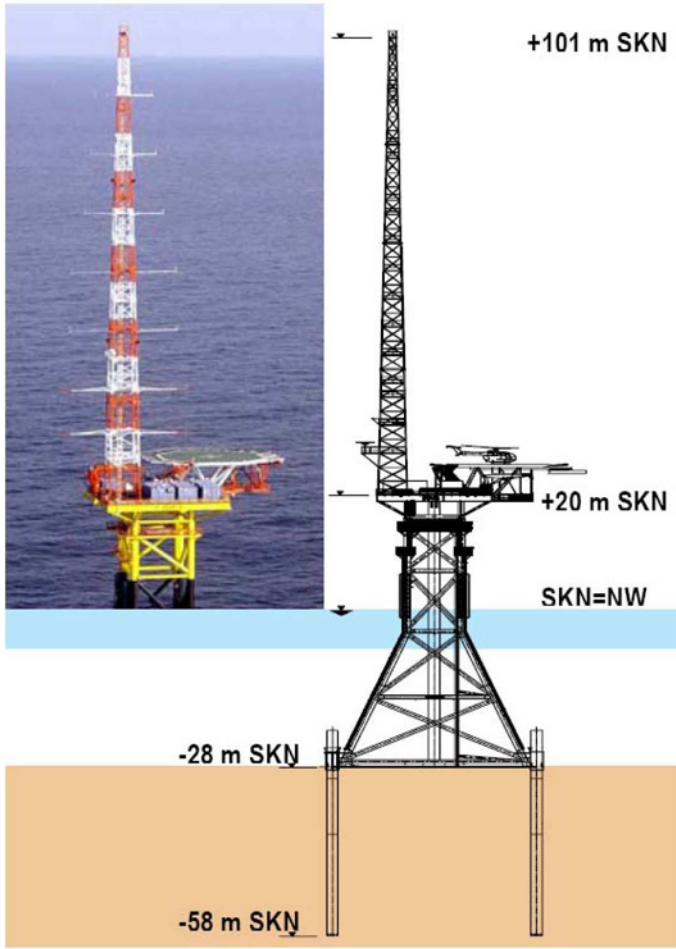

Fig. 2. FiNO 1 research platform (N54° 0.86′; E6° 35.26′).

and large spatial coverage make them a valuable tool, especially in coastal areas for measuring geophysical parameters such as ocean surface winds and sea state [5].

Radar reflectivity over the ocean depends on the roughness of the sea surface and, thus, mainly on the wind field as described in [6]. Additionally, the backscatter of the radar signal is influenced by the size of hydrometeors, e.g., rain drops or snow in the atmosphere and their precipitation rate. It is important to study effects by precipitation on radar reflectivity. Optical data are used to detect clouds, and, thus, these data are needed to investigate atmospheric impacts, e.g., in cold air outbreaks.

An overview how satellite images acquired by space-borne radar sensors can be used to determine mesoscale wind fields and, thus, help in the task of planning offshore wind farms is, e.g., described in [7].

The main goal of this paper is to show that a combination of optical and radar satellite data is an efficient technique for the analysis of extreme events. Such phenomena are hard to predict by numerical models and are easily missed due to resolution effects and other deficiencies of the model.

We selected the case of the Storm Britta in November 2006 for our study to investigate both oceanographic and atmospheric processes. The study demonstrates the benefit of SAR derived high-resolution wind fields in the analysis of such extreme atmospheric events.

This paper is organized as follows. Section II gives a meteorological overview of the case study presented. Section III summarizes the SAR wind field retrieval scheme, used in the study. Furthermore, an introduction to cloud products from MERIS and MSG is given, and the high-resolution numerical models COSMO/EU, LM, and HIRLAM are described. Additionally, images from different satellites are used in synergy to explain the fine scale structure of the observed atmospheric processes. In Section IV, the presented case study and the wind field is discussed and a comparison to results from LM and HIRLAM is given.

II. Case Study Britta

The deep pressure system “Britta” developed initially from a frontal wave of low pressure in the central North Atlantic early on October 28, 2006 and, after moving northeast, turned further east and developed hurricane-force northwest winds on its western side as it passed through the North Sea. High sea state measurements by the research platform FiNO 1 (see Figs. 1 and 2) were observed. An example of significant wave height (red line), wave period (blue line) and direction (orange line) measured by a waverider buoy is shown in Fig. 3. The record shows that a maximum significant wave height up to 10 m was measured during the severe weather event “Britta” in the morning of November 1, 2006 at 04:00 UTC. Individual wave height reached up to 18 m and damaged the platform at this level (see Fig. 4).

The map in Fig. 5 shows the surface weather analysis for November 1, 2006 at 06:00 UTC. Northwesterly winds over

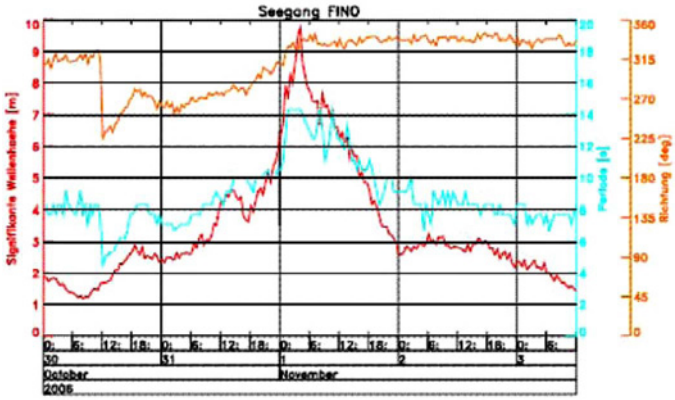

Fig. 3. Significant wave height (red line) measured at FiNO 1 (source: German Weather Service, DWD).

Fig. 4. Steel-bridge at the FiNO 1 research platform damaged by ocean wave crest 18 m above normal sea level (source: German Weather Service, DWD).

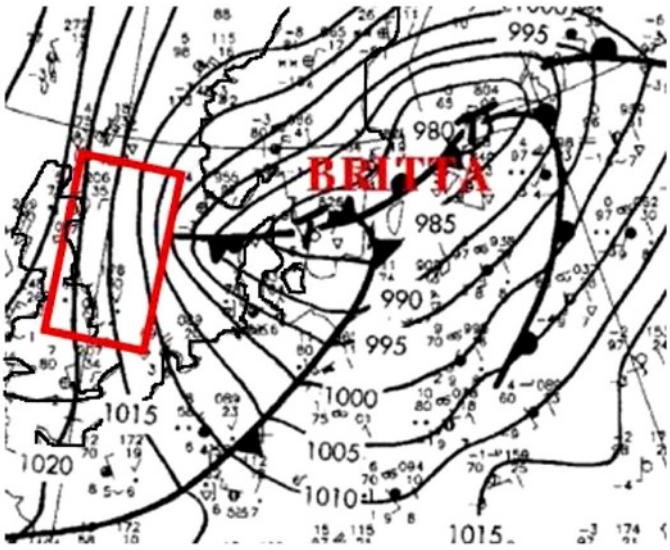

Fig. 5. Surface weather analysis from November 1, 2006 at 06:00 UTC (source: German Weather Service, DWD).

the North Sea increasing from west to east over 25 m/s were observed. The red rectangle marks the acquisition area of ENVISAT ASAR and MERIS taken at the same time.

The wind speed reached force 28 m/s with gusts of up to 43 m/s. At 18 UTC October 31, 2006, the buoy 62138 (58.2 N 1.8 W) reported northerly winds of 31 m/s maximum speed, buoy 63110 (59.5 N 1.5 E) reported north max winds of 28 m/s from the north. Six hours later the platform XP421 (55.5 N 5.0 E) encountered north west winds of 31 m/s while the storm center was moving east of the satellite aquisition area [8]. Britta

Fig. 6. Meteosat Second Generation (MSG-1) true color composite acquired on November 1, 2006 at 10:00 UTC.

caused the highest-ever measured water level above Normal Amsterdam Water Level (NAP), which occurred just at the moment of the high tide in Delfzijl (NAP + 4.83 m, Knock close to Emden NAP + 3.60 m or Borkum NAP + 2.70 m) on the morning of November 1. Britta caused individual wave heights up to 18 m at FiNO1. Parts of the port of Hamburg had to be closed because the streets were flooded and the level of the River Elbe was 5 m (16 ft) above normal.

On the morning of November 1, 2006, boundary layer roll convection occurred over the North Sea due to the cold air outbreak. The general convective nature of the flow is caused by cold air flowing over a warm sea surface. If the boundary layer exceeds the height of the lifting condensation level, then the roll circulation is forming so-called cloud streets that can be seen as shown in Fig. 6.

These rolls are generated by thermal or dynamical (inflection) instability of the basic flow as described in [9]–[12]. These two kinds of instabilities may act independently, but are difficult to detect. Information on the wind speed at the sea surface associated with the boundary layer rolls can be obtained from the radar image intensity of satellite images. Thus, from SAR data the gustiness of the wind field can be determined to a high degree of spatial accuracy. The technique is described in the next chapter.

III. Analysis of Britta With Satellite Earth Observation (EO) and Model Data

The detailed investigation of highly dynamical atmospheric phenomena, such as storms, requires measurements with a high temporal and spatial resolution in both vertical and horizontal dimension. SAR gives information about the wind field with high horizontal resolution. MERIS provides information on the vertical structure of the atmosphere, e.g., cloud patterns in a specific region at a certain time. MSG provides data at 15-min time steps to estimate the cloud propagation direction.

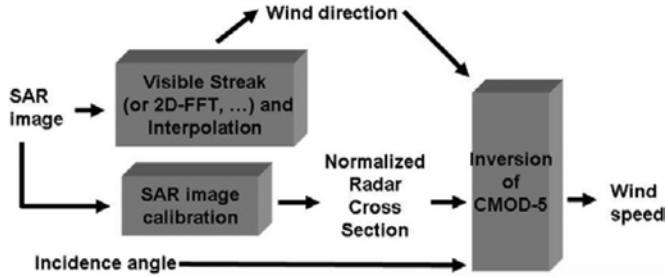

Fig. 7. Flowchart of the wind field retrieval scheme.

IV. Envisat SAR Wind Retrieval Using an Interpolation Technique

The wind field can be derived from ENVISAT ASAR scenes, which gives the possibility to measure synoptically spatially variable wind fields at high resolution and large coverage, which is especially useful for coastal areas. Wind speed is derived from SAR data using a geophysical model function, CMOD 4 or 5 referred to [13], relating the NRCS of the ocean surface to the local near surface wind speed. As further input into the algorithm wind direction versus antenna look direction and incidence angle is needed. A flowchart of the wind field retrieval scheme is shown in Fig. 7. Streaks observed on SAR images yield information about wind direction, these linear features are usually associated with boundary layer rolls, referred to as atmospheric roll vortices. Wind direction can be determined from the image by searching for the dominant wind streak direction in the spectral domain by fast Fourier transformation (FFT). In the low frequency range of the spectra at 600 m to about 2 km. Roll vortices create more spectral energy in the direction perpendicular to the wind. Obviously this FFT method will work only for images in which the streaks are detectable above a certain threshold. In areas, where this is not the case, e.g., due to sea surface features caused by precipitation, in the SeaSAR algorithm wind direction is interpolated using sine and cosine functions in two dimensions. [14]. Fig. 8 shows the SAR retrieved wind field obtained on November 1, 2006 at 10:42 UTC.

V. Meris Cloud Products and Cloud Classification

The focus here is on the influence of clouds and rain on SAR radar cross section (RCS) measurements. MERIS is used to determine physical cloud properties. Cloud-particle phase (i.e., ice versus water), effective cloud-particle radius, and cloud optical thickness are derived using the MERIS visible and near-infrared channel radiances.

Cloud top pressure (CTP) retrieval from MERIS is based on radiation backscattered in the O2-absorption band by the method described in [15] and [16]. The physical basis of the cloud optical thickness retrieval is described in [17]. In Fig. 9, the true color composite obtained from the MERIS data acquired on November 1, 2006 is shown.

VI. Meteosat Second Generation (METEOSAT-8) Derived Atmospheric Motion Vectors (AMV)

We want to use sequences of MSG images (15-min time step) to determine the southward motion of cloud patterns as shown in Fig. 10 and, thus, to estimate downward momentum fluxes (see Section IV) due to high wind speed in the mid level layers of the atmosphere. By tracking the movement of cloud fields, wind speed can be extracted. The height of the clouds is determined from the infrared temperature and converted to pressure using an ECMWF forecast profile. Atmospheric Motion Vectors

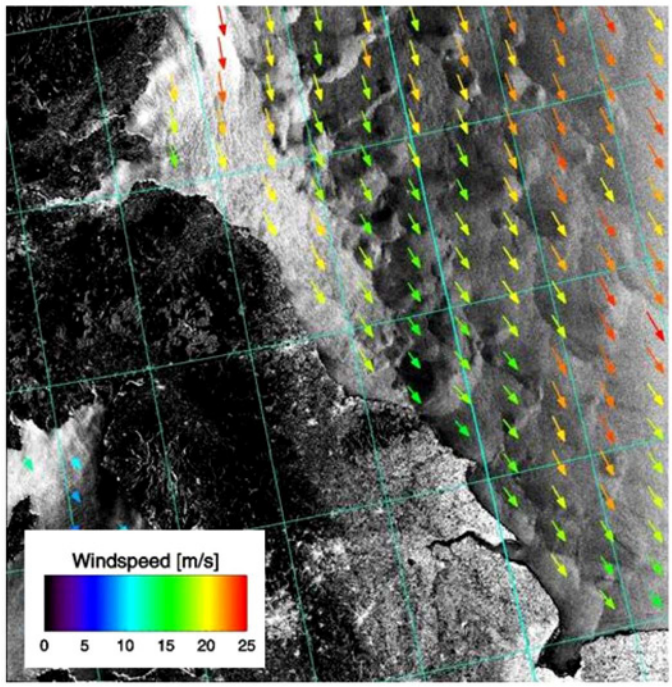

Fig. 8. ENVISAT ASAR WSM derived wind field on November 1, 2006 at 10:42 UTC.

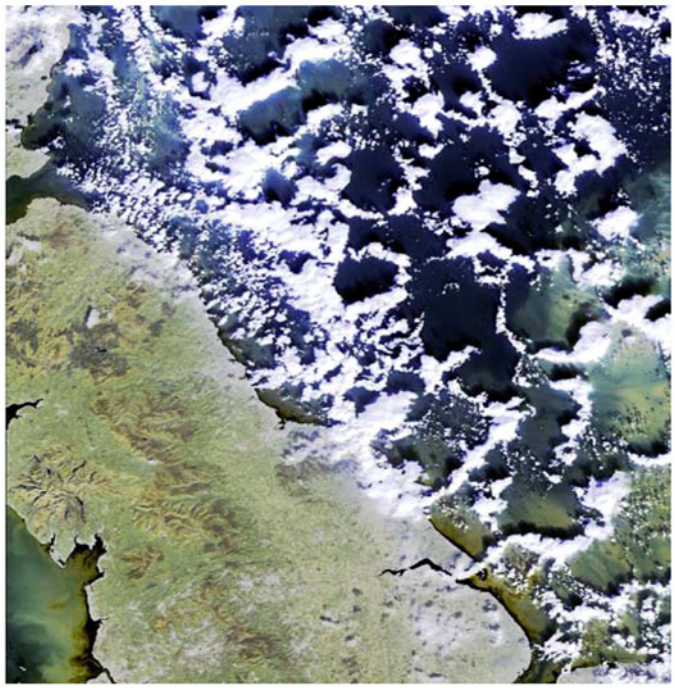

Fig. 9. MERIS FR true color composite acquired on November 1, 2006 at 10:42 UTC.

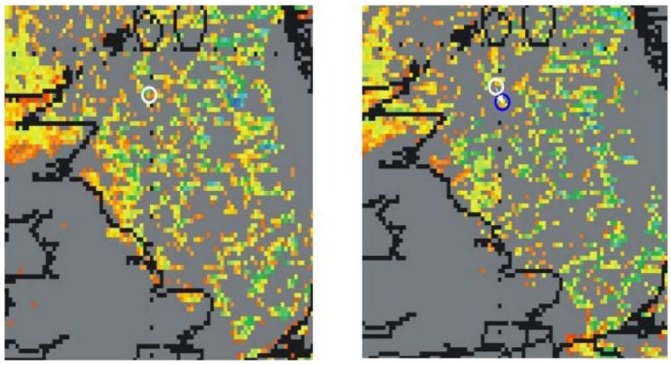

Fig. 10. MSG detected clouds (left: November 1, 2006 at 09:00 UTC, right: November 1, 2006 at 10:00 UTC) and moving cloud patterns marked with circles (white: start point, blue: movement after 1 h).

(AMVs) are currently produced operationally with data from the Meteosat first and second generation satellite series.

The aim here is to investigate moving cloud patterns as observed by the optical data and the radar cross section modulation in SAR images.

VII. Wind Fields and Precipitation From Numerical Models

To estimate precipitation intensity of the clouds, the German Weather Service COSMO/EU model provides total convective and stratiform precipitation rates. The present operational setup is at a meso-â scale using a grid spacing of 7 km [18]. The meso-â scale is resolving convection patterns like in the case of Britta.

For validation the LM wind field is used. LM is a nonhydrostatic numerical model used for operational weather prediction. LM is nested in GME (Global Model Europe) and uses a moisture convection schemefollowing [19]. The turbulence scheme for the planetary boundary layer is based on prognostic turbulent kinetic energy (TKE) following the approach described in [20]. For the North Sea area, LM was set up with a resolution of 7×7 km.

The high-resolution limited area hydrostatic model HIRLAM is a numerical weather prediction (NWP) model and is used for validation, too. The convection scheme currently used is based on the Kain and Fritsch scheme [21], which was originally designed for mesoscale convection. The present turbulence scheme is based on a prognostic TKE scheme. For the North Sea area it was set up with a resolution of 11×11 km.

The most important difference of LM and HIRLAM in the context of this study is the fact that LM is nonhydrostatic whereas HIRLAM is a hydrostatic model. Furthermore LM has a higher spatial resolution. Nonhydrostatic models resolve more convection patterns in the boundary layer. Furthermore higher variability of the surface wind field at the macroscale is observed in such models. In Fig. 11, the North Sea wind fields computed with LM and HIRLAM are shown for 9:00 UTC. It is evident that LM shows more spatial details. For this reason we concentrate on LM wind speed in the next sections, but give as well the HIRLAM results.

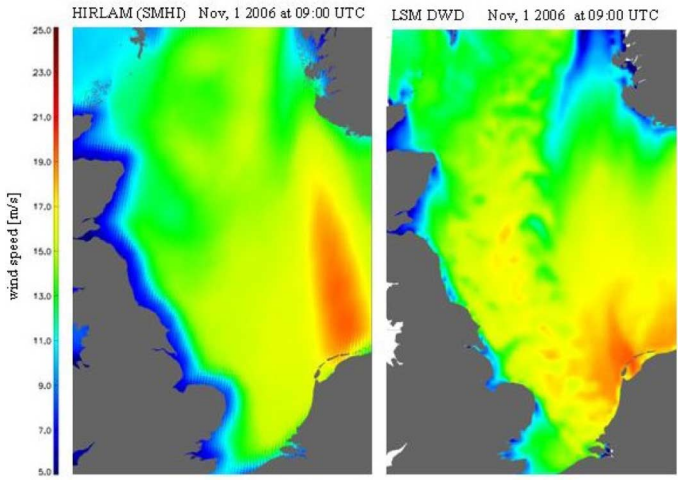

Fig. 11. Surface wind speed forecast as computed by the numerical models HIRLAM (left) and LM (right) for November 1, 2006 at 09:00 UTC.

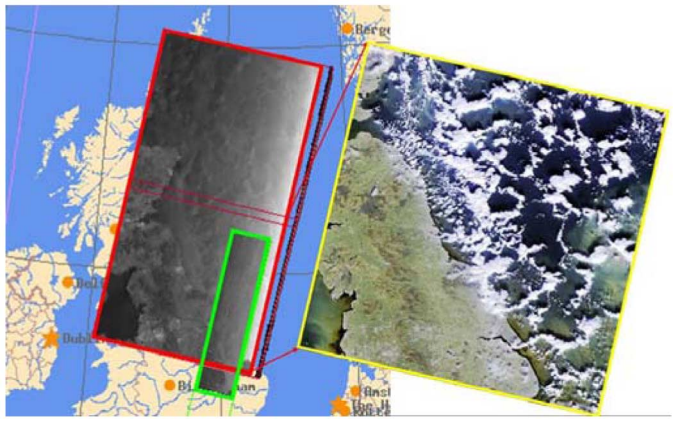

Fig. 12. Synergetic use of remote sensing data (red—microwave: ENVISAT ASAR WSM, green—microwave: ERS-2, yellow—optical: MERIS FR true color composite, background blue: North Sea—model domain, background land surface: Great Britain).

VIII. Synergy of Radar and Optical Data

The marine atmospheric boundary layer (MABL) has direct contact to the ocean and is, thus, strongly influenced by it. The MABL and the ocean exchange large amounts of heat, moisture, and momentum. Couplets of cellular updrafts and downdrafts (cells) and couplets of roll-like updrafts and downdrafts (rolls) in the MABL cause these fluxes. Cells and rolls each have distinctive signatures on the ocean surface. The signatures are the result of the alteration of the ocean surface roughness resulting from wind gusts [22]. Mesoscale wind systems, e.g., downbursts due to clouds increase the sea surface roughness.

The special weather situation in the morning of November 1, 2006 over the North Sea is well captured both in optical and microwave data (see Fig. 12). Typical postfrontal scattered cloud patterns with embedded convective individual clouds with a diameter up to 10 km are observed. For synergetic investigation a nearest neighbor method for the co-registration of ENVISAT ASAR WSM and MERIS scenes was implemented.

From satellite images, the spatial and temporal distribution, as well as intensity, of cells and rolls can be derived. In the

following, we will show that cloud patterns seen in optical data are strongly correlated with the sea surface roughness features observed in the co-located SAR imagery.

The objective of this study is to determine whether the cellular patterns on the SAR images are due to strong wind gusts or precipitation. Radar backscatter is influenced by rain drops impinging on the sea surface and is correlated with intensities of the radar backscatter. In general, rain events are associated with wind gusts that roughen the sea surface and increase the image intensity. A reason for image darkening is the rain-induced turbulence by impinging hydrometeors dampening the Bragg waves on the sea surface.

To investigate the rain effect, we construct a rain discriminating mask from MERIS and COSMO/EU data and superimpose it on the SAR image. For this study, MERIS cloud derived parameters and ISCCP cloud statistics are used. Precipitating clouds need both large enough droplets and large enough vertical extension. We can not retrieve droplet size and cloud thickness directly with optical data. It is well known that under simplifying assumptions these parameters are strongly correlated with effective cloud droplet radius and the optical thickness. These parameters are, thus, used as substitutes in this study. In the first step cloud affected MERIS pixels are superimposed on the respective ENVISAT ASAR WSM pixels. In the second step we used effective cloud droplet radius and the optical thickness to retrieve cloud properties. The retrieval is based on a semi-analytical cloud algorithm (SACURA) which is explained in [23]. This technique is only applicable in middle latitudes and gives a probability of precipitation. The retrieval of precipitation intensity is based on COSMO/EU forecasts. Model results are compared to MERIS cloud covered and precipitating pixels. Combining all this information cloud covered pixels with precipitation probability higher than 45% are detected.

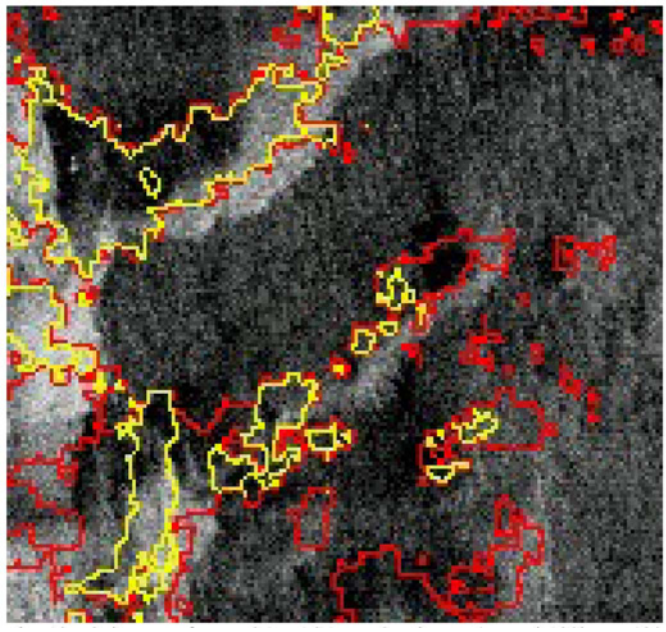

Fig. 13. Subscene of ENVISAT ASAR WSM image (around 120×120 km) acquired on November 1, 2006 at 10:24 UTC (red contours: clouds > 750 hPa, yellow contours: raining clouds, greyscale: RCS).

IX. Interpretation of the Retrieved Wind Ield

In Fig. 8, the SAR retrieved wind field over the North Sea acquired on November 1, 2006 is shown. The retrieved wind field fits very well to the surface weather analysis and observations as shown in Fig. 5 wind speed is increasing from west to east up to 23 m/s and lower wind speed at the coast of England down to 10 m/s. Buoy measurements with 14 m/s at 10:00 UTC (see Fig. 1) agree quite well with SAR retrieved wind speed of around 16 m/s at 10:42 UTC. Fig. 8 shows distinct features in the SAR backscatter perpendicular to the main flow. To investigate these features satellite cloud data are used. This weather situation is influenced by structures of cloud clusters that are organized in postfrontal low-pressure systems. Such postfrontal cloud clusters can develop into convective systems within few hours and can even cause intense convective precipitation and gale force winds.

To investigate the SAR retrieved wind field the MERIS Full Resolution Level 2 product and model data are used. Postfrontal precipitation bands are detected due to mixing of satellite cloud data and COSMO/EU total precipitation data (convective and stratiform). Fig. 13 shows a subscene of ENVISAT ASAR image (around 120×120 km) and superimposed clouds (red lines) with a rain probability higher than 45% marked with yellow lines. Precipitation rates are between 0.1 mm/h up to 2 mm/h. The observed variability of NRCS in Fig. 13 cannot be explained by such low precipitation intensities. Bright areas show rough sea surface (strong winds) ahead of observed cloud patterns, which can only be explained by downdrafts due to the convective cloud wind system.

Different explanations for the high surface wind in front of the cloud patterns are possible. One possibility is convective outflow as a result of downward acceleration associated with negative buoyancy resulting from evaporative cooling of cloud water [24] or acceleration due to perturbation pressure gradient forces. These effects could be increased by downward transport of strong horizontal momentum in a downdraft [25].

To assess the outflow in more detail, a thermodynamic and kinematic profile is investigated. The sounding that best represents the environment of the convection is the one from the Ekofisk 00 UTC given in Fig. 14 (also see Fig. 1). It was located amidst the polar air mass in which the convection occurred (56.52 N, 3.22 W). Based on the precipitation analysis in Fig. 13 and the Ekofisk sounding, the top of the convectively mixed layer was located near the 700 hPa level at the time of the analysis. In this case, of well-mixed air masses, the thermodynamic profile was practically neutral. The convection is forced by advection over the warm surface and convection was imbedded in a very strong wind field as revealed by the Ekofisk 00 UTC sounding data. The northwesterly winds increased from 30 to 36 m/s within the lowest 600 m above the surface, with a further increase to 42 m/s in about 2000 m. The major dynamics, therefore, taking place on the mesoscale. The structure of this system appears to represent a “shallow” and “miniature” version of well organized mid-latitude warm-season linear convective systems. In these, evaporative cooling due to precipitation

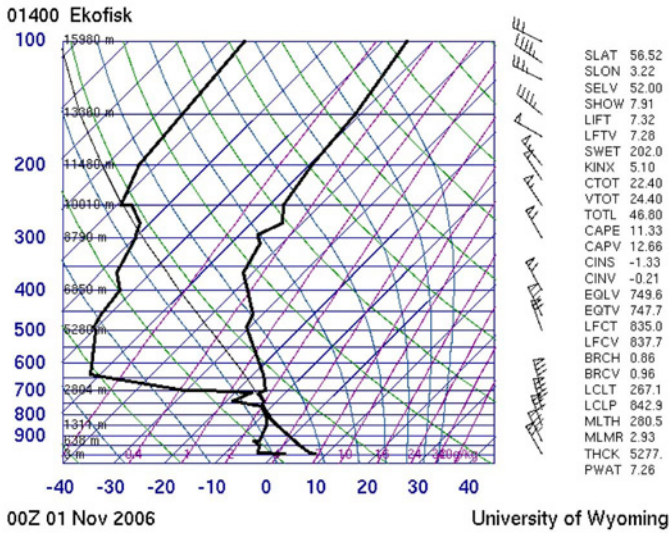

Fig. 14. Ekofisk radio sounding acquired on November 1, 2006 at 00:00 UTC.

along with downward momentum transfer in the downdrafts result in strong outflow winds [26].

As the downward air parcel with negative buoyancy descends toward the surface, it has a horizontal component of the magnitude of the upper-level rear inflow wind. This effect generates a corresponding horizontal momentum in the descending parcel. The resultant divergent outflow is enhanced by the parcel's horizontal momentum. It is proposed that these resulted in strong convective outflow ahead of the small and shallow convective line.

In the case of sparse radio soundings, an estimate of horizontal momentum can be retrieved using geostationary satellites as described in Section IV. To estimate downward momentum fluxes of southward moving clouds the MSG cloud top pressure product is used [27]. In Fig. 10, the cloud top pressure over the North Sea area at 9:00 and 10:00 UTC is shown. The forward speed of cloud patterns can be used to estimate the enhanced downward wind speed. In Fig. 10, the white circle marks a cloud pattern observed at 09:00 UTC. The blue circle marks the same pattern one our later at 10:00 UTC. The cloud system is moving with the average speed of the environmental air masses with up to 40 m/s southward. The northwesterly ambient wind field and the southward moving clouds are producing gusty winds in front of the observed clouds and lead to an addition increase in ocean wave height. This is an important factor in constructing wind turbines.

Figs. 15 and 16 show a cut through a cloud pattern perpendicular to the wind direction with embedded convective clouds with of a diameter up to 13 km. The main wind direction is from north to south. This cloud pattern is precipitating. From north to south an increase in wind speed of 5 m/s is observed. Footprints of these cloud-bands with cloud outflows (downward winds) ahead of convective lines are detected on the radar image of the sea surface (see Fig. 16) due to roughening of the sea surface. The presented results, e.g., strong convective outflow ahead of convective cloud patterns are not present in either of the numerical atmospheric models and can be used to improve or validate them.

In the following, the SAR and QuikSCAT retrieved wind field is compared to numerical model data and *in situ* measurements.

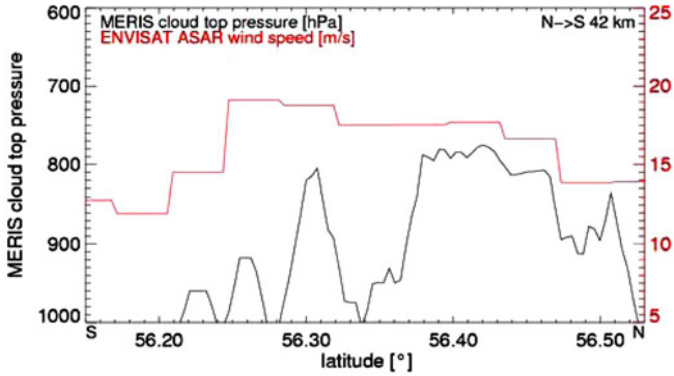

Fig. 15. Cut along the blue line of Fig. 16 showing MERIS ctp and ENVISAT ASAR wind speed.

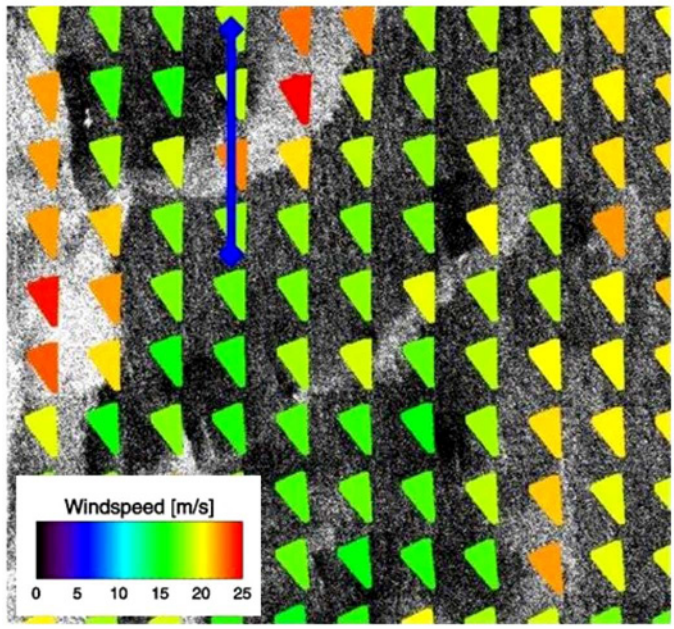

Fig. 16. Subscene ENVISAT ASAR WSM (120 km × 120 km) derived wind field on November 1, 2006 at 10:42 UTC. Blue line: see Fig. 15.

X. Comparison of SAR Retrieved Wind Field With Numerical Model Data

Fig. 11 shows the wind speed at 10 m as given by LM (7 × 7 km) and HIRLAM (11 × 11 km) over the North Sea on November 1, 2006 at 09:00 UTC. Following the analysis given in Fig. 5, the wind direction is roughly parallel to the isobars. In the upper (north) part of Fig. 11 north easterly wind is observed. Going south the wind is turning into a northwesterly direction. Both models give a maximum wind speed of around 25 m/s close to the northern coast of the Netherlands and Germany. The predicted wind fields in terms of maximum values agree quite well with the DWD analysis as shown in Fig. 5 (weather map).

The high-resolution numerical model HIRLAM and LM wind field show large differences between each other as well in intensity of the wind speed as in the spatial structure. In addition large differences to satellite validation data both from scatterometer and SAR exist. In particular the effect of topography does not seem to be well captured by the models.

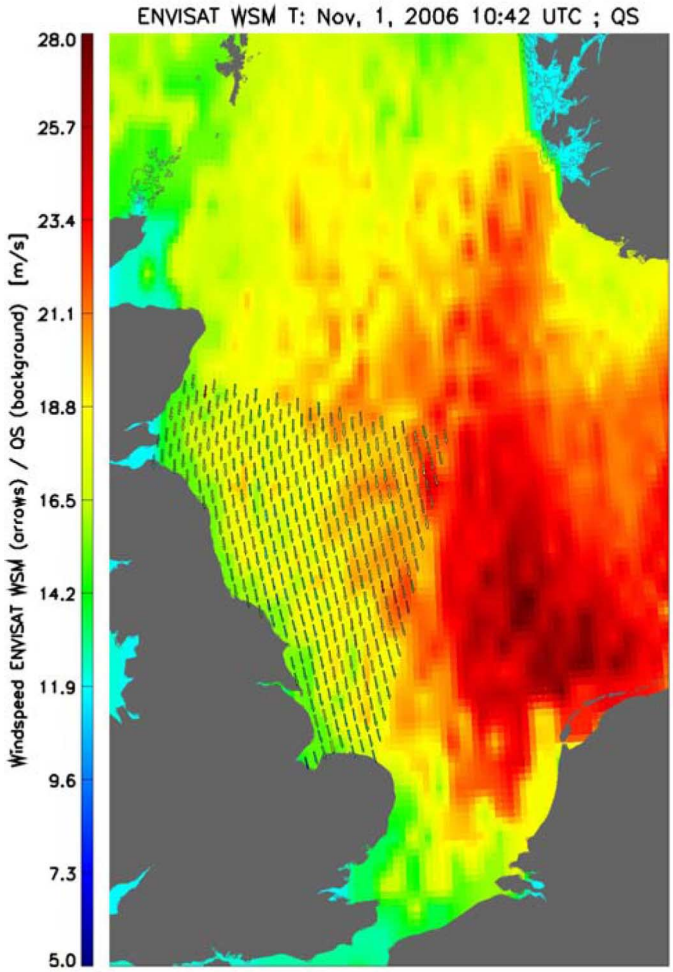

Fig. 17. QuikSCAT surface wind field acquired on November 1, 2006 and superimposed ENVISAT WSM wind field (arrows); see scenes in the following figures.

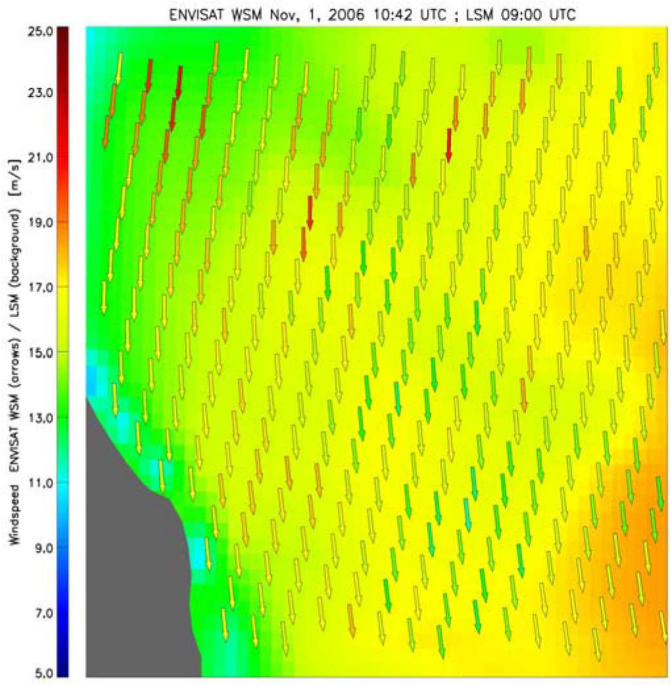

Fig. 18. Wind field LM model input (background). The ENVISAT ASAR wind field is superimposed by arrows (colored at the same scale as the model).

Another effect observed in the SAR data is the high variability of the wind field organized in cellular structures. Differences of up to 10 m/s can be observed regarding the spatial distribution of wind speed especially in coastal zones, e.g., in the south of the Norwegian coast. Fig. 17 (QuikSCAT) give the QuikSCAT scatterometer derived wind field. The difference between the models and QuikSCAT in coastal shadowing areas is clearly visible. South of Norway a shadowing effect with low wind speed behind the coast is observed. QuikSCAT measurements show a more structured wind field, too. This can be explained due to regional gusty winds caused by cloudy patterns. Also, the low wind band on the south west side of Norway is not present in the QuikSCAT satellite data. Both numerical atmospheric models are different in wind speed, spatial distribution, and coastal behavior and the average wind speed in both high-resolution atmospheric models is below the respective QuikSCAT observation.

For comparison to remote sensing data the relevant difference is that LM is a nonhydrostatic and HIRLAM a hydrostatic model with lower resolution. Nonhydrostatic models resolve more convection patterns in the boundary layer. Further higher variability in the surface wind field in the macroscale is observed.

In the following, the LM is compared to SAR retrieved wind speed. In the following two effects of SAR retrieved wind speed and model wind data are discussed. The color code in the following figures for SAR wind speed arrows is chosen to be the same as for the model. The background shows the LM model wind field. The ENVISAT ASAR wind field is superimposed showing similar spatial variations as the LM wind field (Fig. 18). However, the model is not resolving the small scale features as can be seen on the SAR measurement in Fig. 18. The region of SAR derived strong winds of up to 25 m/s aligned with convective cloud bands of 20 km by 10 km can be detected. As mentioned in Section IV model resolution is too low to detect these small scale features. As can be observed in Fig. 19, land surface effects close to the east coast of Scotland are also not well resolved in the considered models. The SAR wind field retrieval shows a coastal wind band of 25 m/s wind speed and above. Air in contact with the mountains (Highlands of Scotland) is cooling and falls down causing an increase in wind speed. In theory, the area of increased wind speed should extend out over the ocean only for a few kilometres. But the observed wind band is to long. This has to be investigated further one for high wind speeds. One possible explanation is an increase and outlook in ocean wave height, causing in additional radar backscatter.

Mesoscale features of wind speed can be seen in time series of *in situ* measurements. Fig. 20 shows the 10 min averaged wind speed time series at 33-m height measured by FiNO1. This measurement best represents the atmospheric conditions in the case of Britta between the October 31, 2006 at 00:00 UTC and the November 2, 2006 at 00:00 UTC. The satellite images were taken at 10:42 UTC. Peaks show wind speed increased due to passage of the maximum wind speed area ahead of cloud bands and afterward decreased. Measured averaged wind speed

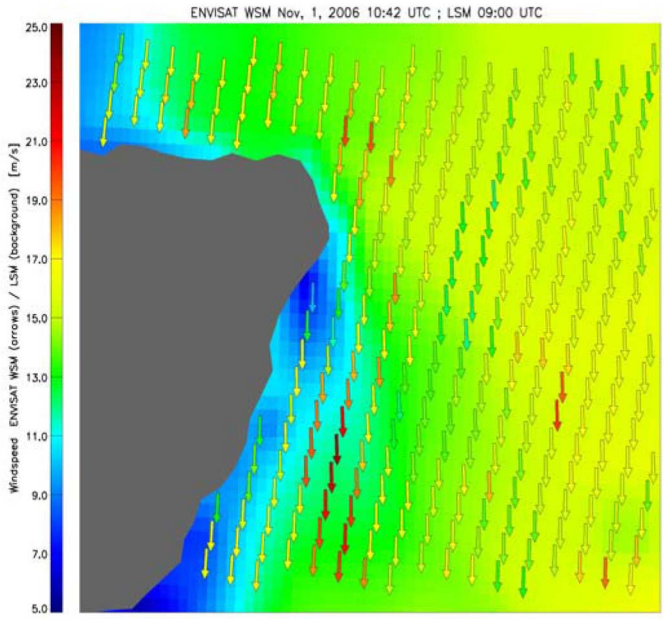

Fig. 19. Wind field LM model input (background) ENVISAT ASAR wind field is superimposed with arrows.

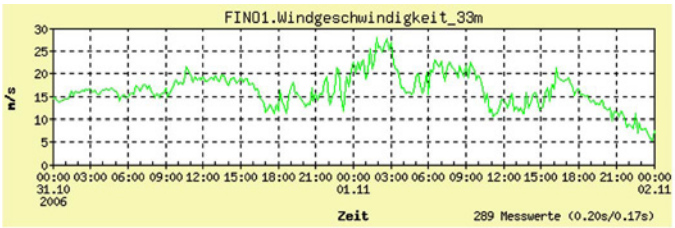

Fig. 20. Wind speed measurement FiNO1 from October 31, 2006 to November 1, 2006 at 33-m height.

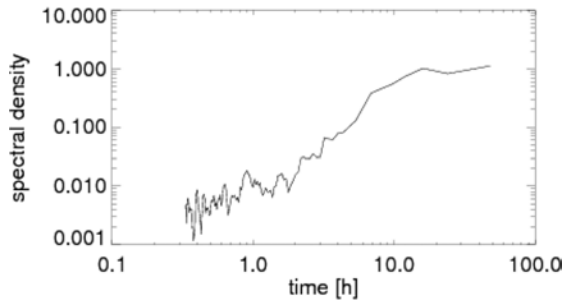

Fig. 21. Spectral density over time of the wind speed time series measured by FiNO1 between October 31, 2006 to November 1, 2006.

between 5 and 28 m/s agree quit well with measurements by the ENVISAT ASAR and the QuikSCAT sensor. The spectrum of the time series in Fig. 21 shows an expected drop of energy going to shorter time scales. From 0.1 to 1.0 h the spectrum density shows peaks. An explanation for this is the turbulent wind field. By simple use of Taylor hypothesis, it can be estimated that if the entire cloud system observed moves at an advection speed of 20 to 40 m/s spectral peaks caused by turbulent structures of the scale of 0.1 to 0.3 h should are equivalent to a spatial pattern of the wind field of 30 to 50 km which is of the right order of magnitude when compared to the cell size of cloud patterns. SAR retrieved spatial characteristic of wind field can be used to increase the confidence level of short term power forecast.

XI. Conclusion

We investigated the fine scale structure of a severe weather case on November 1, 2006 over the North Sea using satellite and model data. The wind field of Storm Britta from the HIRLAM or the German Weather Service LM is validated using the ENVISAT ASAR and QuikSCAT wind field. LM and HIRLAM show differences in mesoscale turbulent behavior and coastal shadowing. Maximum wind speed of up to 25 m/s is measured by SAR and can be observed in the model results, too. However, significant differences are observed in the location of the maxima. Due to the high-resolution ENVISAT ASAR measurements provide very detailed information on small scale atmospheric features, which seem to be not well captured by the analyzed numerical models in particular in coastal areas. Mesoscale feature, e.g., downburst due to cloud patterns with a diameter of up 15 km are not detected by neither LM nor HIRLAM.

The nonhydrostatic model LM provides more spatial details of the wind field. For the explanation of high backscatter in front of cloud bands optical cloud products, e.g., cloud optical thickness and total water path that are products of combined visible and infrared channels are used. Ahead of clouds the surface wind speed is observed to increase by 15 m/s.

Wind field derived by scatterometer are used to validate general structures on the km scale. Differences to model data are observed. LM shows too long wind shadowing at the south coast of Norway, HIRLAM shows a too smooth wind field due to the assumption of being hydrostatic. Fine scale features, e.g., due to cloud patterns or cloud cells can be detected by SAR. Coastal jets of 25 m/s caused by topography effects are detected, too. Scatterometer and SAR wind fields show more coastal, topographic, and turbulent structure.

Results give new opportunities for comparing more offshore wind farm sites and validating the results with *in situ* measurements and models of nearly the whole North Sea. In this study we showed how satellite images taken by space-borne radar sensors can be used to determine mesoscale wind fields and, thus, help in the task of planning offshore wind farms.

The joint use of high-resolution SAR, scatterometer, and optical data allow observation of high-resolution wind fields inside offshore wind farms. Small scale wind patterns can be detected and can help to understand the behavior of an offshore wind farm. Large-scale wind patterns lead to an increase in wave height. Wave height is an important factor in constructing offshore wind turbines and, therefore, to extend the life time

Short-term power forecast is one of the most important points in managing wind parks. Satellite retrieved high-resolution wind fields can help to increase the confidence level of used prediction models.

Acknowledgment

The authors would like to thank ESA for providing ENVISAT ASAR data in the framework of the AO project Wind farm, as well as the Meteorological Institute hosted at the FU-Berlin for providing COSMO/EU data, and the Swedish Meteorological and Hydrological Institute (SMHI) for providing HIRLAM data

and T. Bruns (German Weather Service, DWD) for providing LM data.

REFERENCES

[1] S. C. Pryor and R. J. Barthelmie, "Statistical analyse of flow characteristics in the coastal zone," *J. Wind Eng. Ind. Aerodyn.*, vol. 90, pp. 2001–221, 2002.

[2] R. J. Barthelmie, B. Grisogono, and S. C. Pryor, "Observations and simulations of diurnal cycles of near surface wind speeds over land and sea," *J. Geophys. Res. (Atmos.)*, vol. 101, no. (D16), pp. 21327–21337, 1996.

[3] S. C. Pryor and R. J. Barthelmie, "Comparison of potential power production at on- and offshore sites," *Wind Energy*, vol. 4, pp. 173–181, 2002.

[4] [Online]. Available: http://www.ssmi.com

[5] J. Horstmann, H. Schiller, J. S. Stellenfleth, and S. Lehner, "Global wind speed retrieval from SAR," *Trans. Geosci. Remote Sens.*, vol. 41, no. 10, pp. 2277–2286, Oct. 2003.

[6] S. Lehner, J. Horstmann, W. Koch, and W. Rosenthal, "Mesoscale wind measurements using calibrated ERS SAR images," *J. Geophys. Res.*, vol. 103, pp. 7847–7856, 1998, ISSN 0148–0227.

[7] T. Schneiderhahn, "Comparison of offshore wind park sites using SAR wind measurement techniques," *Meteorol. Appl., Band 12, Nr. 02*, pp. 101–110, 2005.

[8] Mariners Weather Log [Online]. Available: http://www.vos.noaa.gov/

[9] M. I. Mityagina, Y. A. Kravtsov, V. G. Pungin, K. D. Sabinin, and V. V. Yakovlev, "Detection of convective instability in atmospheric boundary layer over the ocean by air borne ku-band real aperture radar," presented at the Geoscience and Remote Sensing Symp. 1996.

[10] T. M. Weckwerth, J. W. Wilson, R. M. Wakimoto, and N. A. Crook, "Horizontal convective rolls: Determining the environmental conditions supporting their existence and characteristics," *Monthly Weather Rev.*, vol. 125, pp. 505–526, 1997.

[11] M. L. Weismann and J. B. Klemp, "Characteristics of isolated convective storms," in *Mesoscale Meteorol. Forecast.*, P. S. Ray, Ed. Boston, MA: Amer. Meteor. Soc, 1984, pp. 414–436.

[12] R. A. Houze, *CloudDynamics*. San Diego, CA: Academic, vol. 573.

[13] H. Hersbach and A. Stoffelen, "The improved C-band geophysical model function C-mod 5," *J. Geophys. Res.–Oceans, 2005JC002931*, 2005, submitted for publication.

[14] J. S. Stellenfleth, "On the divergence and vorticity of SAR derived wind fields," presented at the ENVISAT Symp., 2007.

[15] J. Fischer, R. Preusker, and L. Schüller, MERIS Cloud Top Pressure (CTP) ATBD.

[16] R. Preusker, L. Schüller, and J. Fischer, "Cloud top pressure retrieval from measurements within the O2-a band with the satellite imaging sensor MERIS," in *Proc. Geoscience and Remote Sensing Symp.*, 1999, pp. 143–145.

[17] [Online]. Available: http://193.204.238.60/instruments/meris/atbd/atbd_2_01.pdf

[18] COSMO/EU [Online]. Available: http://www.cosmo-model.org

[19] M. Tiedtke, "A comprehensive mass flux scheme for cumulus parameterization in large-scale models," *Meteor. Atmos. Phys.*, vol. 64, pp. 21–50, 1989.

[20] P. Mellor and T. Yamada, "A hierarchy of turbulence closure models for planetar byoundary layers," *J. Atmos. Sci.*, vol. 31, pp. 1791–1806, 1979.

[21] J. S. Kain and J. M. Fritsch, "Convective parameterisation for mesoscale models: The Kain-Fritsch scheme," in *The Representation of Cumulus Convection in Numerical Models*, K. Emanuel and D. Raymond, Eds. Boston, MA: AMS, 1993, vol. 46.

[22] D. Atlas, "Footprints of storms on the sea: A view from spaceborne synthetic aperture radar," *J. Geophys. Res.*, vol. 99, pp. 7961–7969, 1994.

[23] T. Nauss and A. A. Kokhanovsky, "Discriminating raining from non-raining clouds at mid- latitudes using multispectral satellite data," *Atmos. Chem. Phys. Discussions*, vol. 6, pp. 1385–1398, 2006.

[24] R. R. Rogers and M. K. Yau, *A Short Course in Cloud Physics*. New York: Pergamon, 1989, vol. 290.

[25] R. M. Wakimoto, "Convectively driven high wind events, severe convective storms," *Meteorol. Monogr.*, vol. 28, no. 50, pp. 255–298, 2001.

[26] M. L. Weismann and J. B. Klemp, *Characteristics of Isolated Convective Storms, Mesoscale Meteorology and Forecasting*, P. S. Ray, Ed. Boston, MA: AMS, 1984, pp. 414–436.

[27] MSG Cloud Top Pressure [Online]. Available: http://www.user-page.fu-berlin.de/~geoiss/en/home.html

Stephan Brusch received the diploma degree in meteorology from the Free University, Berlin, Germany, in 2006. He is currently pursuing the Ph.D. degree at the Remote Sensing Technology Institute (IMF), DLR.

He joined the German Aerospace Center (DLR/DFD), Oberpfaffenhofen, Germany, in 2006. In the framework of the Helmholtz Research Network "Integrated Earth Observing System" Helmholtz-EOS, he is working on SAR observation of ocean waves and wind fields.

Susanne Lehner received the M.Sc. degree in applied mathematics from Brunel University, Uxbridge, U.K., in 1979, and the Ph.D. degree in geophysics from the University of Hamburg, Hamburg, Germany, in 1984.

She was a Research Scientist with the Max-Planck Institute for Climatology, Hamburg, and joined the German Aerospace Center (DLR/DFD), Oberpfaffenhofen, Germany, in 1996. Currently, she is a Research Scientist in marine remote sensing, Remote Sensing Technology Institute (DLR/IFM), Oberpfaffenhofen, working on the development of algorithms determining marine parameters from SAR.

Johannes Schulz-Stellenfleth received the diploma degree in applied mathematics from the University of Hamburg, Hamburg, Germany, in 1996.

He joined the German Aerospace Center (DLR/DFD), Oberpfaffenhofen, Germany, in late 1996. In the framework of the Remote Sensing of Sea Ice (FEME) Project, he worked on SAR observation of ocean waves in the marginal ice zone. He is now a Research Scientist with the Remote Sensing Technology Institute (IMF), DLR. The main interest of his present work is the use of complex SAR data to derive two-dimensional ocean wave spectra. Apart from that, he is working on the application of cross-track interferometric (InSAR) data to measure sea surface elevation models.

Underwater Bottom-Topography in coastal areas from TerraSAR-X data

STEPHAN BRUSCH†, PHILIPP HELD†, SUSANNE LEHNER†, WOLFGANG ROSENTHAL‡, ANDREY PLESKACHEVSKY*†

†German Aerospace Center (DLR), 82234 Wessling, Germany
‡Gauss GmbH, Werderstrasse 73, 28199 Bremen, Germany

(Received 1 September 2009; in final form 25 January 2010)

In this paper, wave refraction and shoaling in coastal areas are investigated and used to derive the bathymetry. Due to its high spatial resolution, which can achieve up to 1m in Spotlight mode, and its low cut-off wavelength, images from the TerraSAR-X satellite are particular suitable for the observation of wave behavior in transient and shallow water. By computing the two dimensional spectra shoaling waves are tracked from the open sea up to the shoreline. The observed wave refraction and shoaling is compared with wave refraction laws and first order wave theory (Airy Theory). The retrieved bathymetry is compared against depth data from other sources like ETOPO1, US Coastal Relief Model and sea charts from the British Admiralty. Another goal of this paper is the investigation of breaking waves showing up as near shore image patterns. A theory is presented how to derive the height of breaking waves by use of this pattern. SAR images with azimuth as well as range traveling waves are investigated. As test sites the entrance of Port Phillip near Melbourne (Australia) and the Duck Research Pier in North Carolina (USA) are chosen.

1. Introduction

The shallow waters (<100m water depth) in coastal areas are one of the most important regions for human activities on the seas. A lot of fishing, offshore technology and most of the research activities are carried out in these regions. Each ship, whether it is a small sailing boat or a big cargo ship longer than 300m, has to pass shallow water areas before it can enter a harbour. For all these operations, knowledge of the water depth is one of the most important information for secure navigation.

But also the behavior of waves in coastal areas is very important for navigation, as the wave become shorter and higher when entering shallow water, which leads to an increasing of wave steepness. For sailors wave steepness is the more dangerous factor than absolute wave height. So in severe weather, with waves propagating to the coast, calling at a safe harbour can be more dangerous than staying in the open sea, depending on local bathymetry.

Due to their high resolution, daylight and weather independency and global coverage, space borne SAR's are particular suitable for many ocean and coastal applications. SAR is a unique sensor to provide scientists with two dimensional information of the ocean surface.

In June 2007, a German SAR satellite was launched, TerraSAR-X (http://www.dlr.de/TerraSAR-X). Since January 2008, data and products are available for researchers and commercial customers. TerraSAR-X operates from a 514km height sun-synchronous orbit. The repeat-cycle is 11 days, but the same region can imaged with a different incidence angles, after three days. There are three different modes with different spatial resolution, ScanSAR, StripMap, Spotlight and High-Resolution Spotlight. Technical parameters of the different modes are provided in table 1. Typical incidence angles range between 20° and 60°.

Table 1. TerraSAR-X imaging modes.

	ScanSAR	**StripMap**	**Spotlight**	**High-Resolution Spotlight**
Swath Width (ground range)	100 km	30 km	10km x 10 km	5km x 10km
Azimuth Res.	18m	3.3m	2 m	1.7 m
Range Res.	1.7m – 3.5m	1.7m – 3.5m	1.5m – 3.5m	1.5m – 3.5m

Due to its high resolution, TerraSAR-X is able to image changes of wave direction and wavelength in shallow water. Since Seasat was launched in 1978 many investigations on the imaging of ocean features by spaceborne SAR's have been performed. In 1984 Alpers and Hennings presented a first theory of imaging processes of under water bottom topography by SAR's (Alpers and Henning, 1984). The basis of this theory is the variation of a strong current by bottom topography. If a strong current flows perpendicular over a sand bank, the speed of the current is higher over the ridge than before or after, due to the law of conservation of mass. If the current becomes faster over the ridge, the wavelength of small-scale wave increases. After the ridge, when the current speed decreases the wavelength decreases, too. Due ato this wave-current interaction, variations of currents affect the small-scale Bragg waves which are responsible for the radar backscatter of the ocean. Therefore underwater bottom topography becomes visible in SAR images by modulating the image brightness, (Romeiser and Alpers 1997).

Using this model one can only compute the change of the underwater bottom topography. To get the complete bathymetry one has to input water depth from other sources, for several reference points. This model was used in many projects and is described in papers: Alpers and Hennings (1984), Hennings (1990), van der Kooij et al. (1995), Romeiser and Alpers (1997), Hesselmans et al. (2000), Huang et al. (2001) Hashim and Kadir (2002) and Fan et al. (2008). Although this approach works only for a perpendicular current, or the perpendicular component of a current, X. Li, Ch. Li and W.G. Pichel showed that sand ridges parallel to tidal currents can also be imaged by SAR (Li et al. 2006).

In this paper another possibility to retrieve bathymetry from SAR images is presented. Via an FFT a directional image spectrum is produced, from this spectrum the peak wavelength and direction are extracted. The linear dispersion-relation is used to directly calculate water depth by the measured ocean wavelength. This method has been used as well for data from the marine radar (WAMOS) (Hessner et al. 1999) and optical data (Piotrowski and Dugan 2002). To calculate water depth with the dispersion relation one has to also know the wave frequency. As WAMOS data consist of a time series, the wave frequency can be found by computing the temporal FFT. In the case of static SAR data wave frequency must be obtained from other sources or by calculating it with a first guess for the water depth. For all studies presented in this paper the latter way is used. The retrieved water depth is compared

against water depth from other sources, e.g. British Admiralty nautical chart and the US Coastal Relief Model.

The second goal of this paper is the investigation of image patterns, produced by breaking waves. Wave speed decreases and wave height increases as the wave enters shallower water. As the wave height increases the orbital velocities also increases, as long as the wave can support its own crest. If the horizontal orbital velocity becomes faster than the wave travel velocity the wave begins to break. The high velocities of scatter in the moment of wave breaking cannot be tracked by the SAR, which leads to a smearing and displacement in the SAR image (Oliver and Quegan 1998, Jackson et al. 2005). By measuring the length of the breaking streaks in the SAR image we estimate the wave height at its breaking point.

In the present study, ocean gravity waves on TerraSAR-X Spotlight images with coverage of 10km by 10km are investigated. Three test sites with azimuth and range traveling waves were chosen: the entrance of Port Phillip near Melbourne in Australia and the Duck Research Pier in North Carolina in the United States. In table 2 an overview of all TerraSAR-X images used is presented.

Table 2. TerraSAR-X data used for this investigation.

	Date	**Time (UTC)**	**Location**
TSX1_SAR__MGD_SE___SL_S_SRA_20080317T194534_20080317T194536	2008-03-17	19:45:36	Port Phillip (Australia)
TSX1_SAR__MGD_SE___SL_S_SRA_20080320T225013_20080320T225014	2008-03-20	22:50:14	Duck Research Pier (USA)

In figure 1 a TerraSAR-X image, acquired in Spotlight mode on March 17, 2008 over Port Phillip is shown on a Google Earth map. The ocean waves are clearly visible in the image. Coming from the Southwest the long ocean swell is refracted by the changing bottom topography until the wave crests have become parallel to the shoreline. Wave diffraction can be observed in and after the entrance to Port Phillip. Wave convergence due to underwater ridges can be seen in the lower right part of the radar image. Even changing of the wavelength due to energy dissipation by bottom effects is clearly visible. Near to the coast line smearing occurs due to motion effects of the breaking waves.

The paper is organized as follows: in section 2 the imaging of ocean waves is explained briefly. In section 3 the auxiliary datasets used in this paper are presented. The theory of wave refraction and shoaling as well as a short comparison of theory against measurement is summarized in section 4. The retrieving of ocean wave parameters and the algorithm to track wave in SAR images is briefly described in section 5. In section 6 the retrieved bottom topography is given for all two test sites. The retrieved bathymetry will be compared against depth data from other data sets, described in section 3. Section 7 deals with the investigation of breaking patterns in SAR images. Conclusions and discussion are given in the last section.

Over a water surface, the backscatter depends on surface roughness due to short surface waves, which wavelength is similar to that of the radar signal. These small capillary waves are called Bragg-waves if they satisfy the following Bragg condition (Hasselmann et al. 1985):

$$\lambda_B = \lambda_r / 2\sin\theta_i , \qquad \textbf{(1)}$$

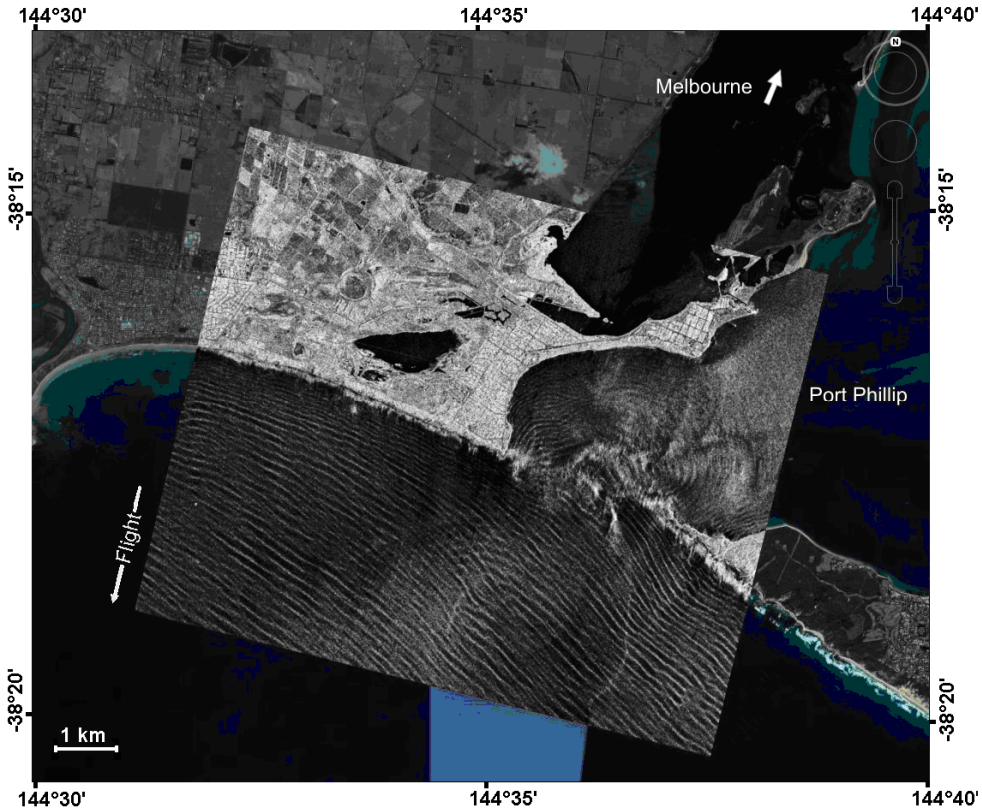

Figure 1. TerraSAR-X Spotlight acquired on March 17, 2008 over the entrance of Port Phillip (background image © Google Earth).

where λ_B is Bragg-water-wavelength, λ_r is the radar wavelength and θ_i is the local incidence angle. If capillary waves satisfy the Bragg condition, constructive interference in the direction of the sensor occurs. This Bragg scattering is the dominant backscatter mechanism for incidence angles between 20° and 60° (Lehner et al. 1998, Horstmann et al. 1998). Due to uniformly distribution of the small-scale waves the Bragg condition is nearly always satisfied (Jackson et al. 2005).

The short Bragg waves are modulated by the long ocean gravity waves. Therefore a two-scale model (Hasselmann et al. 1985) is used to describe the imaging process of long ocean waves by SAR. The two-scale model consists of two modulation mechanisms, tilt modulation and hydrodynamic modulation. Tilt modulation means that the slope of gravity waves changes the local incidence angle θ_i and therefore the Bragg wavelength and the intensity of backscatter. Hydrodynamic modulation is caused by the orbital movement of water particles within the gravity wave. This leads to a convergence of capillary wave on the crests and a divergence of capillary waves in the troughs of ocean gravity waves. Therefore the crests of long waves appear brighter in the SAR image (Jackson et al. 2005).

Wave crests are propagating objects, they move during the image acquisition. This movement will cause some image artifacts. This effect is particularly strong for waves that travel in the direction of azimuth. This culminates in the fact, that azimuth traveling waves which are shorter than a certain threshold is not imaged by the SAR. This threshold is the so called SAR azimuth cut-off wavelength. Between several approaches to estimate the cut-off wavelength, there is a relative simple empirical relationship for the observed cut-off wavelength is given by (Beal et al. 1983):

$$\Lambda_{\min} = \frac{R_o}{V_{SAR}} \sqrt{H_S} \,. \qquad \textbf{(2)}$$

In this formula R_o is the slant range, V_{SAR} is the platform velocity, H_S is the significant wave height and Λ_{min} is the azimuth cut-off wavelength. The SAR azimuth cut-off wavelength depends on orbit parameter of the satellite as well as on the sea state at acquisition time. Due to its low orbit compared to ERS1/2 and ENVISAT, TerraSAR-X should have a quite short azimuth cut-off wavelength of around 100m according to theory for a sea state of 2.0m significant wave height. TerraSAR-X is therefore able to detect short shoaling waves which propagate in azimuth direction. The shortest near shore waves observed in figure 1 have a wavelength of 70m.

3. Description of auxiliary data

In this paper three different data sets of depth information are used. For the Port Phillip case an official nautical chart from British Admiralty is used, number of the sea chart is BA AUS 144. In the case study of Duck Pier the high resolution US Coastal Relief Model is used. It provides depth information of the US coastal zone with a 3-arc-second resolution (http://www.ngdc.noaa.gov/mgg/coastal/coastal.html). For comparison of wavelength derived from 2D-spectra, the Global Sea wave Model GSM of the German Weather Service (DWD) is used. GSM is based on a spatial resolution of 0.75° by 0.75° and produces forecast at 3 hour steps.

4. Wave shoaling and refraction

The refraction of long swell at water depth smaller than 50m is caused by influence of the underwater topography in coastal areas. We apply the linear wave theory to describe wave behavior in intermediate and shallow water. Ocean surface waves begin to feel bottom if the water depths becomes lower than about half of the wavelength. If long ocean swell is propagating into shallow water it will be decelerated. This causes the wavelength to shorten. The wave height increases due to conservation of energy. These two facts increase the wave steepness. Deceleration together with the increasing wave height and steepness is called wave shoaling.

If wave crests are not aligned with contour lines of bottom topography, under a certain angle between wave direction and contour line, wave refraction occurs. The part of a wave which is closer to the beach, e.g. travels in shallower water is decelerated stronger than the part of the wave further outside. Parts of the wave in shallower water are overtaken by those in deeper water. This results in a changing of wave travel direction and takes place until the wave crests have become parallel to the shoreline or the wave breaks. This effect is the same as in geometrical optics, when an electromagnetic wave propagates from one medium into another with a different speed of light. Therefore Snell's law for optics is used for a mathematical description of wave refraction in intermediate and shallow water (Kinsman 1984, Mei 2005):

$$\frac{\sin\varphi_1}{\sin\varphi_2} = \frac{\lambda_1}{\lambda_2} \qquad \text{Snell's law} \qquad \textbf{(3)}$$

where φ_1 and φ_2 are angles between wave propagation direction and local bottom topography contour for locations *1* and *2* (means changing of wave propagation direction) and λ_1 and λ_2 are the wavelength for these correspondingly. As water waves are not pure transversal waves the path of a water particle within a wave describes an orbit. To first order the orbits of a water particle are closed curves. The celerity and direction of a water particle depends on wave height, water depth as well as on the local wave phase. If the speed of wave propagation in shallow water becomes lower than the speed of water particles on the wave crest, wave breaking occurs.

The wave height H while shoaling can by calculated by the following formula from (Kinsman 1984),

$$H = H_d D_S K_R . \quad \textbf{(4)}$$

Here H_d is the deep water wave height, D_S is called shoaling coefficient and K_R is the refraction coefficient.

$$D_S = \left(\frac{k}{k_d}\right)^{\frac{1}{2}} \left(1 + \frac{2kd}{\sinh(2kd)}\right)^{-\frac{1}{2}}, \quad \textbf{(5)}$$

$$K_R = \left(\frac{\cos(\alpha_d)}{\cos(\alpha)}\right)^{\frac{1}{2}} \quad \textbf{(6)}$$

where α_d and α are angles between wave crest and coastal line before and after refraction respectively, $k=2\pi/\lambda$ is the wave number, d is the water depth. Wave breaking occurs if the steepness of a wave overtakes a certain threshold, e.g. if the following relation is satisfied

$$\frac{H}{\lambda} \geq 0.142 \tanh\left(\frac{2\pi}{\lambda} d\right). \quad \textbf{(7)}$$

This corresponds to a wave crest angle of 120° (Stewart 2008). The formulas discussed in this section are used for a wave simulation discussed in the following.

5. Tracking of shoaling waves on SAR and computation of underwater bottom topography

By computing the Fast Fourier Transformation (FFT) for a sub-image a 2 dimensional image spectrum is retrieved. The peak in the 2D spectrum marks mean wavelength and mean wave direction of all waves visible in the sub-image. Values for wavelength and angle of propagation can be retrieved by the following formulas:

$$L = \frac{2\pi}{\sqrt{k_x^2 + k_y^2}}, \quad \textbf{(8)}$$

$$\varphi = \arctan\left(\frac{k_y}{k_x}\right) \quad \textbf{(9)}$$

where L is the peak wavelength and φ is the peak wave direction with respect to the image. k_x and k_y are the peak coordinates in the frequency space. The retrieved wave directions have an ambiguity of 180° due to the static nature of a SAR image. Normally this ambiguity problem must be solved with information about wave direction from the cross spectrum or other sources. In coastal areas where wave shoaling and refraction appears the ambiguity problem can be solved by looking into the picture.

Starting in open sea the box for the FFT is moved in wave direction by one wavelength and a new FFT is computed. This procedure is repeated until the corner points of FFT-Box reaches shoreline. This way a wave can be tracked from open sea to shoreline and changing of wavelength and direction can be measured. Figure 2 shows tracked rays compared against simulated wave rays. The simulated wave is computed by using linear wave theory for a depth field retrieved from the sea chart for the entrance of Port Phillip. The measured wave rays are tracked on a SAR image acquired on March 17th, 2008 at 19:45UTC over the entrance of Port Phillip. The wave rays agree quite well with each other in this case, this indicating that the first order Airy Theory is a good approximation to describe wave refraction.

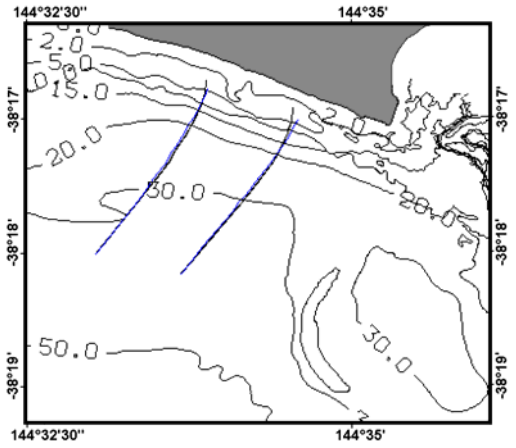

Figure 2. Simulated wave rays (black) compared to SAR measured wave rays (blue).

To retrieve water depth from SAR images, the linear dispersion relation for ocean gravity waves is used. Solved with respect to water depth d the dispersion relation reads:

$$d(L,\omega) = \frac{L}{2\pi}\operatorname{atanh}\left(\frac{\omega^2 L}{2\pi g}\right), \qquad \textbf{(10)}$$

where g is the acceleration of gravity, $\omega=2\pi f$ is the angular wave frequency: here the obtained water depth also is a function of wave frequency $f=1/T$. As a SAR image has no temporal information on the sea state, wave frequency can be retrieved from other sources, as by buoy or the weather services.

In this paper another method is used: The first measured wavelength of a wave ray together with a first guess for water depth from a topography dataset is used to calculate wave frequency. In figure 3 the dependence of the retrieved water depth on wavelength for different first guesses for water depth d_0 is shown. First the wave period is obtained from different d_0 (30; 32; 34; 36; 38; 40m) using eq.10, and later it is applied to obtain the bottom topography for different wave length. E.g. the typical swell wavelength about 160m (red vertical bar on the figure 3) present the difference of obtained water depth d about 2.8m, if spread of 10m of first guess depth d_0 is used (obtained depth d=11m for d_0=30m and d=13,8m for d_0=40m). After computation of water depth for every estimated wavelength, all retrieved depth data are interpolated in order to get a map of the bathymetry.

In this section the results for retrieved underwater bottom topography for the two test sites will be presented. First the calibrated image acquired on March 20, 2008 at 22:50 UTC over Duck Research Pier in North Carolina in the United States is analyzed. The SAR image, the sigma naught grayscale-bar for calibration as well as 2D-spectra are shown in figure 4. As visible in the image, ocean swell is traveling in range direction towards the shore. From the image spectra an averaged peak wavelength of around 163m is derived. A wavelength of 140m swell was forecasted by the German Weather Service (DWD) for 21 UTC. A wind of 7.5m/s was blowing offshore. Due to the short fetch in the scene, wavelength of windsea is too short to be imaged by SAR. A wind sea of 30m in the open sea was forecasted by the model. The DWD-model data for significant wave height and wave direction of swell and wind sea are shown in figure 5a and 5b respectively. Position of Duck Research Pier is marked by red circle in both figures.

There is a deviation of around 20m between the measured wavelength and the forecasted by the DWD, which is probably due to lower temporal and spatial resolution of the wave model. Anyway the GSM model is still useful for FFT boundary conditions.

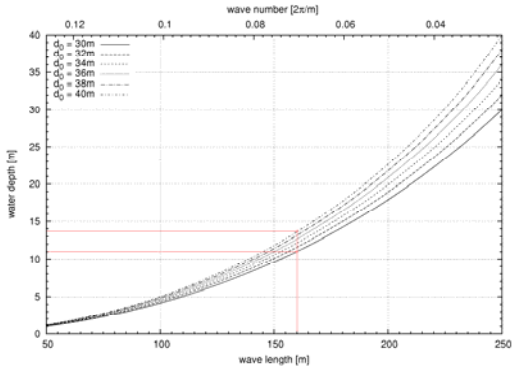

Figure 3. Dependence of retrieved water depth for different first guesses of water depth d_0 at the start point of a wave ray.

6. Case studies

The SAR image together with color-coded wave rays is shown in figure 6. The arrow direction corresponds to wave travel direction. The arrow length as well as the color coding corresponds to wavelength. As apparent in the image, wavelength is decreasing as the wave is propagating to the coast, represented by blue arrows near the shore line. Linear dispersion relation, discussed in section 4 and 5, is used to calculate water depth for each measured wavelength. In this case study 397 depth data were used to interpolate a depth field. The retrieved bathymetry together with contours from US Coastal Relief Model, are shown in figure 7. Inferred bathymetry from SAR data is in good agreement with the US Coastal Relief Model. Local variations in depth are reproduced well.

In the next case study, waves traveling in azimuth direction are investigated. The calibrated TerraSAR-X Spotlight image was acquired over the entrance of Port Phillip on March 17th, 2008 at 19:45 UTC. Here long ocean swell from the south Pacific is traveling in azimuth direction. In figure 8 the SAR image together with 2D image spectra are shown. From three spectra in the lower part of the image an average wavelength of 158m is found. Swell coming from the South West with a wavelength of 175m was forecasted by the German Weather Service for 18 UTC. Again there is a deviation of around 20m, in this case wavelength was overestimated by the model. This is probably because wave shoaling is not sufficiently taken into account due to low spatial resolution near coastal zones. But DWD model gives, however, an offshore first guess for wavelength and wave frequencies.

The DWD model forecasts for ocean swell and windsea are shown in figure 9a and 9b respectively. A short windsea of 20m wavelength was produced by an offshore blowing wind of 6.5m/s (buoy measurement, location see figure 13).

Figure 10 presents tracked wave rays for the acquisition shown on figure 8. The wavelengths are marked with color coded arrows. 38 wave rays are tracked. Every arrow in the track means one FFT box, the distance between two boxes means wavelength. The observed wavelength at track start points is between 100 and 180m, mean value is about 130m. The changing of the wavelength due to bottom influence is clearly visible,e.g. wave shoaling effects near to the beach (blue arrows give shorter wavelength of about 100m). Also wave refraction is clearly imaged by SAR. In the lower left part of the image, incoming ocean swell is refracted by bottom topography until the rays are perpendicular to the shoreline. In the lower right part, wave convergence due to an underwater shoal occurs clearly as the wave rays converge to one point.

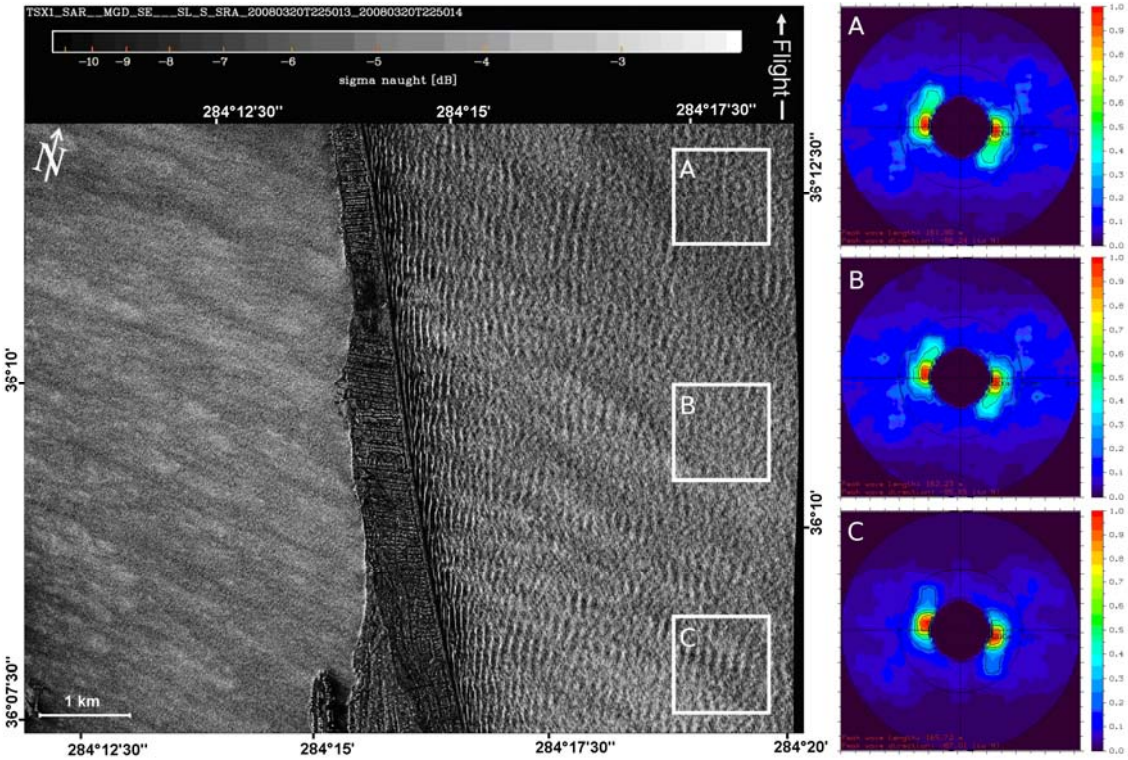

Figure 4. TerraSAR-X Spotlight acquired over Duck Research Pier, NC, USA on Mar. 20th, 2008 at 22:50 UTC. Three subscenes marked as A, B and C are used for spectral analysis.

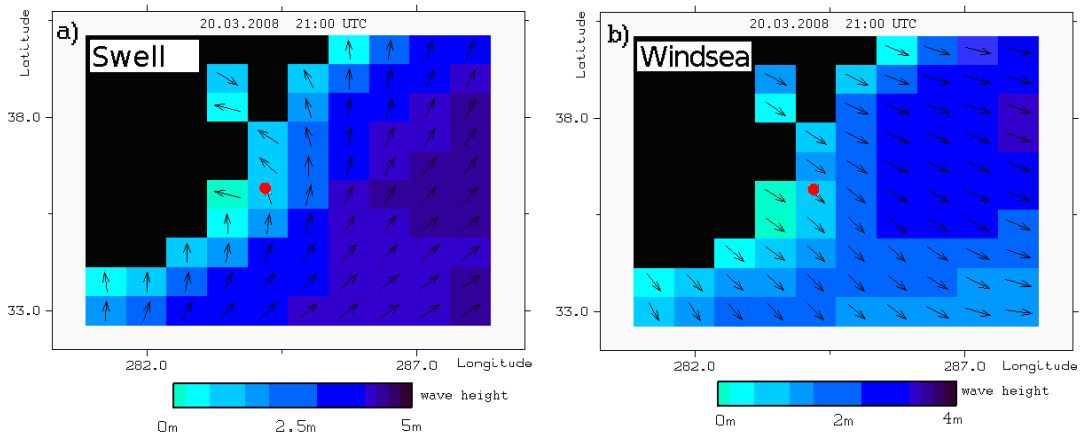

Figure 5. DWD forecast of swell (a) and of windsea (b) for March 20th, 2008 at 21:00 UTC. The Location of Duck Research Pier is shown by red point.

As seen in figure 11 SAR retrieved bottom topography fits well to depth information from an official nautical chart. The scatter plot is given on the sub-image on figure 11. This comparison is presented to shown the general agreement of SAR obtained depths dSAR against the map dMAP (entries=1880, deviation (dSAR-dMAP)<5m for 72,2% of entries, and <7m for 89,2% of entries). The SAR information is more detailed spatially and includes more local depth variability then the nautical map from 1994, therefore the statistical analysis cannot be directly used to compare these different information sets. The bathymetry behavior close to the shore is well captured.

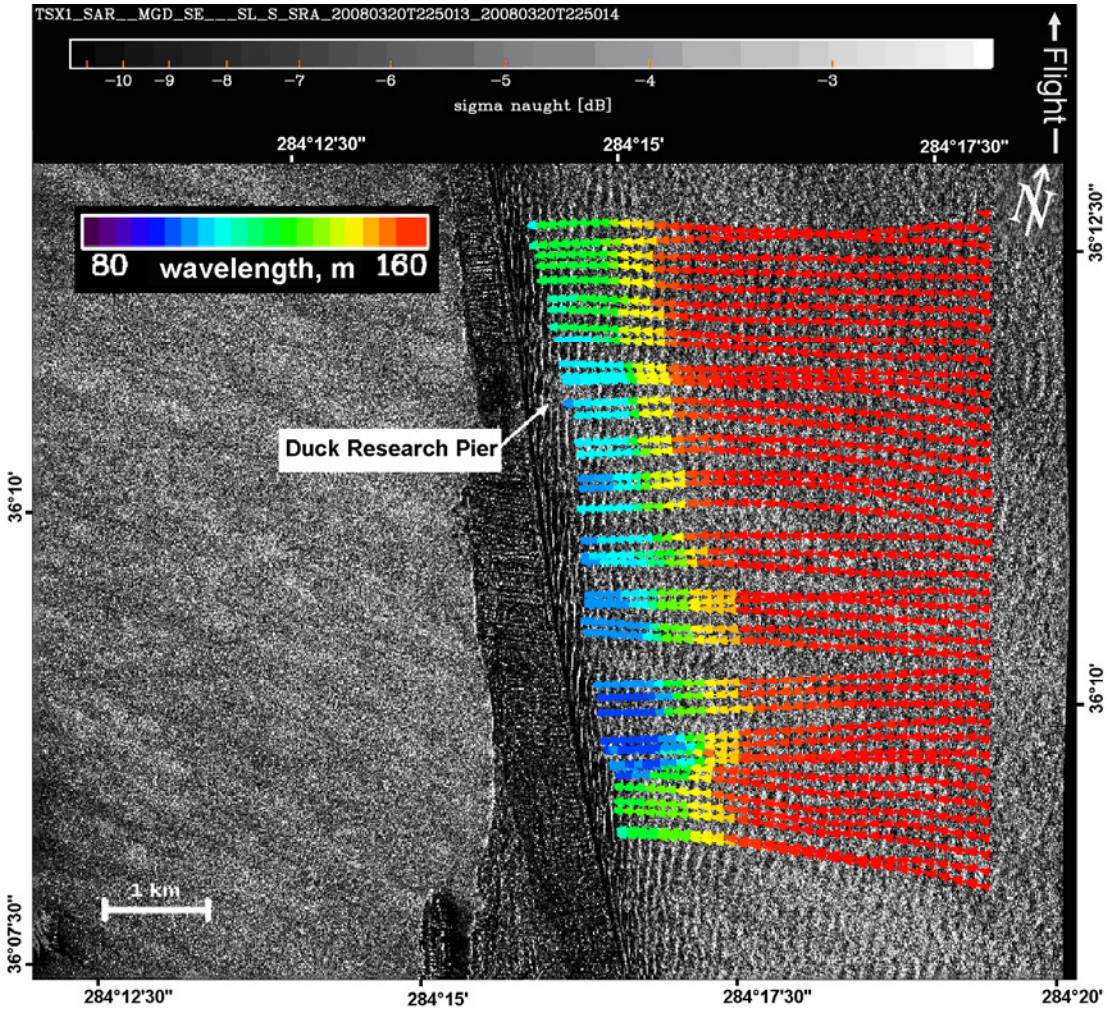

Figure 6. TerraSAR-X spotlight acquired on March 20th, 2008 at 22:50 UTC. Tracked wave rays represented by color-coded arrows.

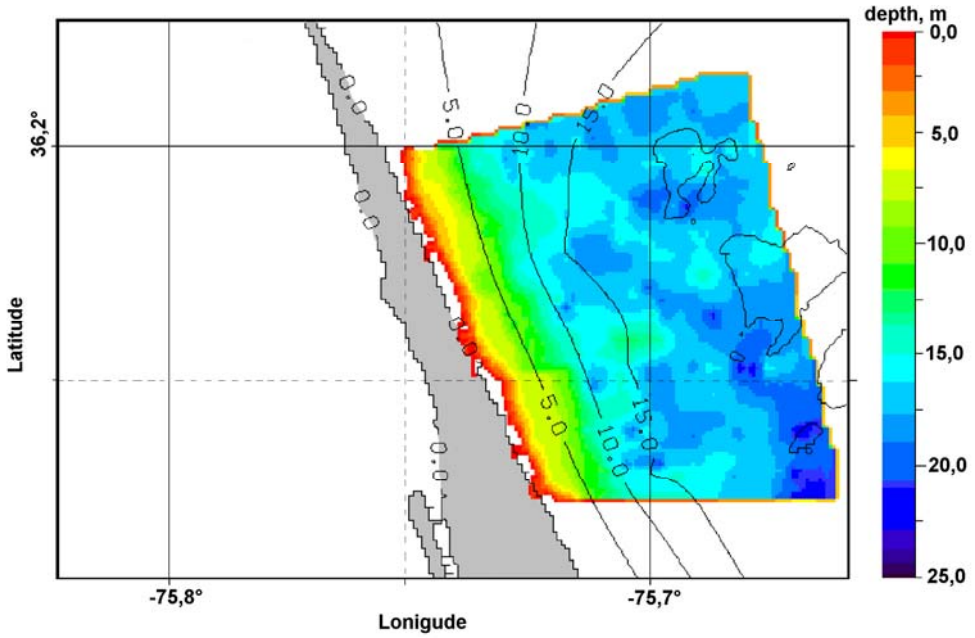

Figure 7. SAR retrieved bathymetry compared against 3" US Coastal Relief Model.

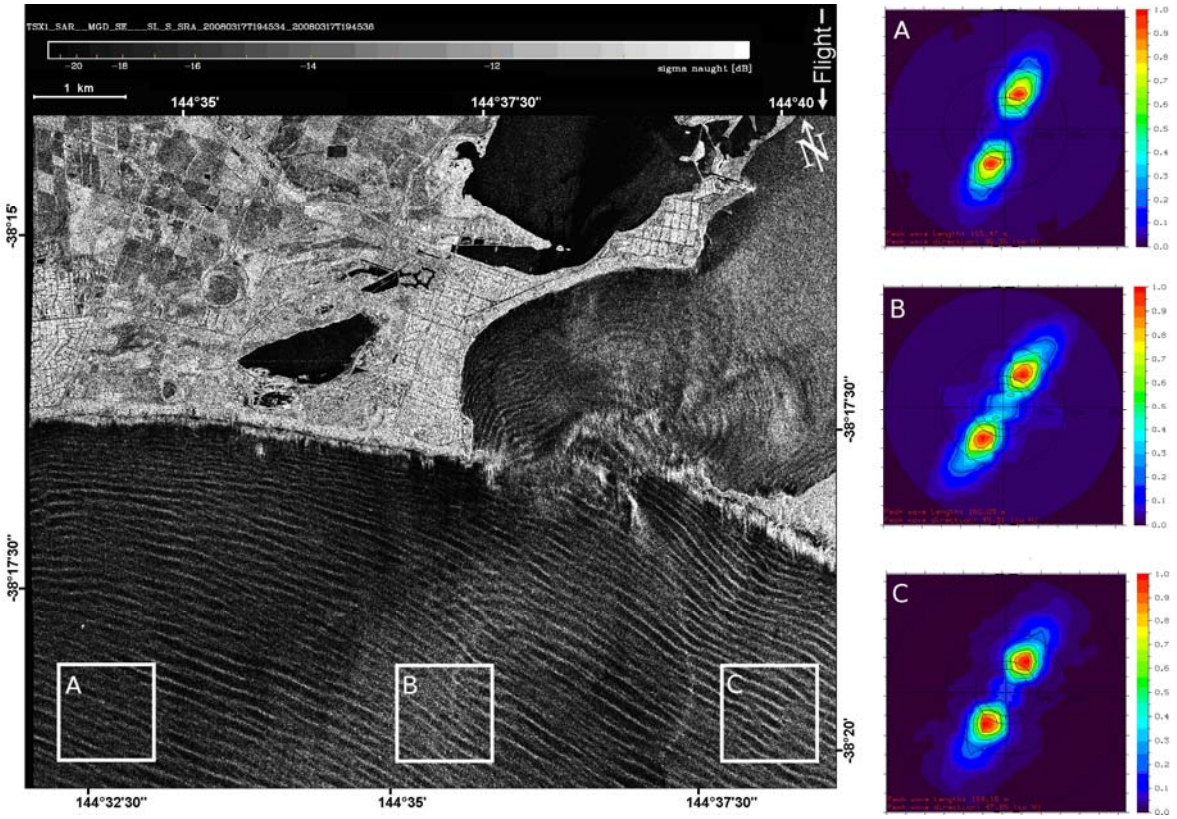

Figure 8. TerraSAR-X Spotlight acquired over the entrance of Port Phillip in Australia on Mar. 17th, 2008 at 19:45 UTC. Three subscenes marked as A, B and C are used for spectral analysis.

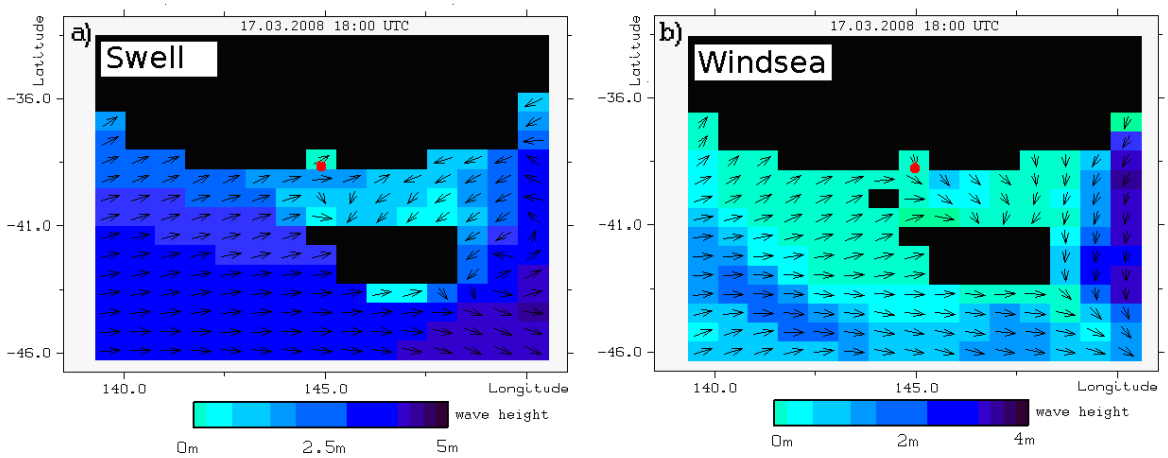

Figure 9. DWD forecast of swell (a) and of windsea (b) for March 17th, 2008 at 18:00 UTC. The Location of Port Phillip is shown by red point.

The area of shallow water on the east side of the entrance is reproduced well. Position and behavior of the water zone of more than 30m depth are also derived from SAR data, as well as a shoal of 20m and lower between these two 30m isolines. Even the position of a zone of 50m and more water depth in the center of the port entrance is reproduced by the retrieval method described in section 5. Bathymetry as retrieved from the TerraSAR-X Spotlight image shows in this case study a more detailed structure than the official nautical chart from the British Admiralty, which is maybe due to a high smoothing of contours in the nautical chart.

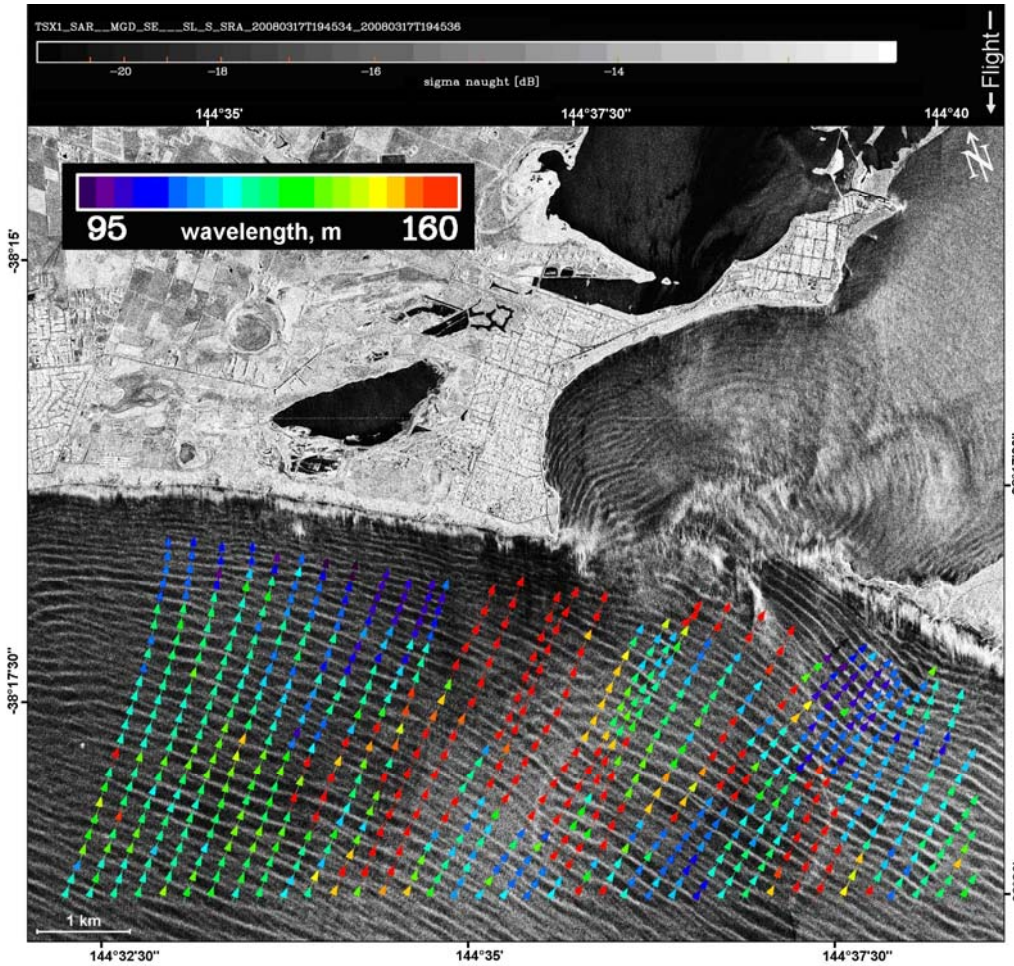

Figure 10. TerraSAR-X Spotlight image acquired over entrance of Port Phillip on Mar. 17th, 2008 at 19:45 UTC. Tracked waves rays are represent by color coded arrows.

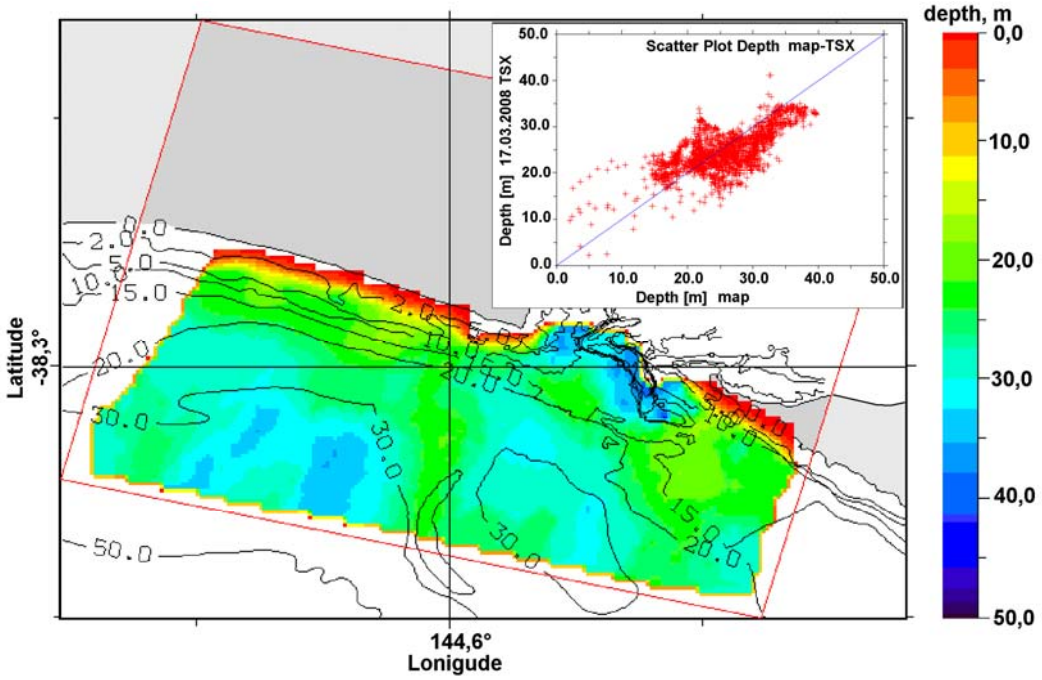

Figure 11. SAR retrieved underwater bottom topography compared against depth isolines from nautical chart.

7. Analysis of image patterns produced by breaking waves

As a wave is shoaling, wave height increases, which leads to an increasing of the orbital velocity of water particles within the wave. If the velocities of water particles become too high, they cannot be tracked by SAR any longer and smearing in the SAR images occurs. The smearing is caused by scatterers with different velocities. Each scatterer is displaced by a certain distance in azimuth direction which can be estimated by the following formula:

$$U = \left(\frac{V_{SAR}}{R_0} \right) \cdot D \,. \qquad \textbf{(11)}$$

In this formula U is the speed of object towards the sensor, V_{SAR}=7km/s is the platform velocity, R_0=514km is the slant range and D is the displacement visible on the image. The highest displacement is thus produced by the fastest scatterer. As wave height has its maximum at the breaking point, smearing is visible around the breaking point of a wave in the SAR image. A water particle within a wave reaches its maximum speed at a wave crest. At time of wave breaking, the horizontal orbital speed at wave crest becomes larger than the phase speed of the wave. The wave is overtaken by its own wave crest and the wave breaks. The maximal horizontal orbital velocity u_x^{orb} based on the linear theory is (e.g., Svendsen and Jonsson 1982):

$$u_x^{orb} = \frac{\pi H}{T} \cdot \frac{\cosh\left(k\left(z+d\right)\right)}{\sinh\left(kd\right)} \qquad \textbf{(12)}$$

where z means the vertical coordinate (z=0 at the surface, positive direction is upwards), T is the wave period. At wave crest the vertical coordinate $z=z_0=0.5H$. By measuring the length of smearing D the maximum velocity of scatterers U can be derived. Assuming latter is produced by water particles breaking away from the wave crest and their speed is the maximal orbital wave velocity $u_x^{orb}=U$, the corresponding height of breaking waves H_{br} can be estimated using eq.12.

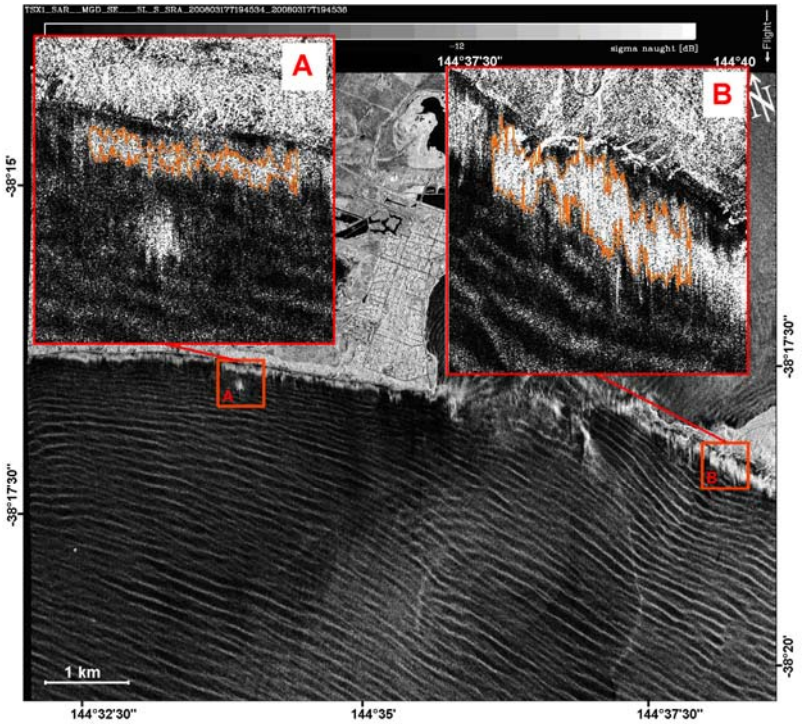

Figure 12. Output of breaking streaks detection algorithm for TerraSAR-X Spotlight image acquired on March 17th, 2008 over entrance of Port Phillip.

In figure 12 detected breaking patterns in TerraSAR-X Spotlight image acquired on March 17th, 2008 over the entrance of Port Phillip are shown. In subimage *A* an area westwards and in subimage *B*, an area eastwards of the Port-Phillip entrance are shown. The mean length of smearing is 60m in A and 180m in *B*. From the measured length of breaking patterns in subimage *A* and B of figure 12 the height of breaking waves is calculated to be 2.19m and 2.72m, respectively.

Figure 13 presents the position and measurements from the buoy, located near the entrance of the bight (38°21.6'S and 144°41.6'E) which is controlled by the Port of Melbourne Corporation. The time series shows the maximal wave height on March 17. 2008 and the TSX acquisition time (17.03.2008 17:45 UTC) is presented by the red vertical bar. The measured maximum wave height is 2.5m at the time of SAR image acquisition. The comparison of H_{br} derived from SAR H_{br}^{SAR}= 2.72m against buoy measurements shows good agreement with a difference about 20cm.

Wave height and wave frequency from buoy data and wavelength from SAR data are used to simulate wave shoaling behavior and breaking point for both cases. From this simulation we get for the height of breaking waves 3.01m and 3.07m for case *A* and *B* respectively (the results are presented in the Table 3). In cases *A* and *B* we get a difference of 0.82 and 0.35m between simulated breaking wave height and height derived from breaking pattern respectively, which is a good agreement for this comparison.

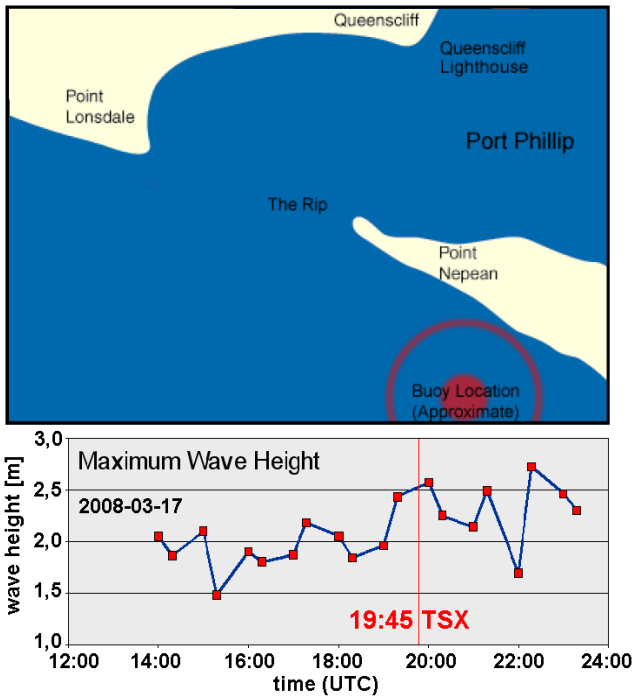

Figure 13. Maximum wave height measured by wave buoy on March 17th, 2008.

Table 3. Derivation of height of the breaking wave.

sub-image	mean length of smearing *D*, m	derived velocity *U*, m/s	mean wavelength, m	mean water depth *d*, m	breaking wave height H_{br} SAR/simulated (difference), m
A	80	1,09	60	8	2.19 / 3.01 (0.82)
B	190	2,59	180	10	2.72 / 3.07 (0.35)

8. Conclusions

In this paper calibrated SAR Spotlight images from the German TerraSAR-X Satellite are investigated. First it is presented that TerraSAR-X is capable to detect wave refraction and wave shoaling due to its high spatial resolution. A method to track shoaling waves on their way from the open ocean to the beach is demonstrated. By tracking the wave, the changing of their wavelength can be measured. The linear dispersion relation for ocean surface gravity waves is used to derive water depth from the measured wavelength.

Two calibrated SAR Spotlight images, acquired over two different test sites with different sea states are chosen for investigations. One was acquired on March 17th, 2008 over the entrance of Port Phillip in Australia and the other one on March 20th, 2008 over the Duck Research Pier in North Carolina in the United States.

In the case of Port Phillip, waves traveling in azimuth direction were investigated. In the other scene of Duck Research Pier, waves traveling in range direction were investigated. It has been found, that azimuth traveling waves down to 70m and around 2m sea state can still be captured by the TerraSAR-X satellite.

A new theory was presented to derive the height of breaking waves from image patterns, produced by breaking waves. The retrieved wave height is compared to wave height calculated with wave shoaling theories and shows a good agreement.

Acknowledgements

We would like to thank Thomas Bruns from the German Weather Service for providing us with GSM model data and Paul Downie from the Port of Melbourne Corporation for the buoy data. TerraSAR-X data were provided by DLR in the frame of sciences AO TSX Ocean Power RES-0072.

References

ALPERS, W. AND HENNINGS, I., 1984, A theory of the imaging mechanism of underwater bottom topography by real and synthetic aperture radar. *Journal of Geophysical Research,***89**, pp. 10 529-10 546.

AMANTE, C. AND EAKINS, B.W., 2008, ETOPO1 1 arc-minute global relief model: procedures, data sources and analysis. National Geophysical Data Center, NESDIS, NOAA, U.S. Department of Commerce, Boulder, CO

BEAL, R.C., TILLEY, D.G. AND MONALDO, F.M., 1983, Large- and small-scale spatial evolution of digitally processed ocean surface wave spectra from the Seasat synthetic aperture radar. *Journal of Geophysical Research*, **88**, pp. 1761-1778.

FAN, K., HUANG, W., HE, M. and FU, B., 2008, Simulation study on optimal conditions for shallow water bathymetry observation by SAR. In IGARRS, 7-11 July, Massachusetts, USA.

HASHIM, M. AND KADIR, W.H.W., 2002, SAR data analysis for wave spectrum, bathymetric and coastal information. In Second National Microwave Seminar, 1 April 2002, Mentakab, Pahang, Malaysia.

HASSELMANN, K., RANEY, R.K., PLANT, W.J. AND ET. AL., 1985, Theory of synthetic aperture radar ocean imaging: A marsen view. *Journal of Geophysical Research*, **90**, pp. 4659-4686.

HENNINGS, I., 1990, Radar imaging of submarine sand waves in tidal channels, *Journal of Geophysical Research*, **95**, pp. 9713-9721.

HESSELMANS, G.H.F.M., WENSINK, G.J. AND VAN KOPPEN, C.G., 2000, Bathymetry assessment demonstration off the Belgian coast – BABEL. *The Hydographic Journal*, **96**, p. 3.

HESSNER, K., REICHERT, K. AND ROSENTHAL, W., 1999, Mapping of sea bottom topography in shallow water by using a nautical radar. In 2nd International Symposium on operationalization of remote sensing, 16-20 August 1999, Enschede, The Nederlands.

HORSTMANN, J., KOCH, W., LEHNER, S. AND ROSENTHAL, W., 1998, Ocean wind fields and their variability derived from SAR. In *Earth Observation Quarterly*, pp. 8-12.

HUANG, W.G., FU, B., ZHOU, C.B., YANG, J.S., SHI, A.Q. AND LI, D.L., 2001, Shallow water bathymetric surveys by spaceborne aperture radar. *IEEE Geoscience and Remote Sensing Symposium*, **6**, pp. 2810-2812.

JACKSON, CH., KOCH, W. AND ET AL, 2005, Synthetic aperture radar marine user's manual. Available online at: www.sarusersmanual.com (accessed 20 March 2009).

KINSMAN, B., 1984, *Wind waves, Their generation and propagation on the ocean surface* (New York: Dover Publications, Inc.).

KOOIJ, VAN DER, M.W.A., VOGELZANG, A. AND CALKOEN, C.J., 1995, A simple analytical model for brightness modulations caused by submarine sand waves in radar imagery. *Journal of Geophysical Research*, **100**, pp. 7069-7082.

LEHNER, S., HORSTMANN, J., KOCH, W. AND ROSENTHAL, W., 1998, Mesoscale wind measurements using recalibrated ERS SAR images. *Journal of Geophysical Research*, **103**, pp. 7847-7856.

LI, X., LI, CH. AND PICHEL, W.G., 2006, SAR imaging of shallow water sand ridges aligned with tidal current. In OceanSAR, 23-25 October 2006, St. John's, NL, Canada.

MEI, CH.C., STIASSNIE, M. AND YUE, D.K.-P., 2005, *Theory and applications of ocean surface waves, Part 1: Linear aspects*, (London: World Scientific).

OLIVER, CH. AND QUEGAN, SH., 1998, *Understanding synthetic aperture radar images*, (Boston/London: Artech House).

PIOTROWSKI, C.C. AND DUGAN, J.P., 2002, Accuracy of bathymetry and current retrievals from airborne optical time-series imaging of shoaling waves. *IEEE Transaction on Geoscience and Remote Sensing*, **40**, pp. 2606-2618.

ROMEISER, R. AND ALPERS, W., 1997, An improved composite surface model for the radar backscattering cross section of the ocean surface 2. model response to surface roughness variations and the radar imaging of underwater bottom topography. *Journal of Geophysical Research*, **102**, pp. 25 251-25 267.

STEWART, R., 2008, Introduction to physical oceanography. Available online at: http://oceanworld.tamu.edu/home/course_book.htm (accessed 01 March 2009).

SWEDSEN, A. AND JONSSON, I.G, 1982, Hydrodynamic of coastal regions. ISBN 87-87245-57-4. Stougaard Jensen/Kobenhavn.

Ship Surveillance With TerraSAR-X

Stephan Brusch, Susanne Lehner, Thomas Fritz, Matteo Soccorsi, *Member, IEEE*, Alexander Soloviev, and Bart van Schie

***Abstract*—Ship detection is an important application of global monitoring of environment and security. In order to overcome the limitations by other systems, surveillance with satellite synthetic aperture radar (SAR) is used because of its possibility to provide ship detection at high resolution over wide swaths and in all weather conditions. A new X-band radar onboard the TerraSAR-X (TS-X) satellite gives access to spatial resolution as fine as 1 m. In this paper, first results on the combined use of TS-X ship detection, automatic identification system (AIS), and satellite AIS (SatAIS) is presented. The AIS system is an effective terrestrial method for tracking vessels in real time typically up to 40 km off the coast. SatAIS, as a space-based system, allows almost global coverage for monitoring of ships since not all ships operate their AIS and smaller ships are not equipped with AIS. The system is considered to be of cooperative nature. In this paper, the quality of TS-X images with respect to ship detection is evaluated, and a first assessment of its performance for ship detection is given. The velocity of a moving ship is estimated using complex TS-X data. As test cases, images were acquired over the North Sea, Baltic Sea, Atlantic Ocean, and Pacific Ocean in Stripmap mode with a resolution of 3 m at a coverage of 30 km × 100 km. Simultaneous information on ship positions was available from TS-X and terrestrial as well as SatAIS. First results on the simultaneous superposition of SatAIS and high-resolution radar images are presented.**

***Index Terms*—Radar detection, sea state, ship detection, synthetic aperture radar, wind.**

I. Introduction

DURING the past years, request for maritime surveillance with new high-resolution sensors has increased, particularly in the field of maritime security and maritime safety. Coastal-based surveillance systems are widely used but are limited in their coverage, e.g., coastal automatic identification system (AIS) only covers up to 40 km off the coast and requires ships that have AIS onboard and that operate it correctly. Satellite imagery gives the possibility to overcome these limits. The possibility to provide ship surveillance over wide regions and all weather conditions makes synthetic aperture radar (SAR) a very well suited instrument for this purpose. Different satellite images at a variety of modes are available and can be selected depending on the extent of the area in order to monitor the size of targets of interest. This has been highlighted by campaigns to detect vessels using satellite SAR imagery from RADARSAT-1 and ENVISAT-ASAR [1], [2]. Distances from the coast modes with a coverage of 300–400 km (50+ m resolution) are often used. In coastal and shelf areas, where smaller vessels are of interest, ENVISAT and ERS image modes with 100-km swath width and 25-m resolution are frequently used. This paper aims to assess their performances for ship detection using images from the new TerraSAR-X (TS-X) satellite in comparison with other data.

Several TS-X Stripmap images over an area where ship traffic is (partly) known by AIS are collected. Areas of interest were the North Sea, Baltic Sea, and Cape Town. Terrestrial AIS [3] is available for the North Sea, Baltic Sea, and the coast near Cape Town. Due to technical problems, SatAIS is currently not available for the North and Baltic Seas. A case study of a TS-X image from Cape Town with synergistic use of TS-X and SatAIS is presented.

This paper is organized as follows. Section II gives an overview about Earth observation (EO) and vessel tracking data. Sections III and IV address the strategy of ship detection and some limitations. Advanced processing for false-alarm discrimination is discussed. This specific processing takes advantage of the large amount of information that can be retrieved from SAR data. Some false alarms may be discarded by detecting SAR azimuth or range ambiguities. We present some results of our near-real-time (NRT) ship-detection processing. In Section V, examples are presented. In Section VI, the velocity estimation of moving ships is explained.

II. SatAIS and Terrestrial AIS Used Together With TS-X

AIS systems were designed primarily for maritime safety and particularly for collision avoidance. Satellite AIS (SatAIS) is considered as an add-on to the coastal stations, thus extending the vessel-monitoring capability for safety and security aspects to a global scale [4], [5].

In this chapter, TS-X, Live-AIS, and SatAIS data are introduced. An example of ship surveillance using TS-X is presented.

A. TS-X

TS-X is an X-band polarimetric SAR capable of imaging up to 1-m resolution in Spotlight mode. TS-X can be used for a wide variety of applications including visual interpretation, mapping, digital-elevation-model creation, disaster monitoring, and oceanography. Table I gives an overview of the TS-X system parameters. TS-X Stripmap mode is used for this study as

Manuscript received March 2, 2009; revised November 28, 2009 and March 23, 2010; accepted April 12, 2010. Date of publication October 14, 2010; date of current version February 25, 2011.

S. Brusch, S. Lehner, T. Fritz, and M. Soccorsi are with the Remote Sensing Technology Institute, German Aerospace Center, 82234 Wessling, Germany (e-mail: stephan.brusch@dlr.de).

A. Soloviev is with the Oceanographic Center, Nova Southeastern University, Dania Beach, FL 33004 USA.

B. van Schie is with LuxSpace Sarl, 6815 Betzdorf, Luxembourg.

Color versions of one or more of the figures in this paper are available online at http://ieeexplore.ieee.org.

Digital Object Identifier 10.1109/TGRS.2010.2071879

TABLE I
OVERVIEW OF TS-X MODES (PINK: EXPERIMENTAL MODES)

Product	Coverage [az x rg]	Resolution [az x rg]	Polarization	Full Performance Range
HR SpotLight	5 x 10 km^2	1.0 m x (1.5 – 3.5 m)	single, dual, quad	20 – 55°
Spotlight	10 x 10 km^2	2.0 m x (1.5 – 3.5 m)	single, dual, quad	20 – 55°
StripMap	≤1650 km x 30 km	3.0 m x (1.7 – 3.5 m)	single	20 – 45°
StripMap (polarimetric)	≤1650 km x 15 km	6.0 m x (1.7 – 3.5 m)	dual, quad	20 – 45°
ScanSAR	≤1650 km x 100 km	16.0 m x (1.7 – 3.5 m)	single, dual, quad	20 – 45°
300 MHz Exp.-Mode Spotlight	5 x 10 km^2	1.0 m x (0.6 – 1.5 m)	single, dual, quad	20 – 55°
Dual Receive StripMap	≤1650 km x 30 km	1.5 m x (1.7 – 3.5 m)	single, dual, quad	20 – 45°
ATI		Acc. 15-60 km/h		

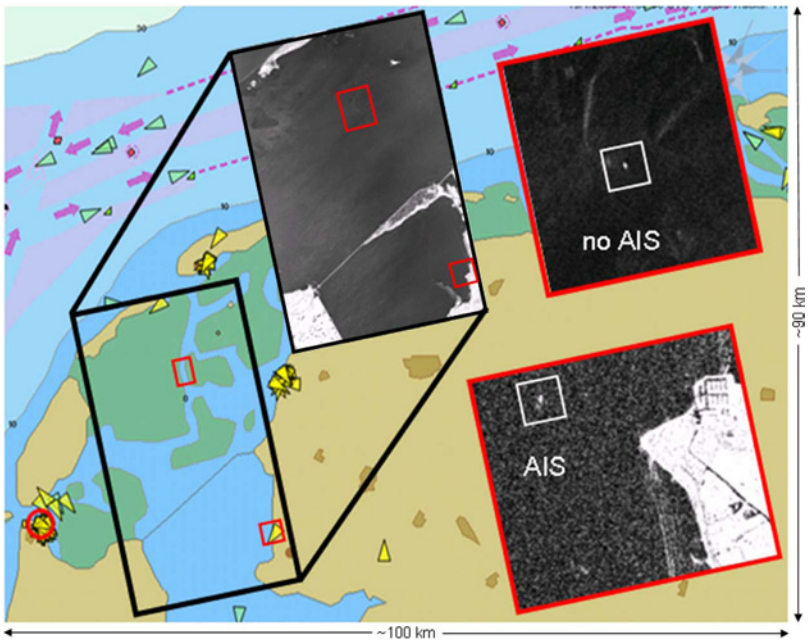

Fig. 1. AIS Fairplay web screenshot and superimposed TS-X Stripmap image acquired on January 19, 2009 at 17:26 UTC. [(Green arrows) Vessel sailing at 0.5 knots or faster. (Yellow arrows) Vessel stopped or sailing at less than 0.5 knots. (http://www.ais-live.com)].

it shows reasonable coverage of 30 km at a still high resolution of 3 m.

B. Terrestrial AIS

AIS is a shipborne broadcast system by which ships inform each other about their position, course, speed, name, and many other parameters of the specific ship. This is used in navigation primarily for maritime safety and particularly for collision avoidance. AIS messages from ships are collected by coastal receivers. The range of coastal AIS receivers is typically 40 km offshore, but can be considerably longer if the receiver is installed on an elevated position and also during particular atmospheric conditions, which are favorable to very high frequency propagation [5]. For this study, we used a terrestrial AIS Live IHS Fairplay account to acquire AIS reports of ships in real time. Fig. 1 shows an example of the AIS web page with superimposed TS-X images of the Dutch coast acquired on January 19, 2009 at 17:26 UTC.

C. SatAIS

Several institutions and companies have demonstrated that AIS signals can be effectively received using spaceborne systems. This fact makes SatAIS a powerful data source to provide global situational awareness of ship positions, vessel and fleet movements, and maritime traffic density mapping. The ship AIS signal detection is possible in the entire radio visibility range of a satellite equipped with an AIS payload. For a payload in low Earth orbit at an altitude of 650 km, the distance from

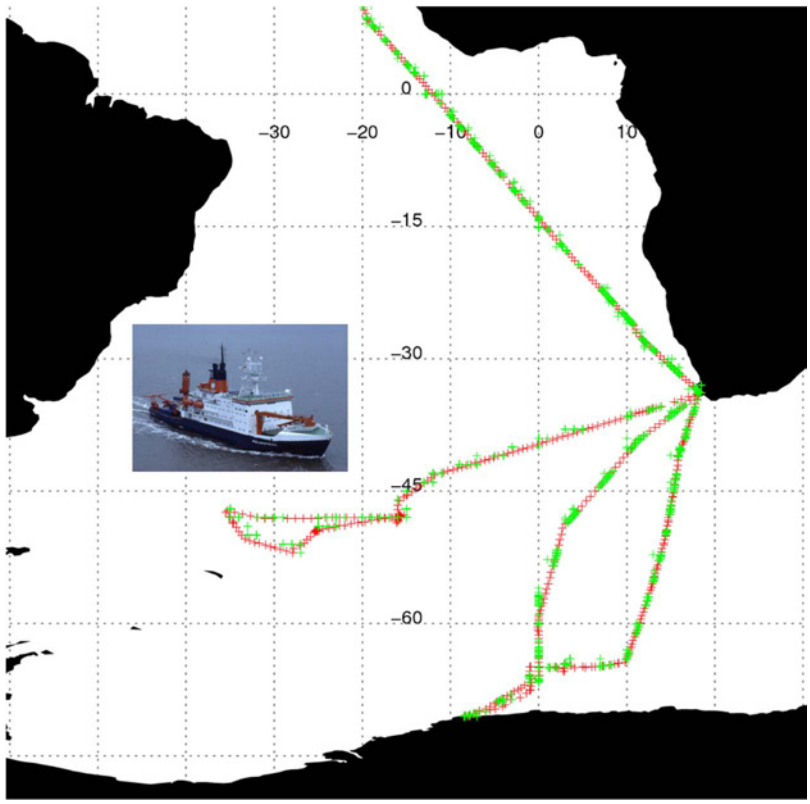

Fig. 2. (Green) SatAIS reports of the German research vessel Polarstern superimposed on the (red) vessel track as reported by the German Research Center Alfred Wegner Institute at its journey (2008/2009) ANT-XXV-3-4.

message source to receiver varies between 2800 km (very low elevation angle) and 650 km (the space-based receiver is directly over the ship in zenith). This means that the average field of view of the payload is well above 20 million square kilometers.

The advantages of SatAIS are clearly the following:

1) the possibility of complete global coverage;
2) vessel tracking from berth to berth;
3) availability in areas without land-based means of vessel detection.

Global coverage and the ability to track vessels from berth to berth are the main advantages that distinguish SatAIS from other maritime intelligence data sources. Moreover, SatAIS features the availability of all information contained in the actual AIS messages as transmitted by ships, providing a complete and extensive information source on all the parameters with respect to individual ships. This enables a convenient and effective way of analyzing maritime traffic around the globe and in certain areas of interest.

The data received by SatAIS have demonstrated the applicability of AIS data in maritime surveillance scenarios, underlining the advantages as previously listed. Fig. 2 shows SatAIS reports for the research vessel “Polarstern” on its journey ANT-XXV-3-4 [6].

In the next couple of years, it is planned to launch a number of SatAIS payloads using this experience as a basis in order to enhance the reception of AIS messages with respect to payloads currently in orbit and to increase the AIS message quality. The launch of future payloads will also dramatically enhance the refresh rate of available AIS data from a certain region and will improve the guaranteed percentage of detected vessels. An increase in the number of detected vessels per area will lead to an increase in the number of scenarios in which SatAIS is applicable, such as harbour traffic planning, search and rescue, global vessel tracking, antipiracy operations, and detection of illegal transports, combined with other sources such as SAR imagery.

In 2010, a SatAIS system will be launched by the German Aerospace Center (DLR) using a directional antenna and improved filtering system for coincident ship messages [7]. This will overcome problems of receiving messages over traffic crowded areas like the North Sea and Baltic Sea.

D. Ship Monitoring With TS-X

The hijacking of the supertanker MV Sirius Star by Somali pirates initiated a case study to test the response time of the TS-X data acquisition as well as the rapid tasking performance of the ground segment DLR-BN (Ground Station Neustrelitz, Germany) for monitoring the situation. The supertanker was hijacked close to Somalia (Africa) on November 18, 2008 and was released on January 9, 2009. With the detected ship positions derived from large-area ScanSAR and Stripmap search acquisitions, follow-up data takes in high resolution but at smaller coverage, modes Spotlight and High-Resolution Spotlight were planned. The standard TS-X EOWEB (http://eoweb.dlr.de:8080/servlets/template/welcome/entryPage.vm) order interface and the nominal product processing and delivery chain (two days) were used for this purpose. The order rights, however,

TABLE II
DATA TAKES ACQUIRED TO MONITOR THE SIRIUS STAR. A OR D INDICATES ASCENDING AND DESCENDING ORBITS, RESPECTIVELY, R OR L GIVES THE RIGHT- OR LEFT-LOOKING ATTITUDE MODE, RESPECTIVELY, AND I STANDS FOR THE CENTER INCIDENCE ANGLE

Nr.	Date	Dir.	Mode	i	Detection / Remarks
1	2008-11-22T03:02	D L	SC	38°	yes
2	2008-11-22T14:56	A R	SC	33°	yes
3	2008-11-24T02:28	D R	HS	53°	no – moved 30km to NE
4	2008-11-27T15:04	A R	SC	52°	yes
5	2008-11-29T02:36	D R	SL	37°	yes
6	2008-11-29T14:30	A L	HS300	39°	yes
7	2008-12-03T14:56	A R	SM	35°	yes
8	2008-12-05T02:28	D R	SM	52°	yes
9	2008-12-08T15:04	A R	HS	51°	yes – dual polarization HH/VV
10	2008-12-10T02:36	D R	SM	37°	yes
11	2008-12-14T14:56	A R	SM	35°	yes
12	2008-12-19T15:04	A R	SM	51°	yes
13	2008-12-25T14:56	A R	SM	35°	yes
14	2009-01-05T14:56	A R	SM	35°	yes
15	2009-01-07T02:28	D R	SM	52°	yes
16	2009-01-12T02:36	D R	SM	37°	no – freed on January 9th

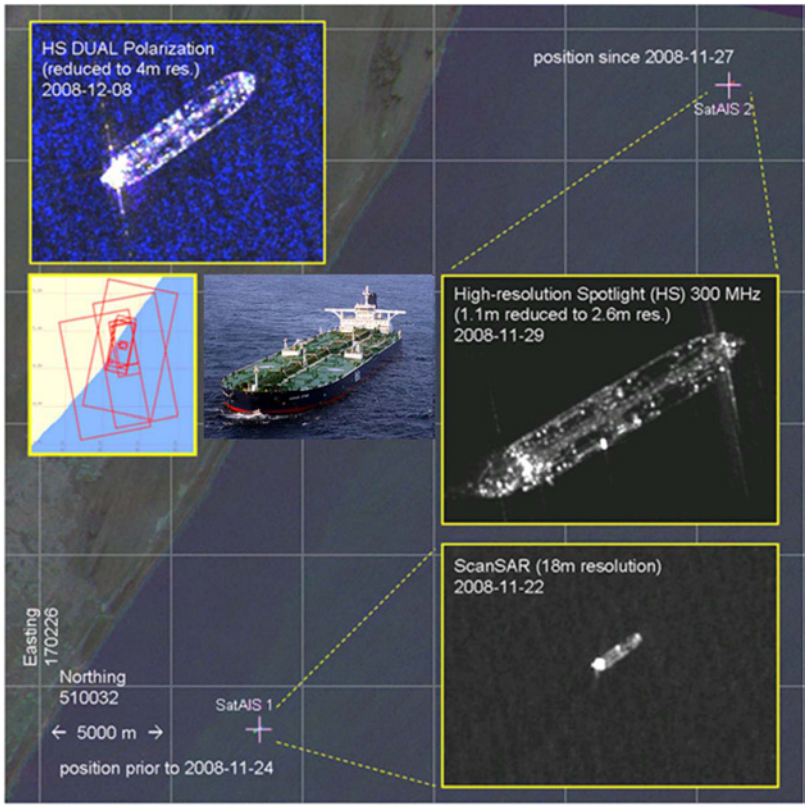

Fig. 3. Optical image and color composite of three TS-X ScanSAR acquisitions [(red) 2008-11-27T15:04, (green) 2008-11-22T03:02, and (blue) 2008-11-22T14:56] showing the position of the Sirius Star off Somali coast and its displacement. During the two acquisitions of November 22, the ship was anchoring at the exact same position (yielding a cyan color). The blowups are from three of the 16 single acquisitions, with the footprints indicated on the map plot. The AIS coordinates retrieved later on are indicated by white crosses (source: LuxSpace).

were extended to access the out-of-full-performance-range beams and left-looking data.

The first two ScanSAR products from November 22, 2008 did not only yield a clear detection at $4°35'35''$ N, $48°06'14''$ E but provided already enough details for an identification. The subsequent High Resolution Spotlight (HS) data take on the 24th were placed at this location but showed no sign of the ship since it had moved in the meantime. This initiated a new search acquisition, revealing on November 27 the new anchoring site at $4°48'59''$ N, $48°15'52''$ E approximately 30 km northeast of the old position. Several high-resolution data takes were acquired from this area in the following weeks, and the ship was found to remain within 1000 m of this position until it was released on January 9, 2009. The test case proved that the TS-X system is suited to task and execute acquisitions based on the analysis of preceding products within two to three days even close to the equator using the nominal ordering, processing, and delivery chains.

TABLE III
PARAMETERS OF ALL ACQUISITIONS

Polarization	HH
Sensor Mode	Stripmap
Product Type	Multi-Look Ground Range Detected
Orbit Precision	Science
Pass Direction	Ascending / Descending
Looking Direction	Right Looking
Incidence Angle Minimum	20
Incidence Angle Maximum	45
Radiometric Accuracy	0.7 db
Resolution	3m

Due to applicable German laws, the highest resolution data including the 1.1-m HS 300-MHz products are not approved for publication and, hence, are available only in radiometrically enhanced product variants with a resolution coarser than 2.5 m. Table II lists the acquisitions, and Fig. 3 shows an overview and examples of the data quality (with reduced resolution). Well visible are the bridge, the pipelines in the middle, and the two helicopter decks near the bow. On the image, SatAIS reports are superimposed by red crosses. The positions agree perfectly in the spatial domain with the TS-X positions. Temporal agreement of the information depends on the satellite orbits. Terrestrial AIS is not available in this region. A synergetic use of SatAIS and SAR data allows one to assess the maritime situation around hijacked ships.

III. Overview of Ship-Detection Strategy on SAR Images

Ship-detection systems generally consist of five stages for standard NRT ship detection in the ground segment Neustrelitz (Germany, DLR):

1) preprocessing;
2) land masking;
3) prescreening;
4) discrimination;
5) feature extraction.

A. Preprocessing

TS-X Level 1b (L1b) products are calibrated by using the annotated files inside the TS-X product. Geolocation is done by an interpolation using the annotated coordinates, the geolocation grid, and the mapping grid of the product. The expected pixel location accuracy is around 2 m [8]. In Table III, the details of TS-X acquisitions are reported.

B. Land Masking

Land masking uses a shoreline database [9] with an eligible buffer zone included to limit the processing of ship detection to sea area. It is important because ship detectors can produce high numbers of false alarms when applied to land areas. Accurate land masking is generally difficult due to inaccuracy of recorded coastline, tidal variations, and coastal constructions. Fig. 4 shows an example of a land-masked image (land color: cyan) acquired over the Baltic Sea–Gdansk on August 5, 2008 at 16:26 UTC.

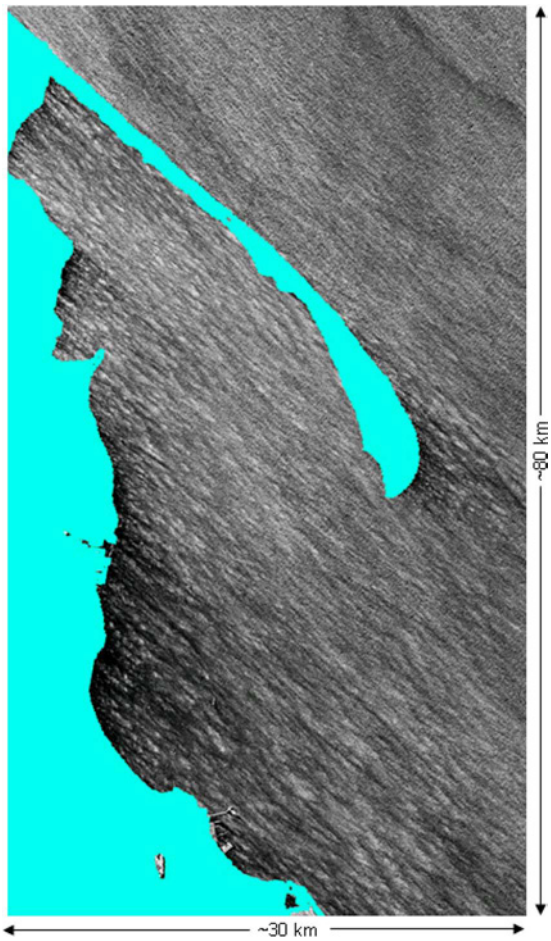

Fig. 4. Land-masked TS-X image (land color is cyan) acquired over the Baltic Sea–Gdansk on August 5, 2008 at 16:26 UTC.

C. Prescreening

Preprocessing applies a simple moving-window adaptive threshold algorithm to detect bright points. A classical constant-false-alarm-rate (CFAR) algorithm is chosen due to its robustness. Further details are given in Section IV.

D. Discrimination

Discrimination is the rejection of some false alarms using target measurements or characterization of specific oceanographic or meteorological phenomena. The variability of the sea surface depends on the wind field. To investigate the wind-field influence, we calculated the wind field by using a geophysical model function X-MOD [10].

Bright-point detection is sometimes not sufficient and, when used by itself, is not able to avoid detections related to oceanographic events, e.g., breaking waves or meteorological events like rain cells. Further errors can arise from SAR image artifacts, such as sidelobes, azimuth ambiguities from land, or strong point targets over the open sea. In this paper, we describe the avoidance of azimuth ambiguities as detected ships. The

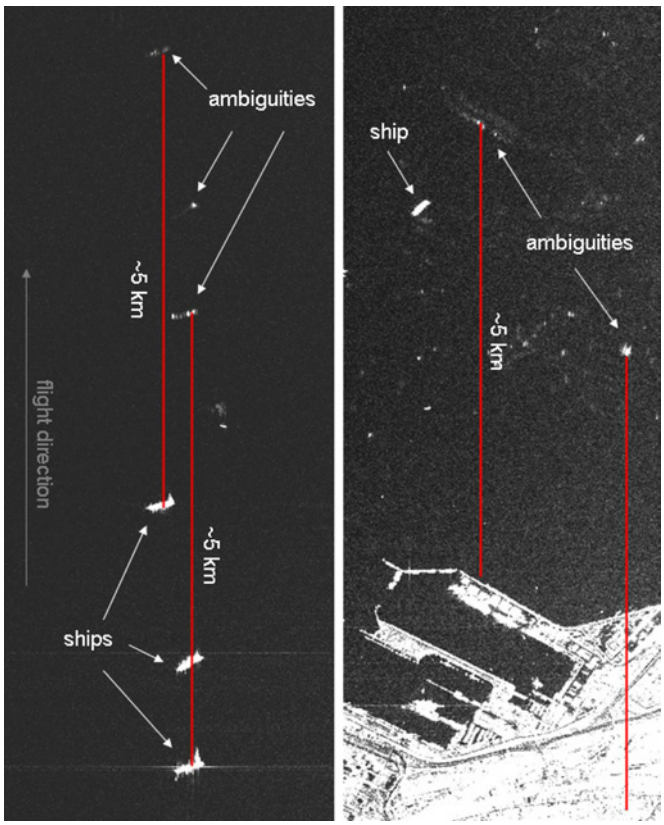

Fig. 5. (Left) Example of azimuth ambiguity at around 5.2 km above the real vessel. This kind of ambiguity can easily lead to a false detection. (Right) Strong azimuth ambiguity at around 5 km above the real target over land. Most of the bright spots inside the ambiguity could be detected and confused as vessels.

TS-X system is designed to avoid range ambiguities [11]. The distance of azimuth ambiguities Δx to point targets is calculated by

$$\Delta x = \Delta t_{\text{ambi}} * f_0 \tag{1}$$

where f_0 is the zero Doppler velocity and

$$\Delta t_{\text{ambi}} = \frac{PRF}{FM} \tag{2}$$

where PRF is the pulse repetition frequency and FM is the derivative time of the Doppler frequency derived from the product annotation given in the Extensible Markup Language annotation file for the L1b product. Azimuth ambiguities in TS-X Stripmap mode images of strong point targets are visible at around 5.2-km offset.

The detection algorithm is designed to exclude azimuth ambiguities of ship targets. For strong scatterers over land, a couple of SAR images are used to create lookup tables of scatterers and ambiguities. These tables are used to avoid false alarms. Azimuth ambiguities from strong point targets like ships and point targets over land are shown in Fig. 5.

E. Feature Extraction

Based on standard L1b TS-X intensity images, ship length, width, and heading are automatically extracted. If the displacement between the ship wake and the ship is detectable, this feature can be used as a direct measurement for ship-speed retrieval (see Section VI).

IV. Detection Algorithm for TS-X Stripmap Images

The test area (target box) is surrounded by a guard area and then, further, by a background area. The purpose of the guard area is to ensure that no part of an extended target is included in the background area, and hence, the background area is representative of the background statistics. Thus, the dimensions of the target, guard, and background areas in pixel domain have to be adapted to image resolution in both range and azimuth directions and to minimal and maximal dimensions of the ship under consideration.

A natural aim in designing adaptive threshold detectors is to ensure that the probability of a false alarm is constant. In this case, the threshold is chosen such that the percentage of background pixel values which lie above the threshold is constant. If this is done, then the false-alarm rate (number of false alarms per unit area of imagery) is likewise constant. One method for CFAR detection is to work directly with the histogram of the background windows and set the threshold at the appropriate point in the tail of the distribution. Choosing a parametric distribution model for the background is equivalent to specifying the associated parametric probability density function $f(x)$, where x gives possible pixel values. Once $f(x)$ has been chosen and its parameters are estimated from the background samples, the probability of false alarm (PFA) for the threshold T is given by

$$PFA = 1 - \int_{-\infty}^{T} f(x)dx = \int_{T}^{\infty} f(x)dx. \tag{3}$$

Designing a CFAR detector involves solving (3) for the threshold T in terms of the specified PFA and the estimated parameters of the pdf $f(x)$. An analytic solution to this problem is not always possible, and numerical methods may be needed. One approach is to search for the correct value of T by trial and error.

The statistical model used in this work is the Gaussian distribution. In this paper, ship detection is done on TS-X multilook ground-range-detected (MGD) Stripmap products. Gaussian distribution is the best approximation due to an increase of the signal-to-noise ratio by resizing the image. In this case, the detector is

$$x_t > \mu_b + \sigma_b t \Leftrightarrow TARGET \tag{4}$$

where x_t is the pixel value under test, μ_b is the background mean, σ_b is the background standard deviation, and t is a detector design parameter which controls the PFA (or, equivalently, the false alarm rate). According to [12], the best tradeoff between probability of detection and false-alarm rate occurred when $t = 5.5$ for low-resolution images. Note that $t = 5.5{-}6.0$ is recommended for high-resolution imagery, as described in [12]. For TS-X images, the best tradeoff has been found for

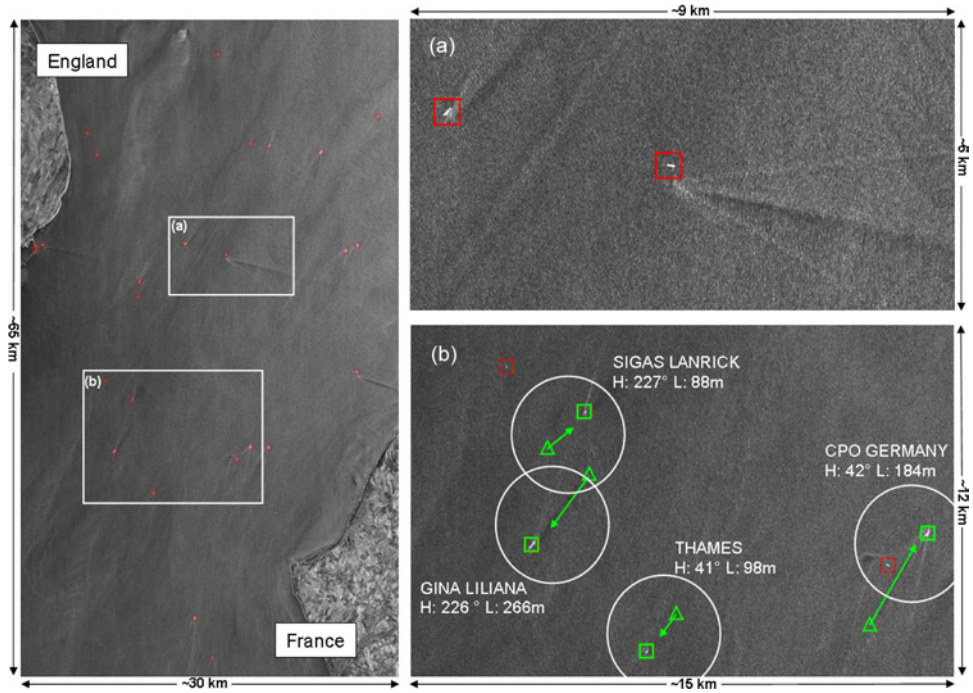

Fig. 6. (Left) TS-X Stripmap mode image (30 km × 65 km, HH polarization, 3-m resolution) over the English Channel acquired on March 22, 2009 at 06:17 UTC. [(Left) Detected ships marked with red rectangles. (Right) (b) (Red) Ships without AIS messages. (Green) Ships with AIS messages, marked with a triangle. (H) Heading. (L) Length.]

TABLE IV
OVERVIEW OF TS-X SHIP DETECTION CORRELATION TO AIS MESSAGES (BASED ON 2234 AIS LIVE MESSAGES AND 144 TS-X IMAGES)

TS-X Mode	Azimuth Resolution	Ship Size	Sea State (SWH)	Wind Speed	Total number of valid AIS messages	Correlation Rate
Stripmap MGD	3.3m	15-20m	< 3m	up to 15 m/s	91	~73%
Stripmap MGD	3.3m	20-50m	< 3m	up to 15 m/s	367	~82%
Stripmap MGD	3.3m	50-100m	< 3m	up to 15 m/s	787	~89%
Stripmap MGD	3.3m	> 100m	< 3m	up to 15 m/s	989	~98%

$t = 6.3{-}6.5$. The number of true detections (hits) has been estimated by subtracting the predicted number of false alarms from the total number of detections.

V. TS-X SHIP SURVEILLANCE AND COMPARISON TO AIS AND SatAIS DATA

The TS-X detection product has been compared with AIS and/or SatAIS data. During first tests of TS-X images, some differences between AIS reports and SAR data could be detected. The AIS Live (Fairplay) account enables the user to only copy and paste the ship reports from the AIS Live Web page. Thus, time gaps between the acquisition and AIS data may appear. Other discrepancies occur also due to incorrect reporting from AIS and SAR geolocation inaccuracies. Fig. 6 shows an example of ships detected by the DLR detection algorithm SAR AIS Integrated Toolbox (SAINT) and superimposed terrestrial AIS (Fairplay) data over the English Channel.

The TS-X image was taken over the channel on March 22, 2009 at 06:17 UTC. Terrestrial AIS data have been provided by Lloyds Register Fairplay. The left image in Fig. 6 shows the channel area with superimposed detected ships. Fig. 6(a) shows a zoom over two detected targets with imaged Kelvin and turbulent wake signatures. Fig. 6(b) shows an example of detected ships and superimposed terrestrial AIS (time window of 15 min) over the English Channel region. For this study, we defined a circle with a radius of around 1 km (white circles) to search for negative false alarms (detected targets). Arrows are showing the estimated position of ships based on heading, speed, and time reports by AIS (triangles). Rectangles are SAR-detected targets. Ship reports from AIS connected to SAR positions are plotted in green. Overall, a consistency (matches between SAR and AIS) of more than 80% is reached. The two red rectangles (zoom) are SAR-detected ships without matching AIS reports. These small vessels [with length between 28 and 40 m (estimated on SAR data)] do not have to report to the AIS system.

Validation studies based on 2234 AIS reports for 134 TS-X images show that the estimation of length has an averaged accuracy of around 20%. The correlation rate between TS-X detections and AIS messages is shown in Table IV.

To define a confidence level for small vessels (ship size < 25 m), ground-truth data are needed as these vessels are not required to send AIS reports. Ship detection on TS-X Spotlight

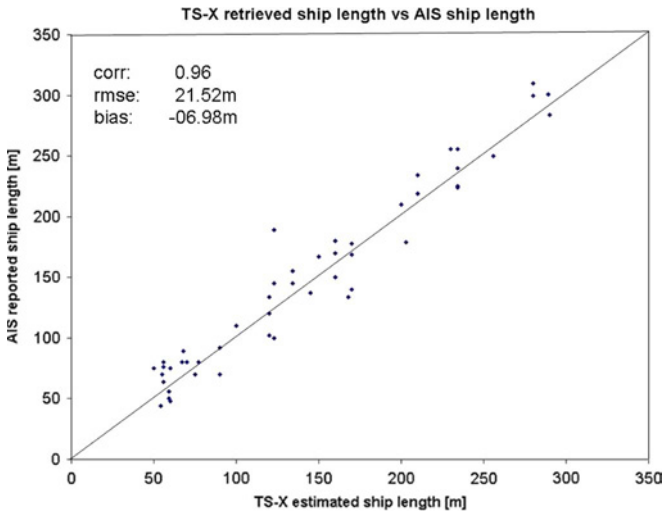

Fig. 7. Ship length measured automatically in SAR images against length reported by terrestrial AIS (49 data pairs).

mode allows the detection of even smaller targets down to the image resolution of less than 1 m. Fig. 7 shows a comparison of SAR-retrieved ship length against AIS reports for ships longer than 100 m. SAR-estimated dimensions of ships are in good agreement with AIS reports with a correlation of 0.96, a bias of -6.98 m, and an rmse of 21.52 m.

Due to high resolution (down to 1.1 in azimuth) and narrow swaths ($<$ 10 km), the TS-X Spotlight mode is a useful tool to monitor ship traffic inside ports. Fig. 8 shows an example of a TS-X Spotlight image acquired over the port of Rostock (Germany) on July 20, 2009. The cyan rectangle shows a zoom inside the port. Vessels anchored at the pier are visible. Single ships are distinguishable. Also detectable is the Search and Rescue Vessel Arkona with a length of 27 m marked with "1." Further detectable is the offshore wind turbine marked by "2."

In the next example, for the first time, the synergetic use of high-resolution EO data and satellite-based AIS data is demonstrated. Fig. 9 shows a TS-X Stripmap mode image in the southern Atlantic Ocean near Cape Town. Vessels detected by SAR are superimposed and marked by red rectangles. Collocated ships with terrestrial AIS messages are marked by green rectangles. SatAIS is superimposed with yellow rectangles. SAR, as well as terrestrial AIS and SatAIS, reports the same position of targets, as can be observed in Fig. 9(a). Fig. 9(b) shows the general limitation of terrestrial AIS, covering only an area up to 40 km of the Cape Town area. Three small vessels are detected by SAR. One of them is reporting an AIS signal via SatAIS. Furthermore, a moving target is visible. The SAR-detected ship reported by SatAIS is moving south.

In the following chapter, the focus is on ship-speed retrieval using complex TS-X images.

VI. Velocity of Moving Objects Using Single-Look Complex Data

In order to determine ship speed, the object velocity is regarded as a vector with two components, one in azimuth and one in range direction. The algorithm consists of three main steps. The first step is the generation of a sequence of single-look SAR images followed by the detection of moving objects. This consists of the detection of ship candidates and the respective velocity estimation. The third step is the compensation of the object motion and the imaging of the moving objects. Two kinds of detection and estimation of speed of the moving objects are possible, either in a multilook image or in a sequence of single-look images.

The latter possibility allows visualization of the object motion. In this manner, we get a sequence of consecutive images, whereas the positions of the moving objects change from image to image. Fig. 10(b) and (c) shows zooms of a sequence of two single-look images based on a TS-X complex image acquired on June 9, 2008 over the east coast of Florida acquired during a measurement campaign [13]. The nonzero target velocity causes a mismatching of the processing filter, which is sensible to the Doppler variation. Thus, the target appears in the image blurred and in a different position, depending on its velocity vector components. In each look, the moving target has different characteristics, because each look corresponds to a different integration time.

For the estimation of ship velocity, we follow the procedure described in [14]–[18]. The velocity of the target is estimated with a single-channel complex-valued SAR image by azimuth-split decomposition, i.e., spectrum bandpass filtering. From the original image, two images, at a reduced resolution, are obtained, and the velocity vector components are estimated through change detection analysis of the target in the two images. The azimuth or cross-range velocity component is calculated by

$$v_{\mathrm{Ta}} \approx -\frac{\Delta x \cdot dx \cdot v_S^2}{\Delta f \cdot \lambda \cdot R_T} \tag{5}$$

where Δx is the displacement vector, dx is the pixel resolution, v_S is the spaceborne velocity, Δf is the distance between the center frequency of the two sublooks, λ is the radar wavelength, and R_T is the distance between the SAR sensor and the target. The target azimuth velocity component v_{Ta} depends on the estimation accuracy of the displacement vector Δx. The displacement has been calculated through estimation of the distance between the centers of mass of the azimuth amplitude distributions of the target in the two sublooks, respectively. In order to obtain a more reliable profile, the pixels of the ship have been selected by thresholding and by visual inspection. Then, the azimuth profile has been obtained by range averaging. The use of the visual inspection is justified by the fact that the pixels belonging to the wake are included when only an automatic thresholding method is used. This happens because the processing is performed on a Complex SAR (COSAR) image, which has a low signal-to-noise ratio, i.e., $ENL = 1$, with respect to MGD products.

In the beginning, the displacement vector has been estimated visually; then, more accurate methods have been used by estimating the distance between the two centers of mass and the coherence. We encountered a problem due to the strong signal of the ship wake with the latter method; thus, the alternative method of the centers of mass has been chosen although it is less precise.

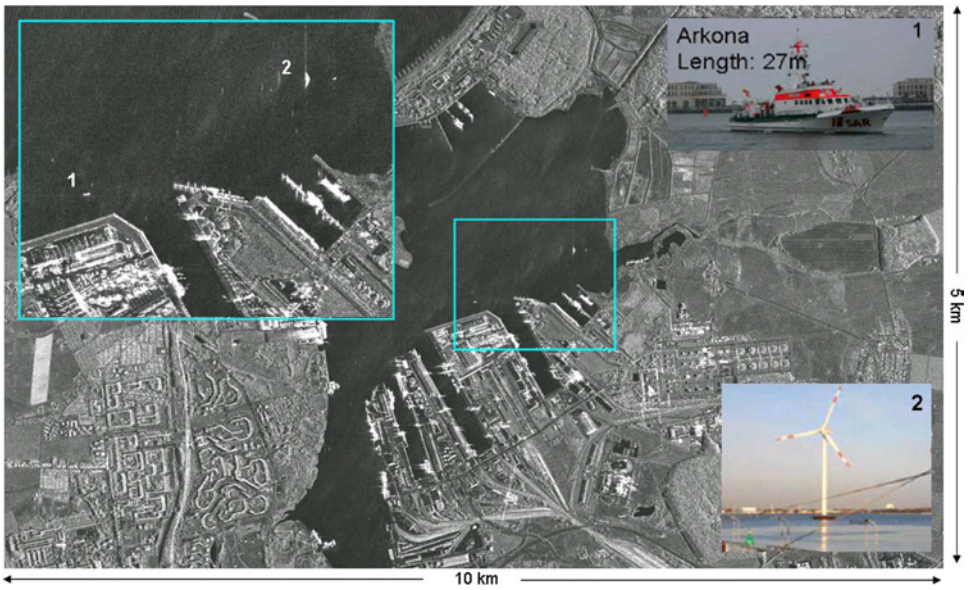

Fig. 8. TS-X high-resolution Spotlight (5 km × 10 km, HH polarization) acquired on July 20, 2008 over the port of Rostock (Germany). (Cyan rectangle) Subscene with the SAR (Search and Rescue) vessel Arkona and a wind turbine.

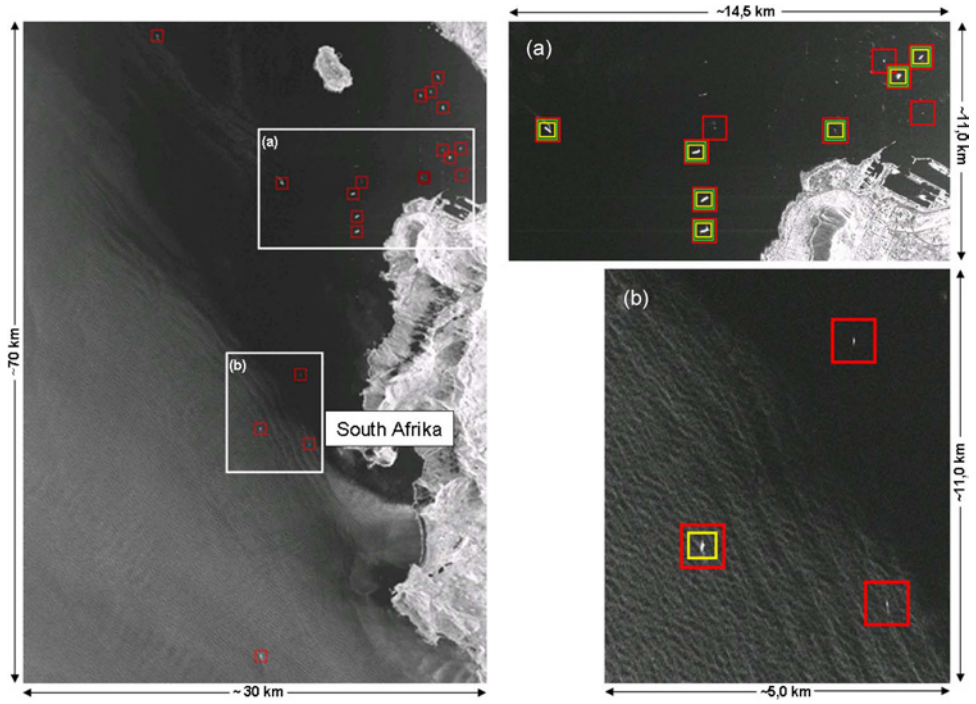

Fig. 9. TS-X Stripmap subimage (HH polarization, 3-m resolution) acquired on December 16, 2008 over the southern Atlantic Ocean with (red rectangles) ships detected by the DLR ship-detection algorithm, (green rectangles) superimposed AIS (Fairplay) data, and (yellow rectangles) SatAIS reports.

The displacement vector is calculated according to $\Delta x = |c_1 - c_2|$, where c_1 and c_2 are the centers of mass for sublooks 1 and 2, respectively. The center of mass is computed by weighting the time position with the amplitude value in the following way:

$$c_i = \frac{\sum_j m_{ij} x_{ij}}{\sum_j m_{ij}} \tag{6}$$

where the sum is over the number of pixels belonging to the target of the ith look, m_{ij} represents the amplitude value, and x_{ij} is the position of the ith look at time position j. The range component is calculated by inverting the following:

$$\Delta t \approx -\frac{f_{DT} \cdot \lambda \cdot R_T}{2 \cdot v_S^2} = \frac{v_{\mathrm{Tr}} \cdot \sin(\theta) \cdot R_T}{v_S^2} \tag{7}$$

where Δt is the temporal shift, f_{DT} is the Doppler frequency, and θ is the local incident angle. The last equation in (7) is obtained by remembering that

$$f_{DT} = -\frac{2 \cdot v_{\mathrm{Tr}} \cdot \sin(\theta)}{\lambda}. \tag{8}$$

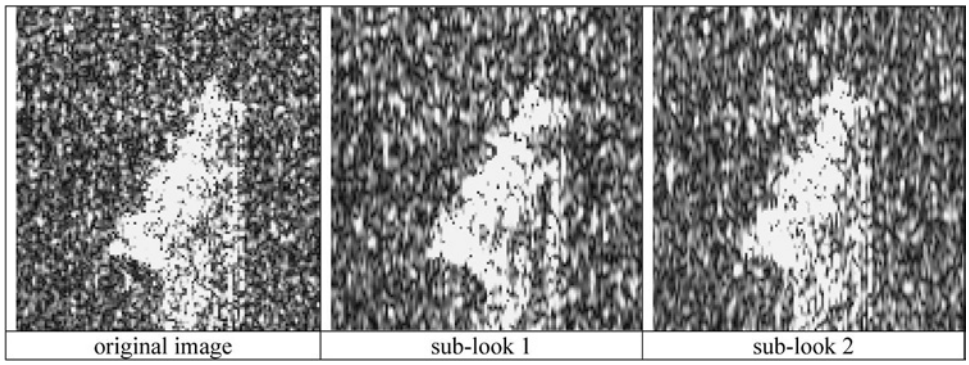

Fig. 10. Sequence of two single-look images based on a TS-X complex image.

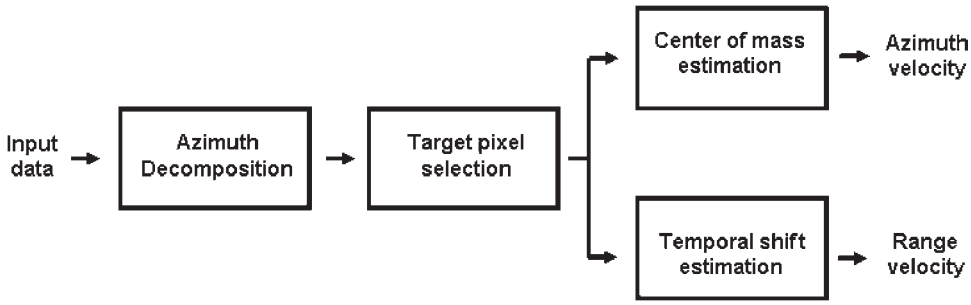

Fig. 11. Flowchart of speed estimation.

The local incident angle θ counts for the projection of the range velocity component in the look direction of the sensor.

The target-range velocity component v_{Tr} depends on the estimation accuracy of the temporal shift Δt. With reference to the block diagram in Fig. 11, the input data are a tail of the original image containing the target to analyze. The data are Fourier transformed in azimuth direction, and thus, the azimuth split is done in the following way:

1) Fourier transform (FT) in azimuth;
2) whitening;
3) splitting;
4) centering the subspectra;
5) weighting;
6) inverse discrete FT in azimuth.

A Hamming window weights the spectrum of the analyzed data. The target is selected by an amplitude threshold and visual inspection, and thus, the undesired pixels are masked. The azimuth profiles of the target after masking and averaging in range are shown in Fig. 12, where the displacement vector is visible. However, for a more accurate estimation of the displacement vector, the distance between the centers of mass of the target in the two sublooks is estimated. Thus, the azimuth velocity is calculated according to (6). The estimation of the temporal shift Δt is done by weighting the signal amplitude in each image with the time t_i of this image.

The estimated velocity of the ship is 12.2 knots with a dispersion of 1.6 knots as compared with the 11.3 knots available from the AIS information. However, the time lag between the SAR acquisition and the AIS may allow for the difference.

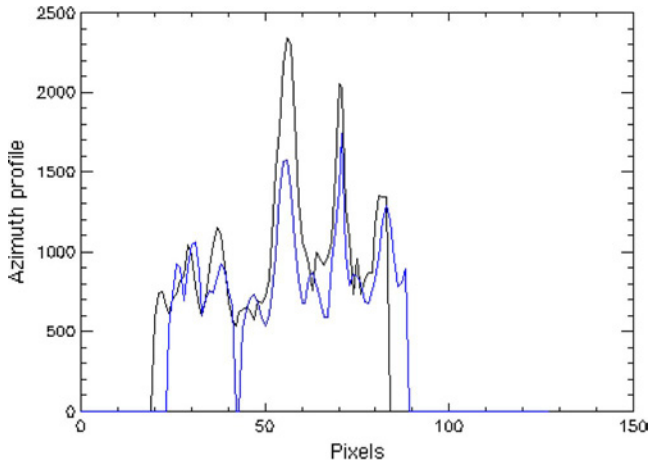

Fig. 12. Profiles of the target in (black) sublook 1 and (blue) sublook 2. The profile is obtained by range averaging, and the pixels not belonging to the target are masked.

VII. Conclusion

In this paper, TS-X acquisitions have been analyzed in order to assess the potential of this new sensor to be used for ship monitoring. A synergetic use of high-resolution TS-X images and SatAIS was presented. An adapted ship-detection algorithm for TS-X Stripmap mode images based on the classical CFAR method was introduced. This TS-X mode has a typical coverage of 30 km $\times$ 100 km and a resolution of about 3 m in azimuth. Thus, this mode is a good choice for monitoring ship traffic in coastal areas and also over the open ocean. The ship detection still shows limitations in coastal areas due to insufficient land

masking or geophysical phenomena such as tidal change or strong meteorological conditions, e.g., severe weather. The algorithm has been integrated to the DLR Toolbox (SAINT) for automatic detection of both large and small vessels. Results show that AIS-carrying larger vessels (length above 60 m) were detected in around more than 93% of cases. For smaller vessels (length $<$ 30 m), the assessment of quality is more difficult due to increasing false alarms for small vessels in high-sea-state situations with breaking waves. Additional experiments will give a quality assessment of detecting small vessels. For moving and nonmoving ships, terrestrial AIS or SatAIS show good agreement with detected ships by SAR. The limitation of terrestrial AIS with coverage of about 40 km off the coast makes SatAIS and SAR a perfect candidate to fill this gap of ship traffic information over open oceans.

Ship-detection case studies of the hijacked tanker Sirius Star and the research vessel Polarstern in areas where no terrestrial AIS is available were given. Velocity estimation based on COSAR data has been demonstrated. The algorithm has been implemented for NRT use of the antenna station in Neustrelitz (Germany).

REFERENCES

[1] S. W. McCandless and C. R. Jackson, "Principles of synthetic aperture radar," in *Synthetic Aperture Radar, Marine User's Manual*. Washington, DC: NOAA, 2004, pp. 1–23.

[2] H. Greidanus, "Satellite imaging for maritime surveillance of the European seas," in *Remote Sensing of the European Seas*, vol. XXII. New York: Springer-Verlag, 2008, pp. 343–358.

[3] P. W. Vachon, R. A. English, and J. Wolfe, "Validation of RADARSAT-1 vessel signatures with AISLive data," *Can. J. Remote Sens.*, vol. 33, no. 1, pp. 20–26, 2007.

[4] [Online]. Available: http://www.luxspace.lu

[5] G. K. Hoye, T. Eriksen, B. J. Meland, and T. Narheim, "Space-based AIS for global maritime traffic monitoring," in *Proc. 7th IAA Symp. Small Satell. Earth Observ.*, Berlin, Germany, May 4–8, 2009.

[6] T. Bruns, S. Lehner, X.-M. Li, K. Hessner, and R. Wolfgang, "Analysis of an event of 'parametric rolling' onboard RV 'polarstern' based on shipborne wave radar and satellite data," *IEEE J. Ocean. Eng.*, 2010, to be published.

[7] [Online]. Available: http://www.dlr.de/irs/desktopdefault.aspx/5023_read-7202/

[8] TerraSAR-X Ground Segment—Basic Pruduct Specification Document, TX-GS-FF-3302, 18.03.2009.

[9] [Online]. Available: http://www.ngdc.noaa.gov/mgg/shorelines/gshhs.htmlgshhs

[10] S. Lehner, S. Brusch, and X.-M. Li, "Coastal wind field and sea state measured by TerraSAR-X," in *Proc. IEEE RadarCon*, Pasadena, CA, May 4–8, 2009, pp. 1–3.

[11] J. Mittermayer and J. M. Martinez, "Analysis of range ambiguity suppression in SAR by up and down chirp modulation for point and distributed targets," in *Proc. IEEE IGARSS*, 2003, vol. 6, pp. 4077–4079.

[12] D. J. Crisp, "The state-of-the-art in ship detection in synthetic aperture radar imagery," Intell., Surveillance and Reconnaissance Div., Inf. Sci. Lab., Def., Sci. Technol. Org., Edinburgh, S.A., Australia, May 2004, Res. Rep. DSTO-RR-0272.

[13] A. Soloviev, M. Gilman, K. Young, S. Brusch, and S. Lehner, "Sonar measurements in ship wakes simultaneous with TerraSAR-X overpasses," in *Proc. 3rd TerraSAR-X Sci. Team Meeting*, Oberpfaffenhofen, Germany, 2008.

[14] C. C. Wackerman, K. S. Friedman, W. G. Pichel, P. Clemente-Colon, and X. Li, "Automatic detection of ships in RADARSAT-1 SAR imagery," *Can. J. Remote Sens.*, vol. 27, no. 5, pp. 568–577, 2001.

[15] M. Kirscht, "Detection and focused imaging of moving objects evaluating a sequence of single-look SAR images," in *Proc. 3rd Int. Airborne Remote Sens. Conf. Exhib.*, Copenhagen, Denmark, Jul. 1997, vol. I, pp. 393–400.

[16] M. Kirscht, "Detection, velocity estimation and imaging of moving targets with single-channel SAR," in *Proc. EUSAR*, Friedrichshafen, Germany, May 25–27, 1998.

[17] J. R. Moreira and W. Keydel, "A new MTI-SAR approach using the reflectivity displacement method," *IEEE Trans. Geosci. Remote Sens.*, vol. 33, no. 5, pp. 1238–1244, Sep. 1995.

[18] R. K. Raney, "Synthetic aperture imaging radar and moving targets," *IEEE Trans. Aerosp. Electron. Syst.*, vol. AES-7, no. 3, pp. 499–505, May 1971.

Stephan Brusch received the Diploma degree in meteorology from the Free University, Berlin, Germany, in 2006. He is currently working toward the Ph.D. degree with the Remote Sensing Technology Institute, German Aerospace Center, Wessling, Germany.

In 2006, he joined the German Aerospace Center (DLR/DFD). In the framework of the Helmholtz Research Network "Integrated Earth Observing System" Helmholtz-EOS, he worked on synthetic aperture radar (SAR) observation of ocean waves and wind fields. His current research interests include the development of algorithm for ship detection and ground moving target indicator, with emphasis on the analysis of single-channel complex SAR images.

Susanne Lehner received the M.Sc. degree in applied mathematics from Brunel University, Uxbridge, U.K., in 1979 and the Ph.D. degree in geophysics from the University of Hamburg, Hamburg, Germany, in 1984.

She was a Research Scientist with the Max-Planck Institute for Climatology, Hamburg, and joined the German Aerospace Center (DLR/DFD), Wessling, Germany, in 1996. She is currently a Research Scientist in marine remote sensing with the Remote Sensing Technology Institute (DLR/IMF), German Aerospace Center, working on the development of algorithms determining marine parameters from synthetic aperture radars.

Thomas Fritz received the Diploma degree in physics from the University of Münster, Münster, Germany, in 1996 and the Dr. rer. nat. degree from the University of Bonn, Bonn, Germany, in 2000.

He then held a postdoctoral position in the Radioastronomical Institute, University of Bonn. In 2003, he joined the Remote Sensing Technology Institute, German Aerospace Center (DLR), Wessling, Germany, and participated in the development of the TerraSAR-X Multi-Mode SAR processor. In particular, he was responsible for TerraSAR-X SAR product specification, characterization, and verification. He is currently responsible for the development of the interferometric processing chain and the system engineering of the Integrated TanDEM-X Processor.

Matteo Soccorsi (S'05–M'10) received the M.S. degree in telecommunication engineering from the University of Rome "Tor Vergata," Rome, Italy, in 2005 and the Ph.D. degree in signal and images from Télécom ParisTech, Paris, France, in 2010.

Since 2005, he has been with the German Aerospace Center (DLR), Wessling, Germany. He is currently holding a postdoctoral position, which is supported by the German Academic Exchange Service (DAAD), in the Marine Remote Sensing Group, Remote Sensing Technology Institute (DLR/IMF). His primary research interests include the development of algorithms for ship detection and ground moving target indicators, with emphasis on the analysis of single-channel complex synthetic aperture radar images.

Alexander Soloviev received the M.S. degree in physics from Moscow Institute of Physics and Technology, Moscow, Russia, in 1976, the Ph.D. and D.Sc. degrees in physics and mathematics from the former Soviet Academy of Sciences, Moscow, in 1979 and 1992, respectively, and the MBA degree from the University of Florida, Gainesville, in 2010.

He was a Visiting Scientist with the University of Hawaii, Honolulu, and the University of Hamburg, Hamburg, Germany, and a Scientist in the two leading institutions of the former Soviet Academy of Sciences: P. P. Shirshov Institute of Oceanology and A. M. Oboukhov Institute of Atmospheric Physics. He is currently an Associate Professor with the Oceanographic Center, Nova Southeastern University, Dania Beach, FL. He is also an Adjunct Professor with the Rosenstiel School of Marine and Atmospheric Science, University of Miami, Coral Gables, FL. He has participated in several major oceanographic experiments (POLYMODE, JASIN, FGGE, TOGA COARE, and GASEX). He is the author and coauthor of more than 60 research articles. With Prof. Roger Lukas from the University of Hawaii, he coauthored the monograph *The Near-Surface Layer of the Ocean: Structure, Dynamics, and Applications* (Springer, 2006). His research interests include turbulence and microstructure in the near-surface layer of the ocean, upper ocean boundary layer, bottom boundary layer, remote sensing, biophysical interactions in the ocean, CO2 uptake by the ocean, hurricane physics, coastal ocean circulation, and ocean engineering. His major field of study is physical oceanography.

Dr. Soloviev is a member of the American Geophysical Union and the American Meteorological Society.

Bart van Schie received the M.Sc. degree in aerospace engineering from Delft University of Technology (TU Delft), Delft, The Netherlands, in 2007.

In 2007, he obtained HAREC Radio amateur license from Belgian Institute for Postal services and Telecommunications, Brussels, Belgium. He has been a Project Manager of the Pathfinder 3 AIS satellite project. He has also worked on the space systems engineering and ground segment design (both hardware and software) for the Pathfinder 2 AIS satellite project; management of launch campaign, IOT and satellite operations for the Pathfinder 2 satellite project; configuration management for the LUXAIS payload as part of ESA's COLAIS project to put an AIS receiver onboard the International Space Station Project manager of AIS commercial services including implementation of the data service infrastructure, customer acquisition, and support and all activities of LuxSpace within ESA's MARISS project; From March to July 2007, he was an intern with the European Aeronautic Defence and Space Company (EADS) Space Transportation, Friedrichshafen, Germany. From October 2005 to June 2006, he was with TOPDesk, where he worked on the design of a test chamber for Bose-Einstein condensation experiments for launch onboard the ATV. He has also worked on Netherlands Financial administration of a medium-sized software company, including debtor and tax administration. Since January 2008, he has been with LuxSpace Sarl, Betzdorf, Luxembourg.